# FACULTY
# OF MATHEMATICS
# AND PHYSICS
# Charles University

# Search for New Physics
# in b-hadron decays
# at the ATLAS experiment

Pavel Řezníček

HABILITATION THESIS

Prague 2022

# Contents

# 1  Introduction

The Standard Model (SM) of particle physics describes the basic building blocks of matter, the quarks and leptons, and their interactions. So far, it has been very successful in describing the results of all experiments in the microworld, covering a wide range of energy of the interactions of all types of particles. Its last missing piece, the Higgs boson, was recently confirmed [1, 2] in experiments at the Large Hadron Collider [3] (LHC), a proton-proton and ion-ion accelerator and collider located in the European Organization for Nuclear Research (CERN). However, there are phenomena that SM is not able to describe, in particular, dark matter and dark energy, the gravity interaction, or the excess of matter over antimatter in the universe. Another drawback of the theory is a large number of free parameters (19, resp. 26 if massive neutrinos are considered[1]), whose values cannot be predicted and are established by the experiment.

The search for New Phenomena (NP) beyond the SM can be classified into two categories: direct search for new particles not existing in the SM, or indirect search for the new particles by testing SM predictions for known processes when the studied process is modified by virtual corrections from the beyond-SM particles to the SM Feynman diagrams. One of the promising fields for the indirect NP searches is the sector of heavy flavour (HF), the studies of production and decays of hadrons containing heavy quarks, which I have joined. In particular, I have specialized in the physics of $b$-hadrons. The energy release in $b$-hadron decays (hereafter referred to as $B$-decays) is large enough to enable factorization of short- and long-distance effects (perturbatively calculable versus calculations within soft quantum chromodynamics (QCD)), thus making theoretical predictions possible and testable.

The experimental tests of the SM predictions typically include studies of interactions of elementary particles at defined energies, provided by particle accelerators. The largest collider experiments of the present provide particles at energies up to a few teraelectronvolts[2]. HF physics has been studied on all lepton-lepton, hadron-hadron, and hadron-lepton type collider experiments. The lepton colliders have the advantage of being able to tune their parameters for very clean $B$-meson production, providing almost background-free data, allowing precision measurements of a wide range of the $B$-meson decays. However, they have limited access to double-heavy flavoured $B$-mesons and to $b$-baryons. Experiments at hadron colliders do not suffer from this particular limitation. In addition, they also have the advantage of using huge $b\bar{b}$ pairs production cross section, providing better access to rare processes. On the other hand, there is a large background level from other inelastic collisions. Thus, their HF analyses have to focus on specific final states that allow efficient selection and that are not buried in the combinatorial background, formed from a random combination of physics objects accidentally mimicking the searched processes.

I joint the B-physics group at the ATLAS experiment [4] at the LHC. The experiment is using same named general-purpose detector and the physics program is broad [5], ranging from SM measurements including studies of the Higgs boson (and formerly search for it), top quark, heavy flavoured hadrons, intermediate vector bosons, etc., over quark-gluon plasma studies in heavy-ion collisions, up to search for non-SM particles like leptoquarks or those predicted by the supersymmetry theory. The detector is thus not specifically optimized for the B-physics analyses (unlike other LHC experiment: the LHCb [6, 7]). In consequence, the B-physics program (see Section 4) is limited to

---

[1]SM historically considers only massless neutrinos. However, a straightforward extension of SM is possible to include the massive neutrinos and their oscillations.

[2]Throughout the thesis electronvolts are used to as particle energy units. Also, the usual convention $\hbar c = 1$ is applied, reporting particle momenta as a product $pc$ and rest mass in terms of the rest energy $mc^2$.

studies of processes in which the provided results can be competitive to the specialized B-physics experiments, or at least can provide valuable cross-check of their results.

The thesis is composed of my main contributions to the B-physics analyses at ATLAS, as listed in the Appendix A, namely the following ones.

- I am one of the principal authors of measurements of the charge conjugation parity violation ($CP$-violation, CPV) phase $\phi_s$ in $B_s^0 \to J/\psi\phi$ decays[3] [8–11]. It is a precision test of the SM (see Section 5 for more details). I wrote the core statistical tool (an unbinned maximum likelihood fitter), contributed to the evaluation of the number of systematic uncertainties and cross-checks, (toy-)Monte Carlo (MC) simulations, editorial work as well as presentations and defense of the analysis in front of the ATLAS collaboration. Also, I served as an advisor or co-supervisor of several bachelors and doctoral students of the analysis team. In this team, I continue to analyze the latest ATLAS data, though with a stronger emphasis on the (student's) advisory role and a few contributions to the systematic uncertainties evaluations.

- I contributed significantly to the analysis of rare decay $B^0 \to K^{*0}\mu^+\mu^-$ [12], searching for possible deviations from the SM prediction, which have been observed by the LHCb experiment (see Sections 2 and 6 for more details). In particular, I did part of the editorial work, evaluated several systematic uncertainties, prepared MC simulations and served as an advisor to one of the principal doctoral students of the analysis. Currently, I am leading the effort of the analysis of the latest ATLAS data.

- I also joined the search for exotic structures in the $B$-decays, namely, I directly contributed to the search for tetraquark-like structures in the $B_s^0\pi^\pm$ system [13] (more details in Section 7), evaluating a few systematic uncertainties.

An important part of the ATLAS B-physics program is also the preparation of the measurements to the future stages of the accelerator, namely the High-Luminosity LHC with upgraded ATLAS detector, but also the preceding phases. I am the main author of these projections for the analyses of $B_s^0 \to J/\psi\phi$ [14] and $B^0 \to K^{*0}\mu^+\mu^-$ [15] decays and contributed also the other older similar studies [16–18], including those in the pre-LHC stage [19]. The studies became part of the CERN Technical Design Reports or Yellow Books [20–25], and the most important outcomes are described in Section 8.

At the early stage of every data-taking campaign, cross-checks of the detector performance are needed. These typically include measurements of well-known parameters of particles, such as their rest mass of decay time. I am one of the main authors of several such analyses monitoring the mass and or decay time of the $B^\pm$, $B^0$ and $B_s^0$ mesons [26–28], contributing to both statistical interpretation and evaluation of the systematic uncertainties. I am also coauthor of the method of estimating the effect of residual misalignment on the ATLAS B-physics measurements [29] (though universally applicable to any ATLAS analysis).

The first stage of data selection runs online, already during the data-taking itself, since there is not enough space to store data for all collision events. The system of these fast selections is called the trigger system. The efficiency and robustness of the system are obviously crucial for every ATLAS analysis. I am a long-standing member of the B-physics trigger group, contributing to B-trigger validation and monitoring and efficiency evaluation [18], as well as leading trigger-related work of several students (diploma theses, collaboration qualification tasks). My involvement in the subject

---

[3]Hereafter, charge conjugation of every mentioned particle and decay is implied throughout, unless stated otherwise.

resulted in being chosen as a coordinator of the B-physics trigger group in the period of 2012–2014.

My initial involvement, in 2011, was within the collaboration of ATLAS Semiconductor Tracker (SCT), a silicon strip detector that measures the position of the passage of charged particles born in the collision. During this period, I developed specialized tests [30–32] of the SCT detector modules and participated in their standard quality assurance tests [33] and tests with accelerated particles at CERN (testbeam) [34]. In 2003 I entered the ATLAS B-physics group, at that time preparing the B-physics program based on Monte Carlo simulations. I joined the group analyzing the feasibility of rare semileptonic $B$-decays, with results at the early stage published within conference proceedings [35, 36]. Within this work, I became one of the principal authors of the ATLAS B-physics analysis software (SW) framework [**37**]. The B-physics analyses at that time also served as one of the test grounds for distributed analysis on the Worldwide LHC Computing Grid. Later, my activities expanded to the B-physics trigger development, preparation of the Monte Carlos simulations, and joining other analyses as the $CP$-violation studies. The involvement was rewarded by the opportunity to present summary results of ATLAS B-physics group at a number of conferences (selected proceedings in [38–43]) and finally by being selected as the coordinator of the entire ATLAS B-physics group in 2013–2015, during which the whole group published 11 papers [44–55].

## 2 Flavour Anomalies

Despite the effort and expectations put into the direct searches for New Physics beyond the Standard Model, no particles incompatible with SM have been found. However, recently several deviations from SM predictions have emerged in known processes. At the dawn of the 21$^{\text{st}}$ century, neutrino oscillations were (conclusively) observed [56], confirming that neutrinos are massive. Around the same time, the measurement [57] of the anomalous magnetic dipole moment of a muon exhibited a $2.7\sigma$ significant deviation from the SM prediction. This measurement was confirmed in 2021 by an independent experiment [58] and the combined deviation of the experimental value from the SM prediction reached a significance of $4.2\sigma$, slightly below the usual $5\sigma$ limit to claim a discovery. However, furthermore, in the last decade, a number of tensions have appeared in the measurements of decays of heavy flavoured hadrons. Finally, a $7\sigma$ deviation from SM is observed in the precise measurement of the $W$-boson mass [59]. As this thesis deals with the New Physics search in the $B$-decays, the next-to-last deviations are detailed below.

### 2.1 Flavour Anomalies in the Experiments

The flavour anomalies include several measurements and corresponding SM predictions. A comprehensive summary of the measurements and SM predictions can be found in Reference [60]. The anomalies are seen in the following processes:

- Measurements of the branching fractions (BR) and angular parameters in the Flavour-Changing Neutral Currents (FCNC)-induced transitions $b \to s\mu^+\mu^-$ at the quark level. The deviations with SM predictions were observed in parameters describing decay angles in the $B^0 \to K^{*0}\mu^+\mu^-$ [61] decay or in differential branching fraction in the $B_s^0 \to \phi\mu^+\mu^-$ [62, 63] decay (although a similar tendency is also seen in the other semimuonic $B$-decays [64–66]). The precisions of all these experimental results are dominated by the LHCb experiment, however, with other experiments contributing non-negligibly to the picture. Tensions had also been present in the BR of purely leptonic decays $B_{(s)}^0 \to \mu^+\mu^-$ [67–69]. However, the latest CMS result [70] is quite compatible with SM.

- Other tensions are seen in the relative decay rate measurements of tree-level $B$-decays including $b \to c\ell^-\nu_l$ transitions:

$$R_{H_c} = \frac{\mathcal{B}(\overline{H}_b \to H_c\tau^-\bar{\nu}_\tau)}{\mathcal{B}(\overline{H}_b \to H_c\ell^-\bar{\nu}_l)}, \tag{1}$$

where $H_b \to H_c$ denotes a transition of $b$-hadron to single hadron with charm quantum number $C = +1$. These transitions include $\overline{B}_{(s)} \to D_{(s)}^{(*)}$, $B_c^+ \to J/\psi$ and $\Lambda_b \to \Lambda_c$. The SM predictions [71–75] for these quantities lie significantly below unity (roughly in the range $0.24 - 0.33$) due to the large effect of $\tau$-lepton mass. The deviations are seen in the combination of the $R(D)$ and $R(D^*)$ measurements from Belle [76–80], LHCb [81–84] and BaBar [85, 86] experiments.

- Until recently, the LHCb experiment had also reported tensions in the lepton-flavour universality (LFU) tests: the measurements of relative decay rates of rare decays $b$-hadrons to muons and electrons:

$$R_h = \frac{\Gamma(B \to h\mu^+\mu^-)}{\Gamma(B \to he^+e^-)}, \tag{2}$$

where $B \to h$ denotes a transition of $b$-hadron to $s$-hadron. The transitions include $B \to K$, $B \to K^*$, and $\Lambda_b \to pK$. Due to the lepton flavour universality, SM predicts these ratios very close to unity [87–90]. The deviations had been seen in the quantities $R_K$ [91] and $R_{K^*}$ [92]. However, in the fall of 2022, updated measurements were presented [93, 94], showing perfect agreement with the SM prediction (and suggesting underestimated systematic uncertainties in the preceding results).

The deviations of these measurements from the SM predictions range roughly from $2\sigma - 4\sigma$. Thus, individually, they would not yet be that much significant. However, combined together and accounting for the fact that the physics processes behind these decays are correlated, the tensions provide an intriguing and consistent picture. The main experimental results demonstrating the tensions are shown in Figures 1, while those that mitigated recently are presented in Figures 2.

## 2.2 Theory Interpretations of the Anomalies

The theoretical description of the flavour decays requires both weak interactions and strong dynamics of hadronization described by the QCD. The two processes are taking place at very different energy scales ($W$-boson mass versus $b$-quark mass). Therefore a low-energy effective field theory is used. The construction of the Effective Hamiltonian follows the Operator Product Expansion technique [95], where the short-range interactions with heavy fields such as Higgs, top quark, $W^{\pm}$, and $Z$ approximately correspond to point interactions and are encoded in so-called Wilson coefficients $C_i$, while the remainder of the SM fields is present in a set of local operators $\mathcal{O}_i$. For the $b \to s$ transitions, the effective Hamiltonian looks like this:

$$\mathcal{H}_{\text{eff}} = -\frac{4G_F}{\sqrt{2}} V_{tb} V_{ts}^* \frac{\alpha}{4\pi} \sum_{i}^{10} \left( C_i \mathcal{O}_i + C_i' \mathcal{O}_i' \right). \tag{3}$$

In this case, the Hamiltonian is explicitly separated into the left- and right-handed components.

The amplitudes of exclusive hadronic decays with an initial state $I$ and final state $F$ are obtained as:

$$A(I \to F) = \langle F | \mathcal{H}_{\text{eff}} | I \rangle = -\frac{4G_F}{\sqrt{2}} V_{tb} V_{ts}^* \frac{\alpha}{4\pi} \sum_{i}^{10} \left( C_i \langle F | \mathcal{O}_i | I \rangle + C_i' \langle F | \mathcal{O}_i' | I \rangle \right). \tag{4}$$

The matrix elements for processes with hadrons in the final state are difficult to calculate; non-perturbative methods, e.g. lattice QCD [88] or QCD light-cone sum rules [87] need to be used, and the decay has to be described in terms of form factors. This aspect limits the precision of the SM predictions for the properties of the decays, where the anomalies are observed. The limited precision is well seen in Figures 1 on top. A more detailed description of the theory can be found e.g. in Thesis [96].

The tension in the Neutral Current decays can be explained[4] by a modification of the $b \to s$ operators that include a vectorial lepton current ($\mathcal{O}_9$): the corresponding Wilson coefficient would need a shift by around $-25\%$ of its SM value [97–100]. Furthermore, global analyses including all $b \to s\{\gamma, \ell^+\ell^-\}$ data indicate also modification of the Wilson coefficient connected with the axial lepton current ($\mathcal{O}_{10}$) and/or hadronic currents with non-SM like chirality ($\mathcal{O}_9'$, $\mathcal{O}_{10}'$). For more details, see Reference [60]. The input from

---

[4]The argumentation includes also the now mitigated anomalies in $R(K)$, $R(K^*)$ and $B_{(s)}^0 \to \mu^+\mu^-$ decays

the various flavour anomalies can be used to make a global fit to the values of the Wilson coefficients. Figure 3 shows an example of such global fits, presenting the most affected Wilson coefficients $C_9$ and $C_{10}$.

A number of attempts to explain the anomalies through New Phenomena can be found. A random selection, far from pretending to be complete, includes $Z'$, naturalness, Zee model, or scalar or vector leptoquarks. A summary of the studies can be found, e.g. in Reference [101].
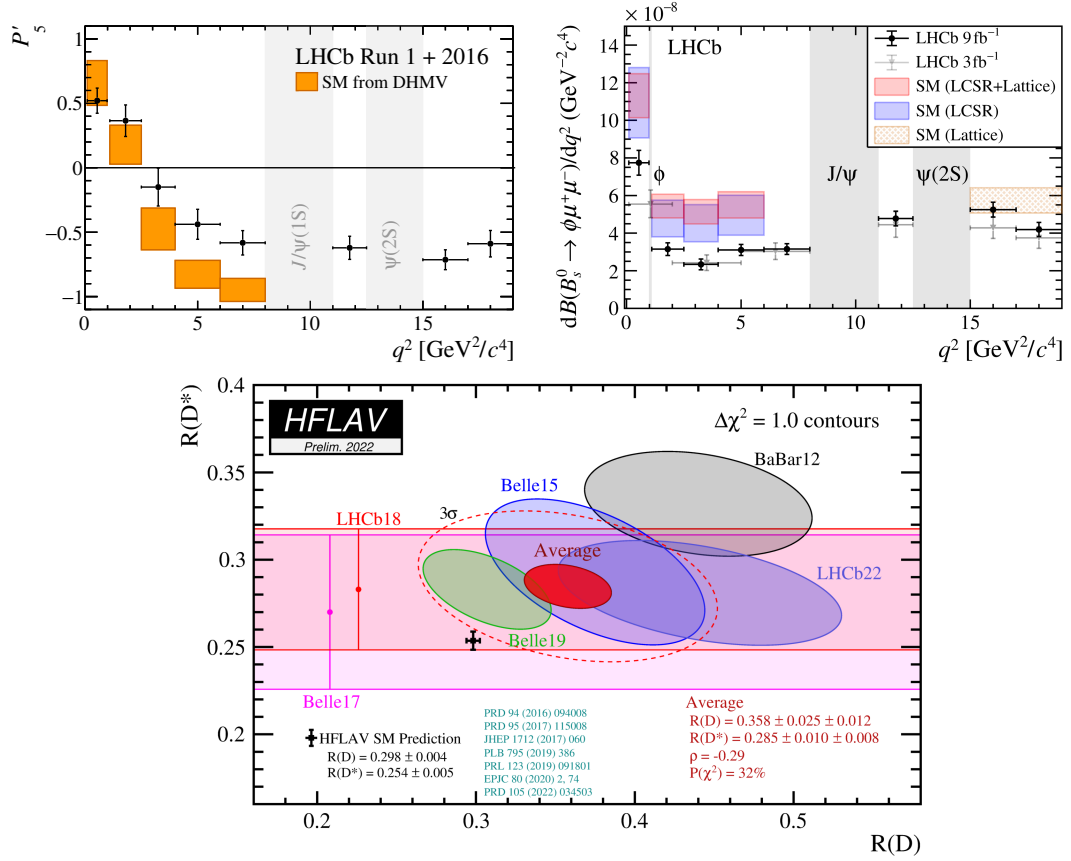


Figure 1: Presentation of the most pronounced (and yet valid) flavour anomalies. References to the experimental results (data) and SM predictions are as follows.

- Top left: Angular parameter $P_5'$ of the $B^0 \to K^{*0}\mu^+\mu^-$ decay, depending on the dimuon invariant mass squared ($q^2$): LHCb data [61], SM prediction [102, 103].

- Top right: Differential decay rate of $B_s^0 \to \phi\mu^+\mu^-$: LHCb data [62, 63], SM prediction using Light Cone Sum Rules [87, 89, 104] at low $q^2$ and Lattice calculations [90, 105] at high $q^2$.

- Bottom: $R(D)$ and $R(D^*)$ ratios: data of LHCb [81–84], Belle [76–80] and BaBar [85, 86]. SM prediction and figure taken from Reference [71].
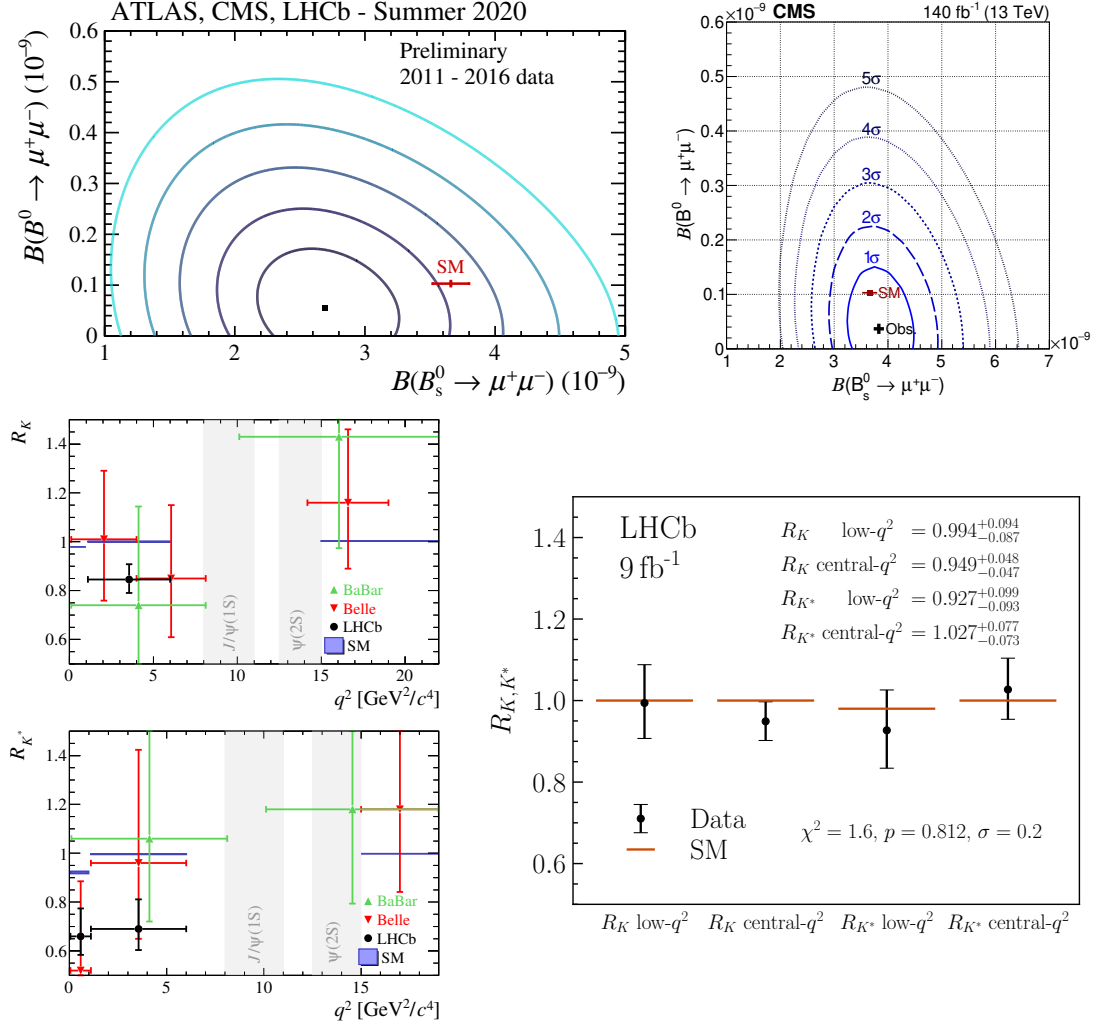
Figure 2: Presentation of the flavour anomalies that have recently mitigated. The left column shows the observed anomalies, the right column presents the updated measurements, now compatible with the SM predictions. References to the experimental results (data) and SM predictions are as follows.

- Top: Branching fractions of $B_s^0 \to \mu^+\mu^-$ and $B^0 \to \mu^+\mu^-$: combined data of LHCb, CMS, and ATLAS [106] (left) and the latest CMS measurement [70] (right), SM prediction [107].

- Bottom left: $R(K)$ ratio in $B^\pm \to K^\pm \ell^+ \ell^-$ and $R(K^*)$ ratio in $B^0 \to K^{*0} \ell^+ \ell^-$: data of LHCb [91, 92] showing the anomaly, overlaid with data of Belle [108, 109] and BaBar [110]. SM prediction [87–90], figures taken from Reference [60]. Bottom right: $R(K)$ and $R(K^*)$ ratios from the updated LHCb measurements [93, 94]. The low/central-$q^2$ regions match those from the previous LHCb measurements as shown in the figures on left. SM prediction [89].
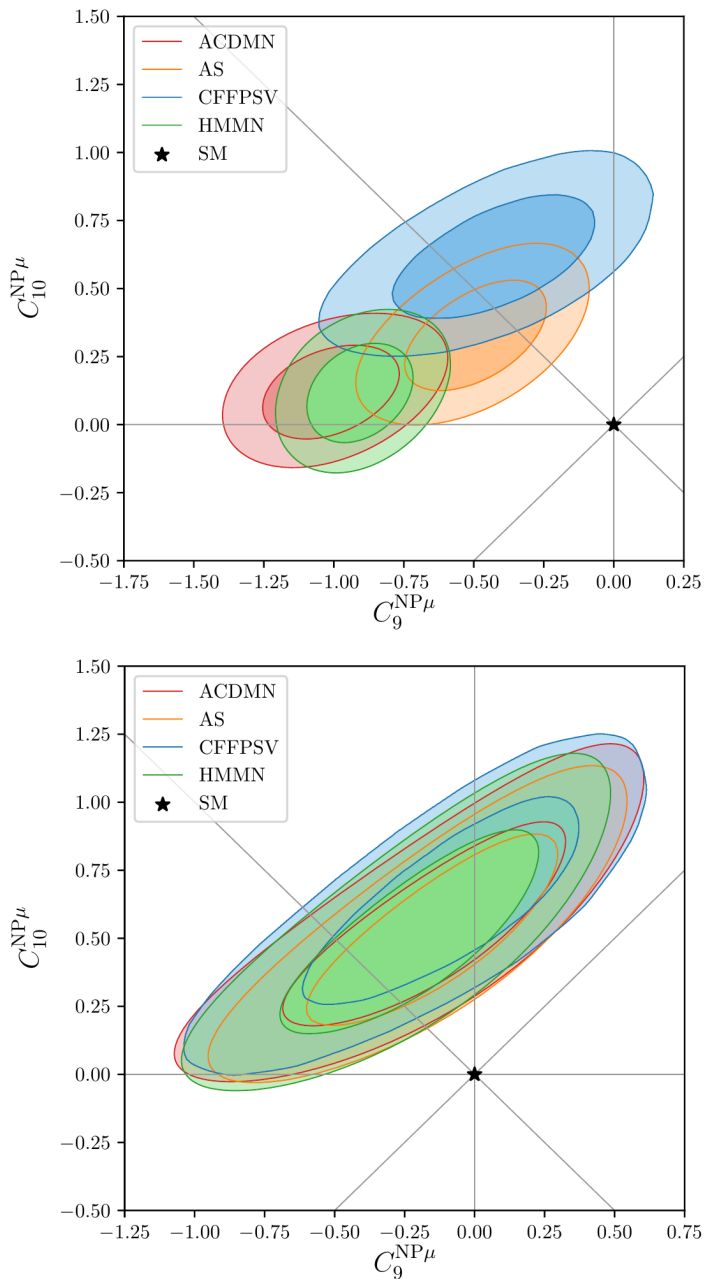
Figure 3: Global fits of the Wilson coefficients $C_9$ and $C_{10}$ using all the $b \to s\ell^+\ell^-$ anomalies (top) and using only the LFU plus $B_s^0 \to \mu^+\mu^-$ ones (bottom). The $C_i^{\text{NP}}$ refers to relative Wilson coefficient contributions from New Physics to the Standard Model values: $C_i = C_i^{\text{SM}} + C_i^{\text{NP}}$. The fits are provided by several theory groups (ACDMN [111], AS [112], CFFPSV [113], HMMN [114]), using slightly different parts of the experimental data, using different statistical frameworks, and having various approaches to form factors computation and assumptions about non-local matrix elements. The results show remarkable agreement between the fits of the various groups and indicate a clear deviation from SM. The figure is taken from a presentation at the conference Beyond Flavour Anomalies III [115]. However, the fits include also the now mitigated anomalies in $R(K)$, $R(K^*)$ and $B_{(s)}^0 \to \mu^+\mu^-$ decays.

# 3    ATLAS experiment

The ATLAS experiment [4] uses a general-purpose detector ATLAS (A Toroidal LHC ApparatuS) placed around one of four interaction points of the LHC. The LHC was designed to collide protons[5] at a center-of-mass energy (c.m.s.) $\sqrt{s} = (7 + 7)$ TeV. The proton beam consists of bunches containing around $10^{11}$ protons. The bunches were supposed to collide with a frequency of 40 MHz, providing in average $\sim 23$ proton-proton ($pp$) interactions in each such a bunch crossing (an *event*). The design instantaneous luminosity, which is the number of collisions per second per effective cross section, was $L = 10^{34}$ cm$^{-2}$s$^{-1}$. However, the real parameters were slightly different from the design, starting at half c.m.s. energy in 2010, but rising almost up to the design $\sqrt{s}$ in 2022. The instantaneous luminosity has quickly reached 75% of the designed value, overcoming it by a factor of $2\times$ in 2022.

The periods of collisions at the LHC and data-taking by the detectors are divided into several Runs, as depicted in Figure 4:

- Run 1 data-taking in 2010–2012, with $\sqrt{s} = 7$ and 8 TeV and luminosity below the design value. The overall collected ATLAS dataset suitable for physics analyses corresponds to integrated luminosity[6] $L_{\text{int}}$ of $(4.9 + 20.3)$ fb$^{-1}$. The average number of interactions $\langle \mu \rangle$ grew from 9.1 in 2011 to 20.7 in 2012 [116].

- Run 2 data-taking in 2015–2018, with $\sqrt{s} = 13$ TeV, but gradually overcoming the design instantaneous luminosity by the factor of $2\times$. $L_{\text{int}}$ reached 139 fb$^{-1}$ and $\langle \mu \rangle$ was 33.7.

- Run 3 data-taking started in 2022 at $\sqrt{s} = 13.6$ TeV at $2\times$ nominal instantaneous luminosity. This period will end in 2025 and is supposed to deliver $L_{\text{int}} = (200 - 300)$ fb$^{-1}$. The $\langle \mu \rangle$ in 2022 was 44.5.

After these periods, the collider and detectors will be significantly upgraded. This High-Luminosity LHC (HL-LHC) is expected to provide a dataset of at least 3000 fb$^{-1}$ of $pp$ collisions at up to $\sqrt{s} = 14$ TeV. The ATLAS Upgrade detector will have to cope with average 200 $pp$ interactions in bunch crossing.
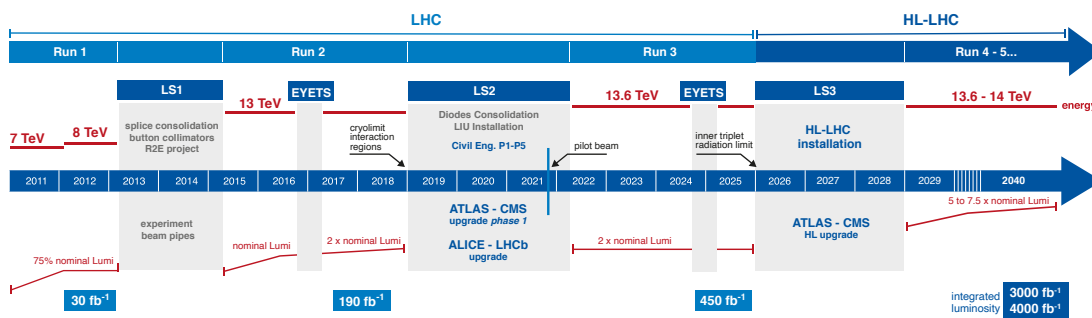


Figure 4: The past and future stages of the LHC / HL-LHC with expected parameters of the $pp$ collisions and the total collected datasets. Figure taken from Reference [117].

A hard $pp$ collision with the potential to produce New Phenomena or heavy SM particles is characterized by a large energy signal in the direction perpendicular to the colliding protons. Such collisions are relatively rare. Due to the fact that there are more $pp$ collisions in single bunch crossing, the interesting events are polluted by several soft

---

[5]Hereafter, the heavy ion collisions at LHC are not discussed, following the scope of the thesis.
[6]Luminosity integrated over the pure time of collisions delivered by LHC.
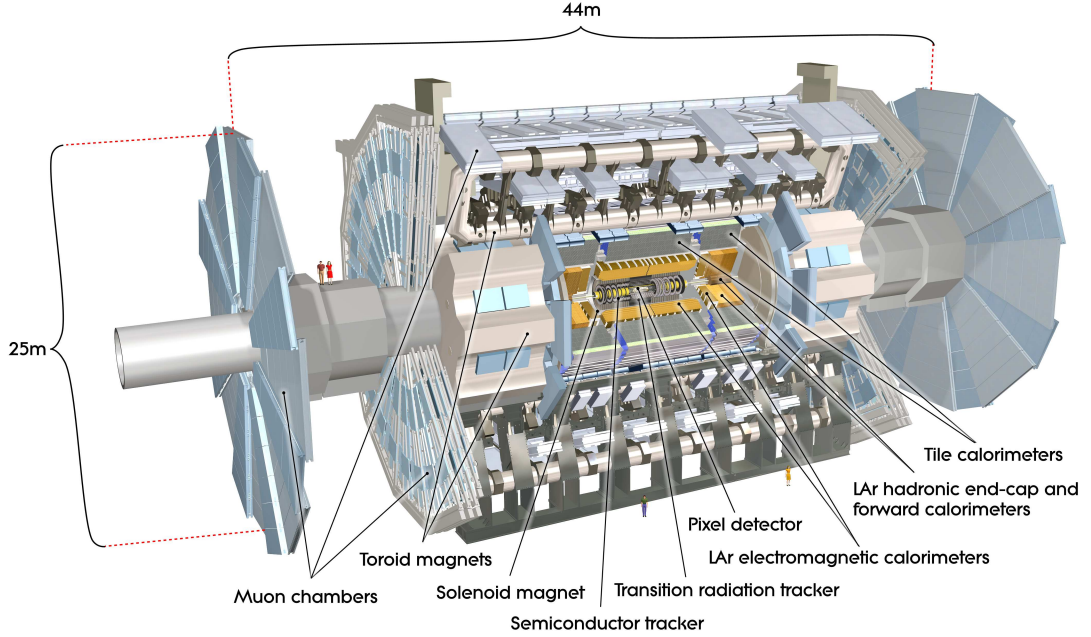
Figure 5: Cut-away view of the ATLAS detector [4]. The dimensions of the detector are 25 m in height and 44 m in length. The overall weight of the detector is approximately 7000 tonnes.

*pp* collisions. This effect is called pileup[7] and significantly enlarges the electronic signal occupancy in the detector subsystems (and combinatorial background in analyses).

The ATLAS detector is composed of several layers (as shown in Figure 5) with the aim of identifying particles coming from the *pp* collision and measuring their electric charge and momentum or energy. However, most of the particles of interest (including the hypothetical ones) quickly decay into lighter ones. The detector is thus designed to detect the products of these decays. Knowledge of the properties of these daughter particles and the use of conservation laws allow the reconstruction of the parameters of the mother particle. The daughter particles need to live long enough to reach the detector, which basically limits the need of detection to stable particles, neutrons, muons, charged pions, and the lightest kaons. A general principle of the detection is based on the characteristic particle interactions with matter via processes such as ionization or bremsstrahlung of charged particles, nuclear collisions, Compton scattering, photoeffect, $e^+e^-$ pair creation from photons, etc. Using these processes (part of) the energy of a passing particle is transferred to the material of the detector. Various techniques and detector layouts are then used to transform that energy into a localized electric signal of magnitude in some way related to the deposited energy.

The ATLAS detector is forward-backward symmetric with cylindrical geometry and nearly $4\pi$ coverage in the solid angle. ATLAS uses a right-handed coordinate system with its origin at the nominal interaction point (IP) in the centre of the detector and the *z*-axis along the beam pipe. The *x*-axis points from the IP to the centre of the LHC ring and the *y*-axis points upward. Cylindrical coordinates $(r, \phi)$ are used in the transverse *xy*-plane, $\phi$ being the azimuthal angle around the *z*-axis. Pseudorapidity is defined in terms of the polar angle $\theta$, $\eta = -\ln \tan(\theta/2)$.

---

[7]Besides this in-time pileup, an additional signal can appear from particles in the preceding *pp* collisions, due to the high collision rate (every 25 ns) compared to the length of the signal from the detector electronics. Further background comes from beam–beam interactions (gas in the underground cavern, beam halo).

The B-physics analyses at ATLAS mostly use the information from the tracking system and the muon detectors, for reasons explained later. These two systems are thus described in more detail in the following sections.

## 3.1  Tracking System

The detector layer closest to the *pp* interaction point is the tracking system [118, 119], the Inner Detector (ID). Its purpose is to reconstruct the tracks of the charged particles and measure their momenta and sign of charges. Since the detector is placed inside a solenoidal magnetic field of magnitude $2\,\mathrm{T}$, the track shape is approximately helix with a radius proportional to the momentum. The system is composed of three subdetectors. Closest to the beam and most precise in the determination of the position of the passing particle are layers of silicon pixel detectors (Pixel). These are then followed by layers of silicon strip detectors (SCT, very precise only in $\phi$-direction), and finally straw tube gaseous detectors (TRT, capable of electron identification). The geometry of the layers is cylindrical in the barrel[8] region, while concentric disks are used in the end-cap. Per track, the detectors typically provide 3 hits in Pixel, 8 hits in SCT, and $\sim 30$ hits in TRT. The system is capable of reconstructing tracks with $p_\mathrm{T} \gtrsim 500\,\mathrm{MeV}$ and $|\eta| < 2.5$ with practically 100% efficiency.

The key performance physics parameters are:

- The precision of the measurement of the momentum of particles in the transverse plane, $p_\mathrm{T}$. The expected resolution from the simulations can be roughly expressed as $\sigma(p_\mathrm{T})/p_\mathrm{T} \simeq 0.04\% \cdot p_\mathrm{T}[\mathrm{GeV}] \oplus 2\%$ [4], but strongly depends on the $\eta$-direction of flight of the particle. In B-physics, the $p_\mathrm{T}$ resolution translates to the resolution of the mass of the reconstructed *b*-hadrons and their daughter particles. For illustration, see also the left Figure 6, the average mass resolution of dimuonic HF decays ($B^0_{(s)}$, $J/\psi$, etc.) is at the level of tenths of MeV, also strongly depending on $\eta$-direction of flight of the *b*-hadron. The best resolution is around $\eta = 0$ in the barrel region, while the worst resolution is at the end of end-caps at $|\eta| = 2.5$, as illustrated in Figure 26. The resolution of light *s*-hadrons (as products of *B*-decays) decaying into a pair of charged hadrons is at the level of a few MeV.

- Since the relative $p_\mathrm{T}$ resolution decreases with $p_\mathrm{T}$, at around $2\,\mathrm{TeV}$ the detector starts to lose the capability to determine charge sign.

- The precision of the direction of flight of the particle ($\phi$, $\theta$) is at the level of a milliradian and for B-physics translates to a typical resolution of decay angles at a level of 2 degrees. The effect on angular B-physics analyses is typically small or even negligible.

- The precision of the transverse impact parameter $d_0$, the closest distance between the track helix and the position of the *pp* collision, the primary vertex (PV), in the transverse plane, is at the level of a few tenths of micrometers. This quantity is directly related to the precision of reconstruction of secondary vertices from *b*-hadrons, and thus also the precision of measurement of their decay time. For illustration, the resolution distribution in Run 1 is shown in the right Figure 6. The distribution emerges from the fact that the resolution strongly depends both on $\eta$ and $p_\mathrm{T}$ of the *b*-hadron. For the case of the plot above, the average proper decay time resolution is $\simeq 100\,\mathrm{fs}$.

---

[8]ATLAS detector is divided to the barrel and end-cap regions by means of the pseudorapidity: barrel is the central part of $|\eta| < 1.05$, while end-cap $|\eta| \geq 1.05$ surrounds the barrel at each side.
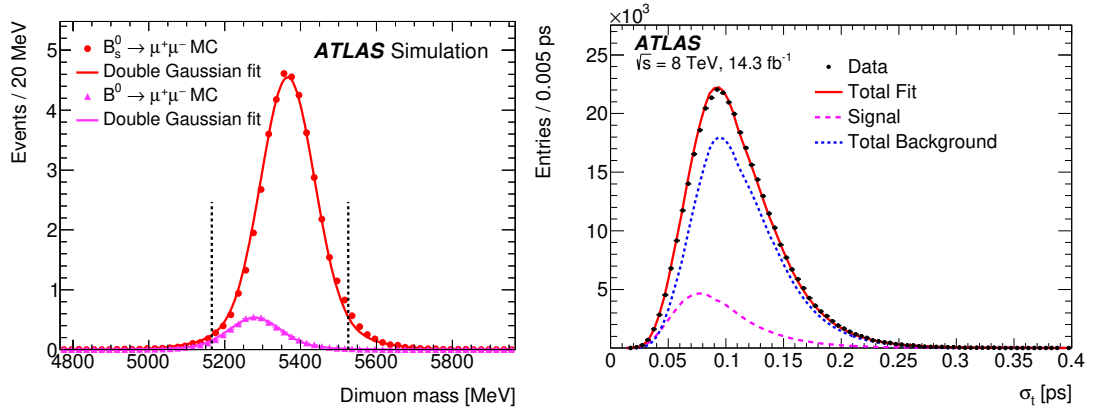
Figure 6: Left [120]: Dimuon invariant mass distribution for the $B_s^0$ and $B^0$ signals from MC simulation of $B_{(s)}^0 \rightarrow \mu^+\mu^-$. The double Gaussian fits are overlaid. The two distributions are normalised to the SM prediction for the expected yield with an integrated luminosity of $25\,\text{fb}^{-1}$. For a homogeneous detector, the distributions would be single-Gaussian. Right [9]: Proper decay time uncertainty distribution for data, the fits to the background and the signal fractions, and the sum of the two fits. For an homogeneous detector, the distribution would be a $\delta$-function.

Before Run 2, the Pixel system was enhanced by a new Insertable B-Layer (IBL) [121, 122], placed just on top of the beam pipe at a radius of $33.5\,\text{mm}$ (while the first Pixel layer is at $50.5\,\text{mm}$). As a consequence, the resolution in $b$-hadron proper decay time measurement has improved by 23% [14].

The lifespan of the ID will end with Run 3 due to the radiation damage. For HL-LHC the detector will be completely replaced by a new all-silicon detector ITk with a pixel subsystem [123] surrounded by a strip subsystem [124]. ITk will have a significantly better granularity to cope with $\langle \mu \rangle = 200$ and thus with an order of more particle tracks for reconstruction. It will also provide improved mass and proper decay time resolution (see Section 8.1). A new High-Granularity Timing Detector [125] will improve the pileup reduction to improve forward object reconstruction, complementing the capabilities of ITk.

## 3.2 Calorimeters

The calorimetry system is responsible for the measurement of the energy of the particles (or jets of particles), providing also spatial information. A particle entering this system creates a particle shower (electromagnetic or hadronic) through interaction with the material of the calorimeters, and most of the particles are stopped in this volume. Exception are muons with energy above a few GeV, and neutrinos. Unlike the tracking system, calorimeters are capable of detecting neutral particles too.

There are two distinct systems. The electromagnetic (el.mag.) calorimeter, which utilizes lead/copper as the absorber and liquid argon as the active medium, is optimized for the measurement of electrons and photons, and contains fine segmentation allowing to distinguish photons from $\pi^0$ decays. The hadronic calorimeter, using iron–scintillator (in barrel) and copper/wolfram–liquid argon (in the end-caps) systems, measures the energy of hadronic particles that are not fully absorbed in the el.mag. calorimeter. The resolution of the el.mag. calorimeter can be expressed as $\sigma(E)/E \simeq 10\%/\sqrt{E[\text{GeV}]} \oplus 0.7\%$ , while for the hadronic calorimeter (in the central region of $|\eta| < 3.2$) the resolution is $\sigma(E)/E \simeq 50\%/\sqrt{E[\text{GeV}]} \oplus 3\%$. The overall coverage of the calorimeters in $|\eta|$ direction is up to 4.9.

13

The HL-LHC upgrades consist of the upgrade of the readout electronics [126, 127].

## 3.3 Muon Detectors

The muons spectrometer (MS) is designed to measure the momentum of muons flying from the calorimetry system. It consists of gaseous tracking detectors, utilizing a number of technologies: Monitored Drift Tubes (MDT), Thin Gap Chambers (TGC), Resistive Plate Chambers (RPC), and Cathode Strip Chambers (CSC). The detectors are placed in a toroidal magnetic field of approximately $0.5\,\mathrm{T}$ and $1\,\mathrm{T}$ (central and end-cap regions). The system covers $|\eta| < 2.7$, although triggering (see Section 3.6) is only available in $|\eta| < 2.4$. The tracks reconstructed by the muon system can be combined with the tracks seen by ID, allowing particle identification and providing a more precise muon+ID track. For low-$p_\mathrm{T}$ muons, it is also possible to connect an extrapolated ID track with a single signal in the muon detectors when the muon track is not reconstructible. While the ID precision dominates in the barrel region, in the end-caps the information from muon detectors improves the resolution in $p_\mathrm{T}$ (and consequently mass). For illustration, the $J/\psi \to \mu^+\mu^-$ mass resolution using ID and/or MS tracks is shown in Figure 7.
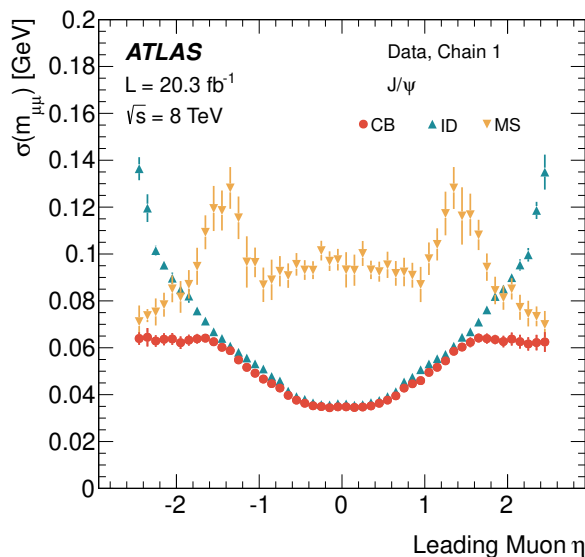


Figure 7: Dimuon invariant mass resolution for CB, MS, and ID muon reconstruction for $J/\psi \to \mu^+\mu^-$ events measured in real data as a function of the pseudorapidity of the highest-$p_\mathrm{T}$ muon. The figure is taken from Reference [128]. MS: muon-spectrometer track only. ID: Inner Detector track only. CB: combined ID+MS tracks.

Although ATLAS calorimeters are designed to absorb the majority of hadrons, there is a small probability that a hadron will either punch-through or decay in-flight to muons (and neutrinos) and the hadronic ID track would be thus misidentified as a muon. This is an important effect, especially in the case of studies of rare muonic decays. In the $B^0_{(s)} \to \mu^+\mu^-$ analysis [120] the $B \to hh$ decays formed a significant background, when the fake probabilities reached 0.4% for kaons, 0.2% for pions, and $< 0.01\%$ for protons. Out of these numbers, only a few percent were real punch-throughs, while the majority of the fakes came from decays in-flight.

Before Run 3, a New Small Wheel detector [129] has been installed, upgrading the forward muon system. For HL-LHC, further upgrades are planned [130], increasing the

number of trigger layers, and using new MDTs (also for triggering). Most electronics will be replaced to handle higher data rates.

## 3.4 Other Detectors

The ATLAS detector is accompanied by three smaller detectors at high pseudorapidities: LUCID and ALFA for luminosity measurements, and the ZDC calorimeter measuring neutral particles.

## 3.5 Particle Identification

From the above description, it is clear that the ATLAS capabilities in particle identification are limited. Missing transverse energy is the signature of neutrinos. The muons and electrons/photons have dedicated systems allowing them to be identified. Muons, in addition, can also be identified by their signature in calorimeters [131], though this is mainly used for trigger purposes. The calorimeters are also capable of identifying heavy particles by their time-of-flight, but the method is mostly applicable to exotic very-heavy particles. TRT is capable of electrons identification through transition radiation. The tracking system itself allows limited hadrons identification via the measurement of energy loss [132]. However, the method is effective only for low momentum of ordinary particles: for protons only up to $p \lesssim 1\,\text{GeV}$, while the ability to distinguish kaons and pions works only up to $p \lesssim 0.7\,\text{GeV}$. For this reason, B-physics analyses do not attempt to distinguish different types of hadrons.

## 3.6 Trigger System

The frequency of collisions and the related data stream is too large to allow storage of every event. Events are thus filtered by Trigger System [133, 134]. Out of the 40 MHz rate, only up to 2 kHz can be stored, when roughly 10% are available for B-physics events/triggers.

The Trigger and Data Acquisition (TDAQ) system selecting potentially interesting events is divided into two main parts: hardware (HW)-based Level-1 (L1) limiting the output rate to at most 100 kHz, and a software-based High-Level Trigger (HLT) assuring the final output rate mentioned above:

- The L1 trigger is based on requirements of simple signatures, as are leptons or jets with transverse momentum/energy above predefined thresholds. The decision needs to be taken in less than 2.5 μs and the subdetectors have to keep full data in a pipeline for such a period. In Run 2, the L1 system was enhanced by *L1Topo* algorithms[9] [135] allowing for the calculation of simple physics quantities of combined objects as invariant mass, opening angles, or missing transverse momentum. The precision of these quantities is significantly limited by the fact that only the minimal momenta/energies of the objects entering the combinations are known, not the momenta/energies themselves.

- The HLT trigger is further separated to Level-2 (L2) and Event Filter (EF)[10]. At L2 only partial event data are available, e.g. ID tracks are reconstructed only in cones around the L1 objects (regions of interest - RoIs), while EF operates with full event information. The HLT algorithms are analysis-like, allowing e.g. to

---

[9]Using Field-Programmable Gate Arrays (FPGA) processors.

[10]A merge of computing farms dedicated to the two levels was made in Run 2, allowing for better resource sharing and HW and SW simplifications. RoI-based reconstruction continues to be used by time-critical algorithms.

reconstruct primary and decay vertices, as well as whole the searched *B*-decay trees. Technically, the algorithms are divided into a feature-extraction part (`FeX`), which constructs the analysis-like objects, and a hypothesis part (`Hypo`) that filters these objects by e.g. their kinematic properties.

The trigger is composed of hundreds of predefined `L1+Fex+Hypo` filtering algorithms (*triggers / trigger items*), which form a trigger menu. It contains trigger items not only for physics studies but also for calibration and supporting purposes such as trigger efficiency measurements. However, the menu is not a static list. The items and their setting need to dynamically react to the variation of the instantaneous luminosity during data-taking. If the output rate of a particular trigger item is too high (the total L1 or HLT rate would exceed the global limits), it needs to be switched off or *prescaled* when only a predefined fraction of the events accepted by the particular trigger item is passed for further processing, while the rest is ignored.

In Run 2 a concept of Trigger Level Analysis [136] was introduced. Such an analysis uses trigger-only objects from the HLT algorithms instead of full offline reconstruction information. The advantage is that the output storage rate can be up to a few tenths of kHz.

## 3.7   Data Processing

The data as taken are organized in *lumiblocks* (several minutes of data taking under the same conditions), *runs* (several hours of continuous *pp* collisions from a single LHC fill), *data periods* (collection of consequent *runs* at similar conditions as trigger menu, etc.) and LHC *Runs* (years of LHC running between technical stops). Moreover, the stored data are divided into *streams* devoted to main physics, delayed reconstruction (which included B-physics), and calibration and monitoring streams. Only data passing a quality review [137, 138] are suitable for analysis. The first cross-checks are made *online*, by shifters during the data-taking, and are based on comparisons of predefined histograms to their reference. After each *run*, an expert performs another cross-check. Several waves of more thorough reviews follow in the next days/weeks, having available (a fraction of) the reconstructed data. As a result, a *Good Run List* (GRL) is provided to the analyzers to avoid including flawed data in their measurements.

The data from the experiment are too large (petabytes per year) to be processed locally, and thus the processing is run at Worldwide LHC Computing Grid [139]. The data in RAW format, which encapsulates signals from the electronics, are reconstructed[11] into Event Summary Data (ESD), containing objects as ID tracks, muon tracks, jets, primary vertices, etc. This intermediate format is then followed by a smaller Analysis Object Data (AOD/xAOD), originally intended for physics analyses, but nowadays followed by even smaller derived formats (DAOD) suitable for specific groups of analyses. All these tasks are performed in the ATLAS software framework ATHENA [140, 141], while individual DAOD analyses then use a variety of tools, though mostly based on the ATHENA and on the ROOT analysis framework [142].

## 3.8   Simulations

Due to the complexity of the detector, readout system, and reconstruction, a simulation of the full experiment is needed to prepare the physics studies. The full ATLAS simulation [143] is chained from the following steps:

- Simulation of the *pp* collisions, using software packages such as PYTHIA8 [144], HERWIG [145], SHERPA [146], and/or combined with process generators like

---

[11]Calibration and detector alignment is performed with the special data streams first.

MADGRAPH [147] or particle decayers as EVTGEN [148]. At the very end of the process, a number of filters can be applied to select the desired events. The result of this process is the genealogy tree of particles created in the collision and gradually decayed into quasi-stable states (particles reaching the detector).

- In the next step, GEANT4 [149] simulates the interactions of the quasi-stable particles from the previous step with the matter of the material, i.e. processes such as ionization, nuclear collisions, etc. The output of this stage is the collection of energy losses along the path of the particles in the detector. The effect of possible external magnetic field is included.

- The energy losses are then converted into the expected output signals from the electronics. This *digitization* step uses software tailored to the subdetectors. The result is then an event in a format equivalent to or the same as the real RAW data from the experiment.

- Hereafter, standard ATLAS reconstruction and analysis follows, allowing to study desired physics signal signatures in the detector as well as possible background processes.

Since the full simulation, as described above, is slow (up to several minutes per event), alternative approaches were developed to speed it up. These are based on a parametrized description of the detector efficiencies and resolutions (the parametrization is, though, obtained from the full simulations), merging and replacing the GEANT4 and digitization (and possibly also reconstruction) steps. Examples of such fast simulation frameworks are ATLFAST [150] and DELPHES [151].

Despite the complexity of the full simulation chain, differences between real data and simulations are always present, originating in imprecise physics process simulations and necessary simplifications in the digitization process. Simulated data thus have to be confronted with real data using control channels, and corresponding corrections need to be applied.

## 3.9 Physics Program

The physics program of the ATLAS experiment is broad, including both SM measurements as well as searches for New Physics. The experiment is divided into physics groups focusing on Higgs boson, top quark, B-physics, and other Standard Model measurements, while New Phenomena are directly searched by Supersymmetry and exotics group. Specific groups are analyzing heavy-ion collisions and preparing physics studies for the next stages of the experiment.

Another set of groups is providing supporting performance studies for the reconstructed objects (ID tracks, electrons, photons, muons, tau reconstruction, jets, missing energy, flavour tagging), developing simulations and physics modeling, studying trigger, data quality, preparing software, and care about the various subdetectors.

# 4 B-physics at ATLAS

## 4.1 B-Physics Program

The B-physics program at ATLAS dynamically focuses on topical analyses in the field heavy of flavour physics. The rate of production of $b\bar{b}$ pairs at LHC in the *pp* collisions reaches several millions per second (varies with $L_{int}$ and $\sqrt{s}$), which makes LHC a B-factory. The precision of reconstruction at ATLAS, as described in Section 3.1, provides satisfactory performance for a wide variety of HF studies. However, in order to utilize these facts, the $b\bar{b}$ events (B-events) need to be efficiently selected by the trigger system, and the studied $B$-decays need to be distinguished from the harsh background coming from pileup and other hard-scattering processes. The former requirement requires maintaining as low-$p_T$ thresholds as possible at the trigger level while keeping the output rate within allowed limits for B-physics. This is reasonably achievable predominantly with the purity of the muon system (exceptions exist, as described later). The latter requirement, the suppression of background, pushes the program towards the studies of $B$-decays that are fully reconstructable (at the very final state) by the ATLAS tracking system. Escaping neutrinos or photons or other neutral particles allow for partial $b$-hadron mass reconstruction only, which makes distinguishing the signal from the background difficult (again, there were a few exceptions in the B-physics program, typically dealing with soft escaping neutrinos or photons).

The B-physics program at ATLAS can be divided into the following categories:

- **Rare $B$-decays:** studies of known rare processes that are potentially sensitive to NP contributions. The decays are suppressed in SM by various mechanisms, while these might not exist in NP scenarios. The (differential) branching ratio can thus be significantly modified: BR can be both enhanced or suppressed, or the decay topology can be significantly different from SM prediction. ATLAS measurements include FCNC muonic $B$-decays, lepton flavour universality tests, or search for lepton flavour violating (LFV) decays. The analyses typically work with a handful of signal events (if any).

- **Precision measurements with $B$-decays:** studies of processes with relatively high BR, providing large data samples for the analyses (up to hundreds of thousands of signal events). A precise determination of the properties of the $B$-decays allows for a thorough test of the SM predictions. The B-physics group at ATLAS has studied oscillations of $B_s^0$ and $B^0$ mesons or helicity amplitudes in decays of $\Lambda_b$. The analyses are quite complex, utilizing multidimensional fits to the variables describing the decays.

- **HF spectroscopy:** studies of double-heavy flavoured $B$-mesons as $B_c^+$, search for new decay modes, for new excited states of $b$-hadrons, or search for and studies of exotic states as tetra/pentaquarks. All these measurements put the QCD predictions for the production cross section, BR, and/or mass spectrum of these particles into a test.

- **HF production:** measurement of the production cross section of $b/c$-hadrons, including quarkonia ($J/\psi$, $\psi(2S)$, $\Upsilon$, $\chi_c$). Furthermore, studies of correlations between $b$-hadron pairs or of $b$-hadrons with jets are also performed. The results of the measurements are compared to QCD predictions (utilizing approaches such as Non-relativistic QCD or Fixed-order Next-to-Leading Logarithm, production as a color-singlet- or color-octet-based states) and allow testing simulation of these processes with standard MC generators. A special subpart of this ATLAS B-physics program are the analyses of the associated production of HF (typically

quarkonia) with other objects as $W$ or $Z$ bosons, or di-$J/\psi$ production. Besides the QCD tests these analyses also allow to measure the effective cross section of double-parton scattering, when the two objects are produced from two different parton pairs. All these measurements help to understand the HF backgrounds in other non-B-physics ATLAS analyses.

- **Validation studies:** cross-checks of properties (mass, lifetime) of well-known $B$-decays in order to study and validate the reconstruction performance of the ATLAS detector and/or the base event-selection procedures. These studies typically include $J/\psi \rightarrow \mu^+\mu^-$, $B^+ \rightarrow J/\psi(\mu^+\mu^-)K^+$, $B^0_s \rightarrow J/\psi(\mu^+\mu^-)\phi(K^+K^-)$ or $B^0 \rightarrow J/\psi(\mu^+\mu^-)K^{*0}(K^+\pi^-)$ decays, checking the performance in different parts of the detector.

The results of the ATLAS B-physics group are summarized at ATLAS public web page [152].

## 4.2 Data Processing and Analysis Chain

A typical data processing and analysis chain of the measurements in the ATLAS B-physics group consists of the following steps. The HF events produced in the $pp$ collision are first selected by the B-physics trigger system, following a base data quality review as described in Section 3.7. The accepted events are then reconstructed by the ATLAS offline software (offline reconstruction): hits in the tracking and muon system are reconstructed into curved particle tracks, energy deposits in calorimeters into jets, electron and photon objects, and primary vertices are reconstructed from the ID tracks. Information about all active triggers and their connection to the offline-reconstructed objects is also made available. The $b$-hadron decays are searched by trying to reconstruct their decay vertex (secondary vertex SV) using the ID tracks of the daughter particles (daughter tracks). This procedure is generally called *vertexing*. Once the reconstructed decays are available, a selection procedure follows to suppress combinatorial background. A statistical analysis of such signal-enriched samples is then performed, and systematic uncertainties (systematics) are evaluated. The latter steps are supported by full MC and toy-MC simulations, training the analysis procedures, determining signal efficiencies, or contributing to the evaluation of systematics.

### 4.2.1 Heavy Flavour Production at LHC

The total cross section of $pp$ interactions at LHC is around $100\,\text{mb}$, out of which roughly a quarter corresponds to the elastic $pp$ scattering [153–155]. The total cross section of $b\bar{b}$ production at LHC at nominal $\sqrt{s}$ is $\sim 300\,\mu\text{b}$ [156] (see also Figure 8 right), while $\sim 30\,\mu\text{b}$ are within the limited fiducial acceptance for typical B-physics analysis ($p_\text{T} > 9\,\text{GeV}$, $|\eta| < 2.5$) [157, 158]. In the $pp$ collisions at LHC the $b$-quarks are created via four mechanisms: flavour creation, flavour excitation, and gluon splitting, with the latest being the dominant one at LHC [159]. Examples of the Feynmann diagrams of the three processes are shown in Figure 8 (left). The hadronization process allows for the production of not only $B^0$ and $B^+$, but also for $B^0_s$, $\Lambda_b$, and other heavier/excited states such as $B^+_c$, and even allows for the search for new states and for penta/tetraquarks. The predominant $b$-hadrons are roughly produced with the following ratios: $f(B_s) : f(b - \text{baryon}) : f(B^0) : f(B^+) \simeq 0.1 : 0.1 : 0.4 : 0.4$ (but in reality the ratios are slightly dependent on $p_\text{T}$ of the hadrons) [160].
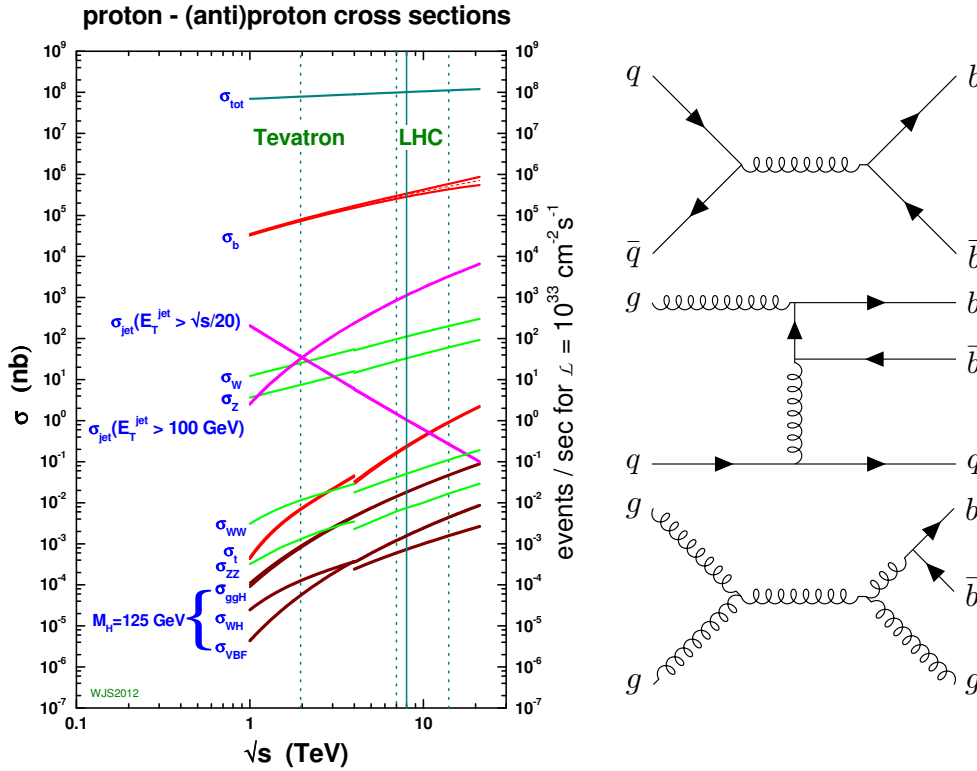
Figure 8: Left: Cross sections of selected processes versus centre-of-mass energy in *pp* collisions. Right: Example Feynmann diagrams for (from top to bottom) flavour creation, flavour excitation, and gluon splitting. A full list of the leading diagrams can be found e.g. in Thesis [159].

### 4.2.2 B-Trigger

The B-physics trigger [161] menu consists of a number of items dedicated to the (groups of) various analyses, focusing on low-$p_\mathrm{T}$ muon triggers for reasons mentioned earlier. The B-trigger items can be categorized as follows:

- **Pure dimuon triggers** form the core of the B-physics triggers. At L1 the MS is required to detect two muon thresholds of a few GeV. At HLT the two muons are confirmed by precision detectors and associated reconstructed ID tracks are used to check that they come from common decay vertex (vertexing). Finally, only dimuon candidates out of a certain invariant mass range are rejected. These triggers collect $J/\psi$, $\psi(2S)$, $\Upsilon$, $B^0_{(s)} \to \mu^+\mu^-$ and $B \to J/\psi X$ decays as well as (partly) nonresonant $b \to s\mu\mu$ transitions. The spectrum of such events in real data is shown in Figure 9.

- **Dimuon triggers with *B*-decays reconstruction** are used to further suppress the HLT rate by trying to reconstruct the full *B*-decay, i.e. also including the hadronic tracks seen by ID and constructing the *B*-decay vertex. The algorithm is close to the procedures used in the offline reconstruction.

- **Multimuon triggers** allow searches for 3-muon signatures used for di-onia production or for LFV $\tau \to \mu\mu\mu$ decays.

- **The Supporting and calibration triggers** are devoted to efficiency measure-

ments of the main B-physics triggers. The efficiency of (B-)triggers could be evaluated from MC simulations or from real data using the tag-and-probe method: using known decays as $J/\psi \to \mu^+\mu^-$ and a single-muon-based trigger, one can determine the efficiency of detecting the other (non-triggered) muon in the decay. Other features such as vertexing at HLT are evaluated by using supporting triggers without the vertexing included. These supporting triggers are always heavily prescaled as the relaxed conditions would lead to unacceptable output rates.

At L1 the lowest possible thresholds for the $p_\mathrm{T}$ of the two muons were $4\,\mathrm{GeV}$. However, with the rising average $L_\mathrm{int}$ the rate at L1 became too high and higher-threshold triggers were implemented, combining 4, 6, and $11\,\mathrm{GeV}$ thresholds. Furthermore, in Run 1 barrel-only L1 configurations were implemented, collecting only muons in the central part of the detector where the reconstruction performance is the best. In Run 2 the *L1topo* was used extensively. The beam intensity and thus $L_\mathrm{int}$ is not constant during a *run*, as depicted in Figure 10, but slowly falls from an initial maximum at the start of data-taking. Such a "decaying" $L_\mathrm{int}$ allows for switching on or lowering prescale factors of high-rate trigger items towards the end of each LHC fill. B-physics greatly benefited from this feature, filling a significant part of the output rate of that End-of-Fill (EoF) period.

In Run 2 dielectron trigger items were introduced to collect $B^0 \to K^{*0}e^+e^-$ events for the $R(K^*)$ measurement. Part of them was based on the combination of muon and electron signatures but had to be prescaled to keep the rate low. The other, more important part of the dielectron triggers, had a special configuration: they did not rely on a specific L1 trigger but instead took all events passing any (or large subset of) items of the L1 menu (i.e. L1 not specifically designed for the $B^0 \to K^{*0}e^+e^-$ analysis). Then searched for the signal decay at HLT.

Often, *b*-hadrons are present in events triggered by non-B-physics specific triggers, e.g. jet or single-muon triggers. Also, due to the fact that (anti-)*b*-quarks are created mostly in $b\bar{b}$ pairs, triggering on a specific signal *B*-decay means that there is also another *B*-decay in the same event. Thus it is possible, in general, to search for any *B*-decay modes in the collected data, although they would naturally be suppressed by their BR. Such a *parasitic mode* would allow for limited analyses of hadronic *B*-decays. However, the potential has neither yet been fully studied, nor utilized.

### 4.2.3 Offline Reconstruction and Vertexing

The B-physics analyses (B-analyses) rely mostly on the *b*-hadron daughter tracks reconstruction by the ID and muon identification by the MS. Despite the fact that the ID+MS combination improves the $p_\mathrm{T}$ resolution of tracks in the end-caps, many B-analyses use ID-track parameters only (for simplicity), utilizing MS just for the muon identification. In order to ensure high quality and control efficiency of the provided ID and MS tracks, the corresponding combined-performance (CP) groups provide recommendations on (muon) tracks selections that B-analyses follow.

A key reconstruction-wise step of the B-analyses is the reconstruction of secondary *B*-decay vertex (B-vertex) using the tracks of the daughter particles. This vertexing procedure finds out a probability, whether a set of tracks could originate in a common space point (within the uncertainties of the track parameters), and also finds the most probable vertex position. The lifetime of *b*-hadrons (mean $\sim 1.5\,\mathrm{ps}$ at ATLAS [162]) prolonged by relativistic effects is long enough for them to fly up to several millimeters away from the *pp* interaction, but at the same time is short enough so that they decay before the first detection layer of the tracking system. The B-physics group uses a vertexing algorithm based on the Kalman filter approach, VKALVRT [163]. The
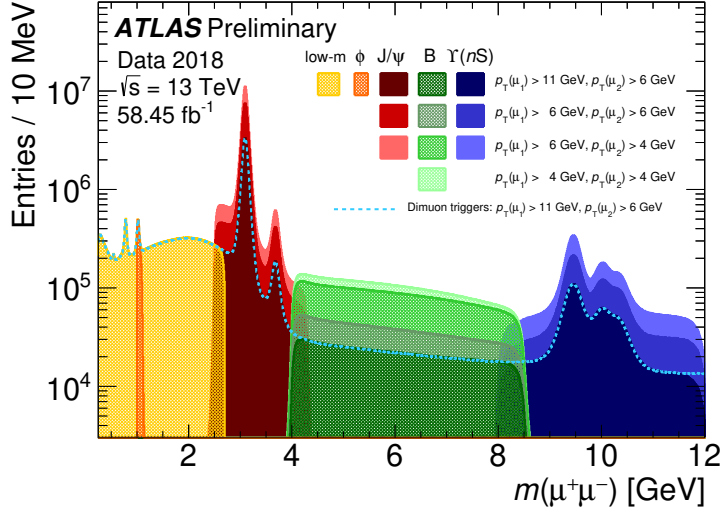
Figure 9: Invariant mass distributions for oppositely charged muon candidate pairs that pass various dimuon triggers, using 2018 data. Figure taken from public B-trigger web-page [161].

procedure can be more complicated by the fact that many $B$-decays include cascades when the intermediate particles can also have non-negligible decay times. An example of such a cascade is $B^0 \to J/\psi(\mu^+\mu^-)K_s^0(\pi^+\pi^-)$ decay when the $K_s^0$ meson can fly tenths of centimeters (for an illustration of the efficiency of reconstructing such long-lived particles, see Figure 11 left). The VKALVRT software also allows the application of additional constraints. A typical constraint is on the invariant mass of a subset of tracks (*mass constraint*), used e.g. for $B \to J/\psi(\mu^+\mu^-)X$ decays: the $J/\psi$ mass is known very precisely and its natural width is $\sim 100\times$ smaller than the detector resolution. The requirement that the invariant mass of the two reconstructed muons matches the world-average [160] $J/\psi$ mass thus significantly improves the resolution of the reconstructed $b$-hadron, as illustrated in Figure 11 (right).

The primary $pp$ collision vertices are reconstructed using similar algorithms [164]. In B-analyses it is important to know the PV in which the $b$-hadron was born, but since it decays away from PV, the determination of the associated PV is not trivial. B-analyses usually use the following methods:

- Select that PV, which is closest to the line extrapolated in the opposite direction of the reconstructed $B$-momentum from the reconstructed B-vertex towards the beam spot (the place where the $pp$ interactions accumulate). The method is also called a method of minimal 3-dimensional impact parameter and is the most frequently used by the B-analyses. The rate of selection of wrong PV is below percent [**9**].

- Because the beam spot is very narrow in the transverse direction (tenths of micrometers) but wide in $z$ (centimeters) as depicted in Figure 12, a selection based on minimal $z$-distance between PV and B-vertex also usually gives the correct answer.

- Most of the $pp$ interactions are not hard in the sense of energy released in the transverse plane. Selecting the PV with the highest sum of $p_T$ of the tracks out of which the PV was reconstructed thus also has a high probability of being the one in which the $b$-hadron was born.
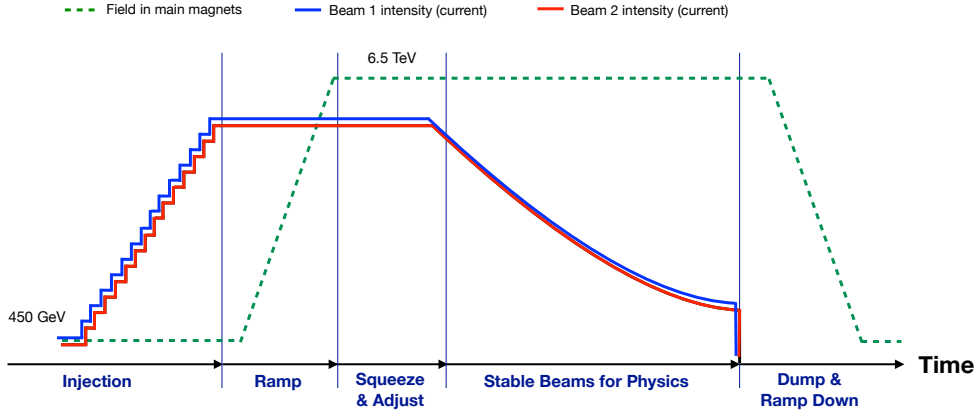
Figure 10: The LHC goes through a cycle composed of several phases: the injection of beams into the rings, the acceleration to the collision energy during ramp, the preparation of beams for collisions during squeeze and adjust, the phase where collisions take place during stable beams, the extraction of the beams from the rings during dump, and finally the ramping down of the magnetic fields. Taken from Reference [138].

All these three methods are illustrated in Figure 12. Since the daughter tracks of the signal $B$-decay candidate can be accidentally used in a PV construction, in B-analyses all the PVs are refitted by removing the signal daughter tracks first.
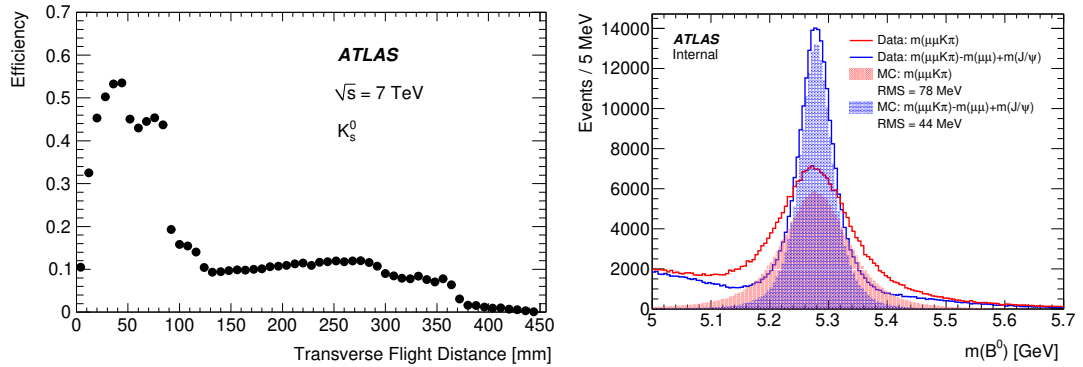


Figure 11: Left: The reconstruction efficiency of $K_s^0$ candidates in the 7 TeV MC sample versus the transverse flight distance [165]. Right: $B^0$ mass reconstructed with and without the $J/\psi$ mass constraint using $B^0 \rightarrow J/\psi(\mu^+\mu^-)K^{*0}(K^+\pi^-)$ decay candidates of the control channel of analysis in Reference [12]. A simulation of the control channel is shown with the filled histograms.

### 4.2.4 Event Selection

The filtering of events in order to obtain signal-enriched sub-sample of data is typically using the following variables:

- Kinematics of the signal particle candidate or its decay products. Typically $p_\mathrm{T}$ above a certain threshold is helping in suppressing combinatorial backgrounds from the huge amount of low-$p_\mathrm{T}$ pileup tracks.

- Invariant mass of the signal particle candidate or its intermediate unstable decay products. The selected mass range typically relates to the detector mass resolution.
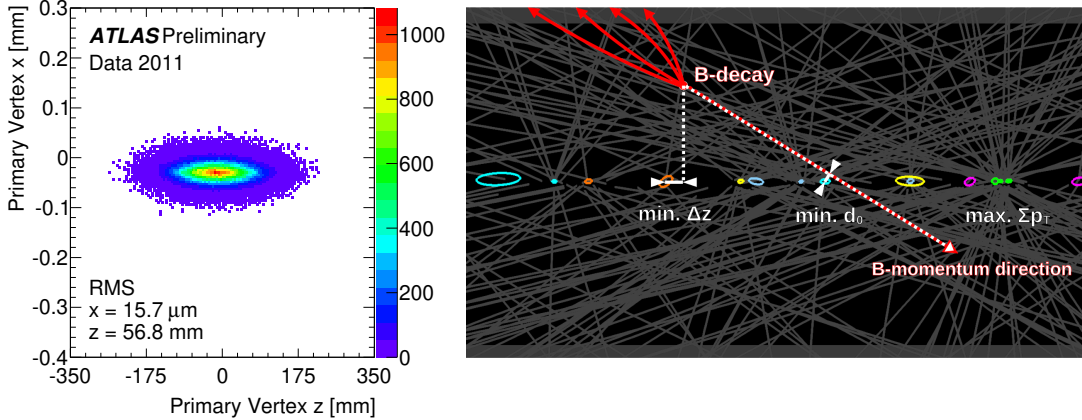
Figure 12: The distribution of PV in 2011 data in the $xz$-plane [166], illustrating the beam spot size. The distribution in $y$-direction is similar to the one in $x$. The schematic figure illustrates the three PV selection methods used in B-analyses: minimal impact parameter $d_0$, minimal $\Delta z$ separation and highest $\sum p_T$ of tracks forming the PV (in reality the B-vertex is much closer to the line of PVs (colored ellipses) and thus the three methods often agree on the selected PV).

- Quality of the reconstructed secondary ($b$-hadron) vertices by means of the $\chi^2$ per number of degrees of freedom (NDF) of the vertex-fitting procedure. The position of the decay vertex, or the calculated $b$-hadron proper decay time (or its significance[12]) can also be a subject of selection.

- Pointing of the $b$-hadron momentum towards the PV: the angle between the $b$-hadron momentum vector and the vector of direction from SV to PV.

- Isolation of the signal particle by vetoing events with close (in terms of the direction of flight) activity in the tracking system and/or calorimeters.

For precision measurements and production cross section studies, where the expected amount of signal events is high, a simple cut-based selection is usually used. Although not having the best performance in signal-to-background (S/B) ratio optimization[13], it simplifies the control over the selection procedure (cut efficiencies, etc. can be easily tested on MC simulations). The search for rare or even forbidden processes usually utilizes multivariate selection techniques such as Boosted Decision Trees or Neural Networks in order to achieve as good as possible expected signal significance. The precision measurements often keep a solid portion of background in order to better control its description, and the optimization procedure rather targets the smallest expected uncertainty on the physics parameter(s) of interest.

Special treatment needs to be applied for the cases where multiple signal particle candidates are found in a single event. If they share no common parts (such as reconstructed tracks), they can be all kept. However, if the candidates are not independent, usually just one of them is retained for further analysis. The selection is typically based on the lowest $\chi^2$/NDF of the SV; other possibilities include the highest $p_T$ of the candidate.

---

[12]Proper decay time divided by its uncertainty originating from the uncertainties of the reconstructed ID track parameters.

[13]The optimized expression is not literally the ratio of the number of signal events to the number of background events, but the formulas are analysis-dependent.

### 4.2.5 Statistical Analysis

A statistical analysis, specific to each B-analysis, is used to extract the physics quantities of interest. In order to avoid (unintended) bias in the analysis procedures, the quantities of interest or the relevant part of data are usually blinded, so that preliminary results are not seen until all analysis steps, including all uncertainties evaluations, are fixed.

The signal separation and extraction of physics parameters are done by fits to relevant data distributions. While a minimum $\chi^2$ fit to binned distribution is the simplest basic tool, B-analysis more commonly uses an unbinned (extended) maximum likelihood (UML) fit [167], allowing for a better description of small data samples. The method relies on probability density functions (PDF) that describe the probability distribution of the signal and background components. The typical form of the (log-)likelihood function is:

$$\ln \mathcal{L}(\theta) = \sum_{i=1}^{N} \Big[ w_i \cdot \ln \big( \sum_s f_s \cdot \mathcal{F}_s(m_i, t_i, \Omega_i, \ldots, \theta) + \sum_b f_b \cdot \mathcal{F}_b(m_i, t_i, \Omega_i, \ldots, \theta)) \Big] \quad (5)$$

where $\mathcal{F}_s$ and $\mathcal{F}_b$ are the PDFs of the signal(s) and background(s), which depend on the physics and nuisance parameters $\theta$ and the observables extracted from data such as the mass $m_i$, the proper decay time $t_i$ or the decay angles $\Omega_i$. The fractions $f_s$ and $f_b$ represent the relative contributions of the signal(s) and the background(s) in the statistical fit model (the sum of all the fractions is unity). Weight $w_i$ can be used to account for possible detector inefficiencies if necessary. The likelihood is maximized in terms of $\theta$. When building the whole fit model, it is important to check that the correlations of the various observables are properly described.

The cross section measurements and searches for new states and decays usually use invariant-mass-only fits, separating a Gaussian-like signal from a flat-like background. When the separation of long-lived components is needed, another observable is added: a (pseudo)proper[14] decay time is:

$$t = \frac{L_{xy} \, M}{c \, p_{\mathrm{T}}} \quad (6)$$

where $p_{\mathrm{T}}$ is the reconstructed transverse momentum of a $b/c$-hadron and $M$ is its mass. The transverse decay length $L_{xy}$ is the displacement in the transverse plane of the $b/c$-hadron decay vertex from the PV, projected onto the direction of the $b/c$-hadron transverse momentum. An illustration of projections of such a 2-dimensional (2D) mass-proper-decay-time fit is shown in Figure 13.

Searches for new decays usually deal with no signal or signals of small significance. The likelihood allows for the determination of the significance using the likelihood ratio method [169], as an alternative to evaluation via toy-MC experiments. In case of no signal, upper limits on the production of the states can be set via an asymptotic approximation from the profile likelihood formalism based on $\mathrm{CL}_s$ frequentist method [170, 171].

Precision measurements are often multidimensional, including decay angles or other variables. Special cases of such additional variables are per-candidate resolutions of reconstructed mass or proper decay time. Propagating the known uncertainties of the particle track parameters ($p_{\mathrm{T}}$, $\eta$, $\phi$, $d_0$, $z_0$) and their correlation matrix, one can calculate the uncertainty of the invariant mass of a combination of tracks. Similarly, using in

---

[14]In the analysis of $J/\psi$ production, the particle can either be produced directly in $pp$ collision (prompt production) or can come from decays of long-lived particles as $b$-hadrons (non-prompt component). In the latter case, the measured $J/\psi$ decay time is not related to the $J/\psi$ lifetime, but to the lifetime of the mother $b$-hadron. Thus the usage of the *pseudo* prefix.
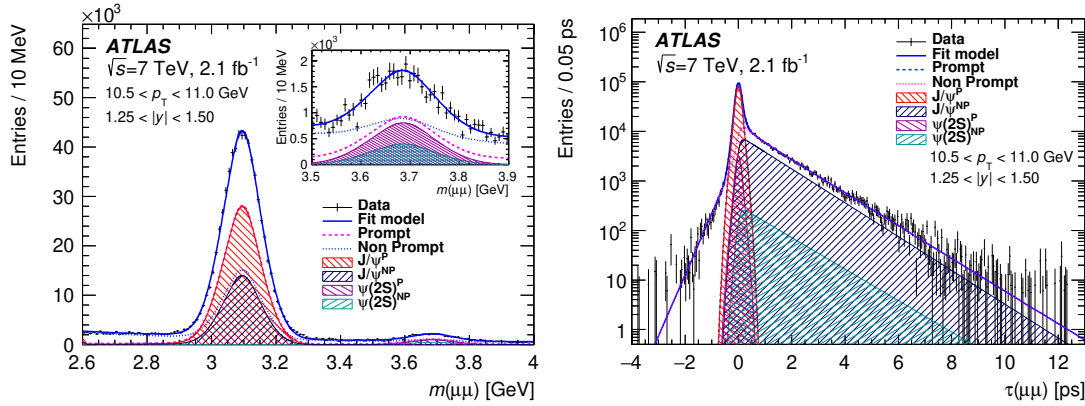
Figure 13: Mass (left) and pseudo-proper decay time (right) projections of a 2D mass-time UML fit of dimuon candidates in the measurement of $J/\psi$ and $\psi(2S)$ production cross section in $pp$ collision data at $\sqrt{s} = 7$ TeV [168]. The signal components for $J/\psi \to \mu^+\mu^-$ and $\psi(2S) \to \mu^+\mu^-$ are divided to prompt and non-prompt parts and shown separately as well as the total signal+background prompt and non-prompt components.

addition uncertainties of the PV and SV position and their correlations, a proper decay time uncertainty, individual to each $b/c$-hadron candidate (thus *per-candidate*), can be obtained. Due to the cylindrical geometry of the ATLAS detector, the resolution of the particle track parameters strongly depends on the $\eta$-direction of flight of the particle, and so do the mass and proper decay time uncertainties. The signal peaks are thus multi-Gaussian. In the fit model, such peaks can be approximated by double/tripper-Gaussian, modified Gaussian [157, 172], or Johnson's SU [173, 174] distributions. Another approach is to use MC simulation-based templates. However, one can also utilize the known per-candidate resolutions to construct a multi-Gaussian distribution (each event has signal Gaussian PDF with width defined by the per-candidate uncertainty) that should exactly match the data[15]. To properly include these new observables ($\sigma_{m_i}$, $\sigma_{t_i}$) into the likelihood, their distribution for signal and background events must be estimated, typically using the sideband-subtraction method or SPLOT technique [175]. Otherwise, one can encounter unexpected biases in the fit parameters [176].

The fact that the UML fits are unbinned complicates the assessment of the quality of the fit, while in fits utilizing $\chi^2$ minimization the $\chi^2/\text{NDF}$ ratio provides the measure of the quality. Therefore, the validity of an UML fit results is verified by evaluating $\chi^2/\text{NDF}$ of various projections of the fit, or by comparing fitted data with the toy-MC data generated from the UML fit model.

### 4.2.6 Monte Carlo Simulations

MC simulations of the signal decays are used to study the efficiency and acceptance effects: efficiency of the selection, efficiency of trigger and reconstruction, sculpting of decay angles by the kinematic cuts on the daughter particles, and self-background - the fake signal candidates in an event where real signal decay is present. The self-background typically appears as a consequence of a combination of part of the signal decay with other (random) tracks from the same event, mimicking the signal signature.

Background MC samples are then used to study the rejection of fake signals coming either from accidental random combinatorics of tracks or from dedicated $B$-decays

---

[15]In reality a common scale factor is used to scale the uncertainties to account for imperfect estimate of track parameters uncertainties.

typically having the same or similar topology as the signal, but differing in the type of particles (due to the missing hadron identification capabilities of ATLAS). An example of such a pair of signal–dedicated background is $B_s^0 \to J/\psi(\mu^+\mu^-)\phi(K^+K^-)$ and $B^0 \to J/\psi(\mu^+\mu^-)K^{*0}(K^+\pi^-)$ pair of decays, both having two muons plus two tracks signature. The $B^0$ decay can thus easily mimic the $B_s^0$ one (and vice versa). Assigning kaon mass to the pion track from the $B^0$ decay would lead to the deformation of the fake $B_s^0$ candidate invariant mass distribution. MC simulation allows to describe such effects and include them in the statistical analysis.

B-Physics simulations typically use the PYTHIA-based wrapper PYTHIA8B [177] combined with the EVTGEN decayer. PYTHIA is tuned with ATLAS data, using the CTEQ6L1 set of parton distribution functions [178] and the A14 parameterization [179]. The PYTHIA8B wrapper allows forcing desired signal $b/c$-hadron decays. Since the generation and filtering of $b\bar{b}$ events is slow (up to minutes per event), the wrapper utilizes several mechanisms to speed up the process by reusing parton part of a previous simulation (repeats hadronization process) or by re-decaying $b$-hadrons to reach desired final state (including kinematic requirements based on typical B-trigger and ID acceptance). EVTGEN[16] is providing a precise description of (not only) $B$-decays by accounting for the proper matrix elements of the processes and for the quantum numbers of the particles involved in the decay tree.

### 4.2.7 Systematic Uncertainties

The used analysis techniques, approximations, statistical methods, simulations, and knowledge of the detector performance are always burdened by uncertainties, leading to systematic uncertainties of the extracted physics parameters. While the list of systematics is very specific to each B-analysis, the most common ones, together with their assessments, are listed below.

The **luminosity** is measured with precision at the level of a few percent [180– 183] and naturally contributes to the uncertainty of the measurements of $b/c$-hadron production.

The **detector acceptance** (the coverage in $\eta$ and the minimum $p_T$ on the reconstructed tracks) significantly affects both the total "seen" production cross section and the topology of the decays, i.e. the distribution of the $b/c$-hadron decay angles. The detector acceptance is evaluated using MC simulations (after corrections for differences between data and MC, as described later). The limited size of the MC sample, though significantly larger than the real data, imposes a statistical uncertainty on the extracted acceptance distributions. Further uncertainties can come from chosen binning or chosen empirical fit functions used to smooth the acceptance distributions.

The measurements are also affected by **trigger and reconstruction efficiencies or misidentification rates** of the various objects such as ID or muon tracks. While the offline reconstruction efficiencies (tracks that passed trigger and are within the ATLAS detector acceptance) are close to unity, the trigger ones are lower, especially at L1 where a few tenths of a percent are typically lost. These efficiencies are known with a limited precision, which then propagates to the results of a given B-analysis. The misidentification rates are usually cross-checked with real data using well-known (and high-rate) decays where such a rate can be measured (e.g. $B^+ \to J/\psi(\mu^+\mu^-)K^+$ to measure kaon-muon misidentification).

The analysis has to be robust to the **event selection**. Although it is optimized to obtain the best possible precision from the data, it needs to be checked that the selection of events (either in signal or control or normalization regions) does not bias the result,

---

[16]I have contributed to this SW framework with the decay model `Lb2Lll` for the semileptonic rare decay $\Lambda_b^0 \to \Lambda^0\mu^+\mu^-$.

i.e. that slight variations of the selection do not lead to inconsistent results. In the case of the existence of **multiple signal candidates** ($N_{\mathrm{cand}}$) in a single event, the procedure of choosing just one can lead to biases in the measurement too. The related systematics can be evaluated by keeping all such candidates in the analysis, while weighting them by a factor of $1/N_{\mathrm{cand}}$, and checking the effect on the given B-analysis results.

The **statistical fit model** is usually only an approximation of the real data distributions, especially as what concerns detector resolution and combinatorial background components. The systematic uncertainty is evaluated by using alternative fit models, still fitting the data well (e.g. higher-order polynomials for the combinatorial background, or the variations of the multi-Gaussian detector resolution description mentioned in the previous section). The systematics can be obtained either by applying the alternative fit models on the real data or by generating toy-MC data from the alternative models and fitting them by the default fit model.

The UML **default fit model** can suffer from **intrinsic biases**, the more the fit model is complicated (from the point of view of a number of dimensions and physics and nuisance parameters) and the less the amount of data to fit is available. A fit of a set of toy-MC datasets (toy-data) generated from the fit model is used to obtain this bias. Ideally, the result ($\theta_{\mathrm{fit}}$) of each physics parameter $\theta$ extracted from these toy-data fits should be distributed following a Gaussian shape with the mean value corresponding to the physics parameter value used for the toy-MC data generation ($\theta_{\mathrm{init}}$) and the width of the Gaussian should be equal to the statistical uncertainty of the physics parameter ($\sigma(\theta)_{\mathrm{stat}}$) extracted from the fit(s). It is a self-consistency check, presented by a set of *pull-plots*: plots of $(\theta_{\mathrm{fit}} - \theta_{\mathrm{init}})/\sigma(\theta)_{\mathrm{stat}}$ that should follow the normal distribution $\mathcal{N}(0,1)$ in the case of no bias. An example of such a plot and its interpretation is shown in Figure 14.
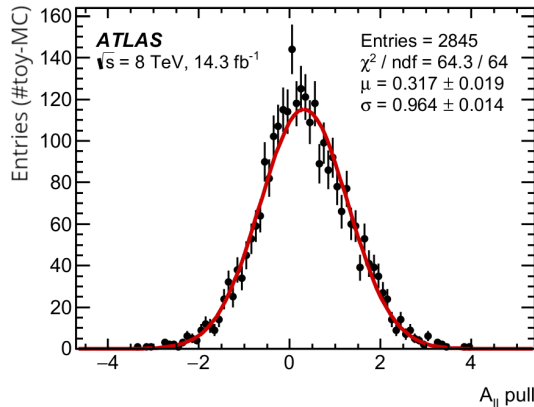


Figure 14: Pull distribution of $A_{||}$ parameter in $B_s^0 \to J/\psi\phi$ analysis [9], suggesting that the real value of physics parameter $A_{||}$ would be shifted up by $\sim 32\%$ of the statistical error with respect to the $A_{||}$ value obtained from the fit on real data. Also, the statistical error of $A_{||}$ in the real data fit will be slightly overestimated, by around 4%.

There are always **differences between MC simulations and real data**, originating either in the particle collision generator and particle decays levels, or in the simulation of detector response. The former, including differences in $b/c$-hadron $p_{\mathrm{T}}$, $\eta$, invariant mass, lifetime, decay angular distribution, other activity in the events (pileup, isolation of signal particles), etc. can be corrected by applying weights calculated from real data, e.g. on control channels. The detector simulation is corrected by *scale factors* provided by the corresponding CP groups. All these corrections have associated uncertainties that then propagate to the given B-analysis. Sometimes the properties of

the studies signal or background particles are not known (e.g. initial polarization or decay angles). In that case, the systematics is evaluated by associating several extreme (but physical) configurations to the unknown properties and checking the effect on the whole B-analysis.

The B-analyses are often using **external inputs** such as BR of control, normalization or dedicated-background channels, or other properties of particles. These have uncertainties and propagate to the given B-analysis systematics.

**Dedicated backgrounds** are usually simulated in MC and corresponding PDFs are plugged into the statistical model (with uncertainties coming from the data-MC differences and external inputs described above), while combinatorial backgrounds are often described by empiric PDFs and systematics are connected with those PDFs alternation.

The **residual detector misalignment** and precision of knowledge of the **magnetic field** in the tracking system impose systematics on the measurement of track parameters. The former is related to the uncertainty of knowledge of the position and geometry of the tracking system. As it measures the position of the passing charged particles with a precision at the level of $10\,\mu\text{m}$, knowledge of the geometry needs to be known at a similar level. This is achieved using real data from collisions and cosmic muon rays, but the procedure has limited precision, leading to the residual misalignment. As a result, the $p_{\text{T}}$ and position of the secondary $B$-decay vertex can be systematically shifted. A relatively simple back-on-envelope estimate of the uncertainty can be made by using known (measured [184]) momentum scale bias from reconstructed invariant masses of well-known particles as $J/\psi$ and translating it into a bias in measurement in a given B-analysis. A more sophisticated method [29] measures the biases in real data and misaligns MC simulations so that the observed biases are similar in size and structure (see Figures 15). Such a misaligned MC data sample of signal events is then used to assess the systematics.
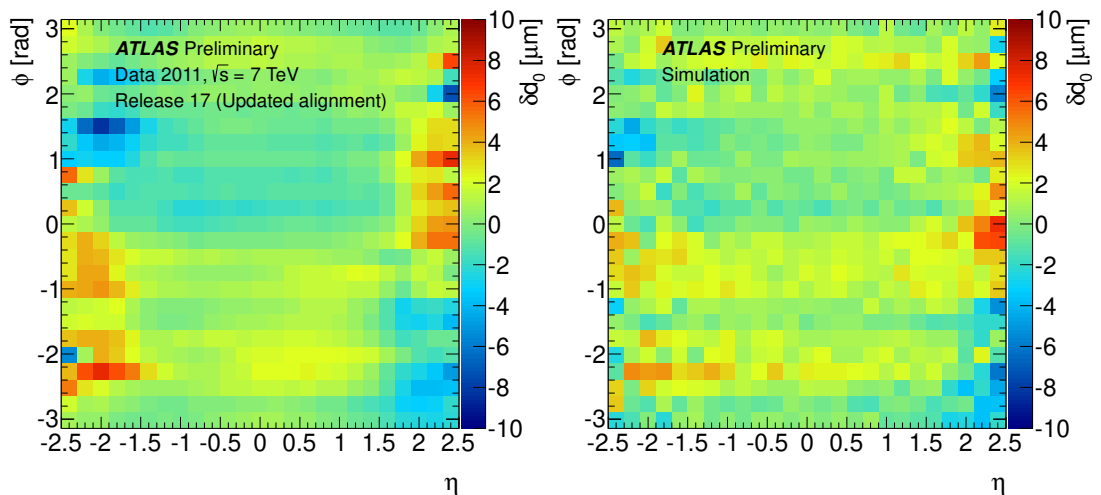


Figure 15: The fitted mean value (the bias) of the impact parameter distribution $d_0$ for different values of $\eta$ and $\phi$ with 25 bins in each projection. The impact parameter is calculated with respect to the PV with the track being removed from the determination of the PV. The left figure shows the real bias in data, while the right figure shows the simulation of the same effect (nominal MC simulation is flat with zero bias).

Furthermore, a number of **stability tests** of the results are made, including dependence on the number of PV in the event, period of data-taking, chosen trigger, size of $b/c$ invariant mass window, kinematic of the signal particle, etc.

# 5  *CP*-Violating *B*-meson decays

The excess of matter over antimatter observed in our Universe is not explainable within the Standard Model. The process of dynamical generation of matter over antimatter, baryogenesis, is conditioned by the existence of *CP*-violation [185]. SM has mechanisms for CPV, which originate from the complex phase in the Cabibbo-Kobayashi-Maskawa (CKM) matrix [186, 187] describing the charge-changing weak transitions of quarks. The theory distinguishes three types of CPV in the quark sector:

- CPV in decay, when the amplitude $A_f$ of the process $M^0 \to f$ is different from the amplitude $\overline{A}_{\overline{f}}$ of the process involving the anti-initial state and the anti-final state $\overline{M}^0 \to \overline{f}$.

- CPV in mixing, when the composition of mass eigenstates is non-equally contributed by the flavour eigenstates: $|M_{L,H}\rangle = p|M^0\rangle \pm q|\overline{M}^0\rangle$, $|p/q| \neq 1$.

- CPV in interference between decays with and without mixing in the same final state, $M^0 \to \overline{M}^0 \to f$ versus $M^0 \to f$, defined by $\arg(\lambda_f) = \arg((q/p)(\overline{A}_f/A_f)) \neq 0$.

So far, all measurements of CPV (including kaons, *D*-mesons, and *B*-mesons) are very well compatible with the SM predictions (for a comprehensive summary, see Reference [160]). However, the size of the CPV is too small, by several orders of magnitude, to be compatible with the observed matter-antimatter asymmetry [188]. This fact suggests that there should be other than SM sources of CPV. Testing the CPV in various processes is thus a promising way to find New Physics effects.

## 5.1  *CP*-Violation in $B_s^0 \to J/\psi\phi$ Decay at ATLAS

ATLAS has analyzed [**8**–**11**] the so-called golden channel $B_s^0 \to J/\psi\phi$, measuring the *CP*-violating phase $\phi_s$ which describes the CPV in the interference between the direct decay and decay with mixing (see Figure 16). In SM the CPV phase is related
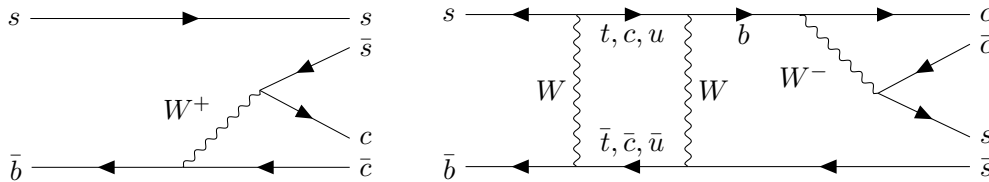


Figure 16: Feynman diagrams of $B_s^0 \to J/\psi\phi$ decay without and with mixing.

to the CKM elements: $\phi_s \simeq -2\beta_s = -2\arg[-(V_{ts}V_{tb}^*)/(V_{cs}V_{cb}^*)]$ and is quite small $(-0.037 \pm 0.001)\,\mathrm{rad}$ [189]. NP processes could contribute to the mixing box diagrams, potentially allowing for a large deviation in $\phi_s$ from SM. The $B_s^0 \to J/\psi\phi$ decay is a decay of the pseudoscalar to two vector particles. Therefore, the final state is an admixture of *CP*-odd (orbital momentum $L = 1$) and *CP*-event ($L = 0, 2$) states. Moreover, an *S*-wave decay $B_s^0 \to J/\psi K^+ K^-$, nonresonant in the kaon-kaon mass, contributes to the observed signal. The decay(s) is described by physics parameters including $\phi_s$, direct CPV parameter $\lambda$, $B_s^0$–$\overline{B}_s^0$ mixing parameters, and finally the amplitudes and phases of the *CP* (and *S*-wave) states. The $\phi_s$ phase can be extracted from the analysis of the time-dependent distribution of the decay angles:

$$\frac{\mathrm{d}^4\Gamma}{\mathrm{d}t\,\mathrm{d}\Omega} = \sum_{k=1}^{10} \mathcal{O}^{(k)}(t)g^{(k)}(\theta_T, \psi_T, \phi_T) \tag{7}$$

where $t$ is the $B_s^0$ meson proper decay time and decay angles $\theta_T$, $\psi_T$, $\phi_T$ are defined in transversity bases as shown in Figures 17.
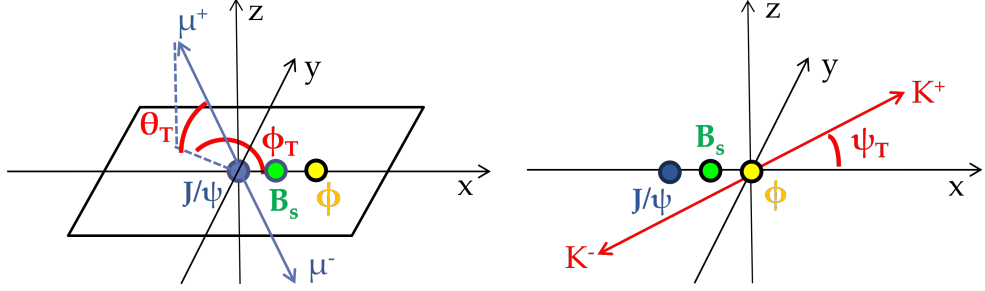


Figure 17: Illustration of the decay angles between the final state particles in transversity basis, with $\theta_T$ and $\phi_T$ defined in the $J/\psi$ rest frame, while $\psi_T$ in the $\phi$ meson rest frame.

The data for the analysis are collected by a set of dimuon triggers. Event selection is cut-based, applying the invariant mass windows of $\phi$, $J/\psi$, momentum cut on the muon and kaon tracks and the quality of the $J/\psi$ and $B_s^0$ vertex. No cut on the $B_s^0$ proper decay time is applied to avoid complicated compensation of the cut efficiency and to keep background data in the analyzed sample to help describe detector resolution. Almost 0.5 million signal candidates are available in the latest datasample.

For the extraction of $\phi_s$ and other physics parameters, an UML fit is used. In addition to the proper decay time and decay angles, the fit uses per-candidate (mass) time resolution, $B_s^0$ meson $p_T$, and $B_s^0$ flavour tagging variables (see below). Besides combinatorial background, dedicated $B^0$ and $\Lambda_b$ backgrounds are included. The multidimensions and large number of free physics and nuisance parameters make the fit challenging (stability, intrinsic biases).

An important part of the analysis is the determination of the initial $B_s^0$ meson flavour (at the time it was born). This knowledge significantly improves the precision of the measurement (see the comparison of the top two Figures 19), because certain terms in Equation 7 change signs based on that variable (and thus effectively disappear in the untagged analysis). Such initial $B_s^0$ meson flavour tagging utilizes the fact that $b$-hadrons are mostly born in pairs of opposite flavours (from $b\bar{b}$ pairs). Determining the flavour of the opposite $b$-hadron (opposite side tagging) in the event thus determines the initial signal $B_s^0$ meson flavour. The tagging method is based on semileptonic $B$-decays, when the charge of the lepton correlates with the flavour of the $b$-quark ($b(\bar{b}) \to l^{-(+)}$). However, the method is diluted by $B$-meson oscillations and $b \to c \to l$ transitions, providing only statistical differentiation of the flavour of the signal $B_s^0$ meson. The key variable of the tagging method is a $p_T$-weighted charge of tracks ($q_i$) in a predefined cone $\Delta R = \sqrt{\Delta\phi^2 + \Delta\eta^2}$ around the candidate for the opposite side lepton:

$$Q_x = \frac{\sum_i^{N \text{ tracks}} q_i \cdot (p_{\text{T}i})^\kappa}{\sum_i^{N \text{ tracks}} (p_{\text{T}i})^\kappa}, \tag{8}$$

with parameters $\kappa$ and $\Delta R$ optimized to obtain the best tagging performance. In the analysis, three taggers were used: muon-, electron-, and $b$-jet-based (the latest relying on hadronic decays, but using a similar approach). The taggers are calibrated with events containing self-tagged $B^\pm \to J/\psi K^\pm$ decays, where the flavour is clear by the signal itself. The calibration allows obtaining, for a given charge $Q_x \in [-1, 1]$, the probability $P(B|Q)$ that the signal in the event was $B$ or $\overline{B}$. An example of such a relationship is shown in Figures 18. The performance of the taggers is characterized by the following variables:
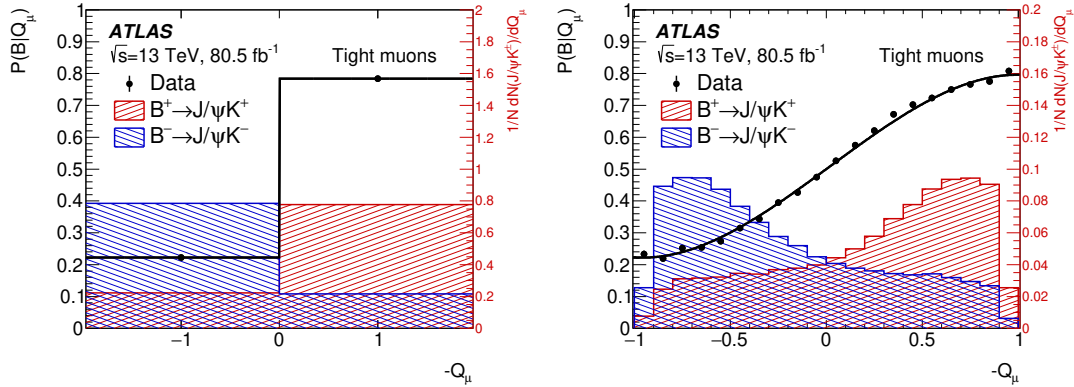
Figure 18: Cone charge distributions, $-Q_\mu$, for muons, shown for the discrete (left) and continuous (right) distribution. In red (blue), the normalized $B^+$ ($B^-$) cone charge distribution is shown (corresponding to the right-axis scale). A $B^+$ ($B^-$) candidate is more likely to have a large negative (positive) value of $Q_\mu$. Superimposed is the distribution of the tagging probability, $P(B|Q_\mu)$, as a function of the cone charge, derived from a data sample of $B^\pm \to J/\psi K^\pm$ decays, and defined as the probability to have a $B^+$ meson (on the signal-side) given a particular cone charge $Q_\mu$. The fitted parameterization, shown in black, is used as the calibration curve to infer the probability to have a $B_s^0$ or $\overline{B}_s^0$ meson at production in the decays to $J/\psi\phi$.

- efficiency $\epsilon_x$, the fraction of events in which the $Q_x$ can be constructed,

- the wrong tag fraction $w_x$ or dilution $D_x = 1 - 2w_x$ that demonstrates how much an ideal asymmetry would be diluted by the wrongly determined flavour,

- combining both above, the tagging power $T_x = \epsilon_x D_x^2$.

In the most recent $B_s^0 \to J/\psi\phi$ ATLAS analysis, 21.2% of events were tagged and the total tagging power reached 1.75%.

Besides the UML fit, the other challenging aspects of these analyses were the tagging optimization and the effect of proper decay time efficiency originating in trigger tracking limitations (muon tracks with large transverse impact parameters rejected). Also, with the enlarging datasets, detector alignment precision becomes important and uneasy-to-evaluate uncertainty of the measurement. However, so far the dominant systematics come from the tagging procedures, accounting for pileup dependence, calibration curves model, tagging PDFs in the UML fit, and for the difference between $B^\pm$ (calibration) and $B_s^0$ (signal) kinematics.

The main results of the series of the $B_s^0 \to J/\psi\phi$ analyses at ATLAS are shown in Figure 19, presenting the measurement of the CPV phase $\phi_s$ and $\Delta\Gamma_s$ (the difference of decay times of the mass eigenstates in $B_s^0$ mixing). The measurement of the CPV phase $\phi_s$ is consistent with the SM prediction. A $3\sigma$ tension with the current world combined value is revealed in the average decay width $\Gamma_s$.
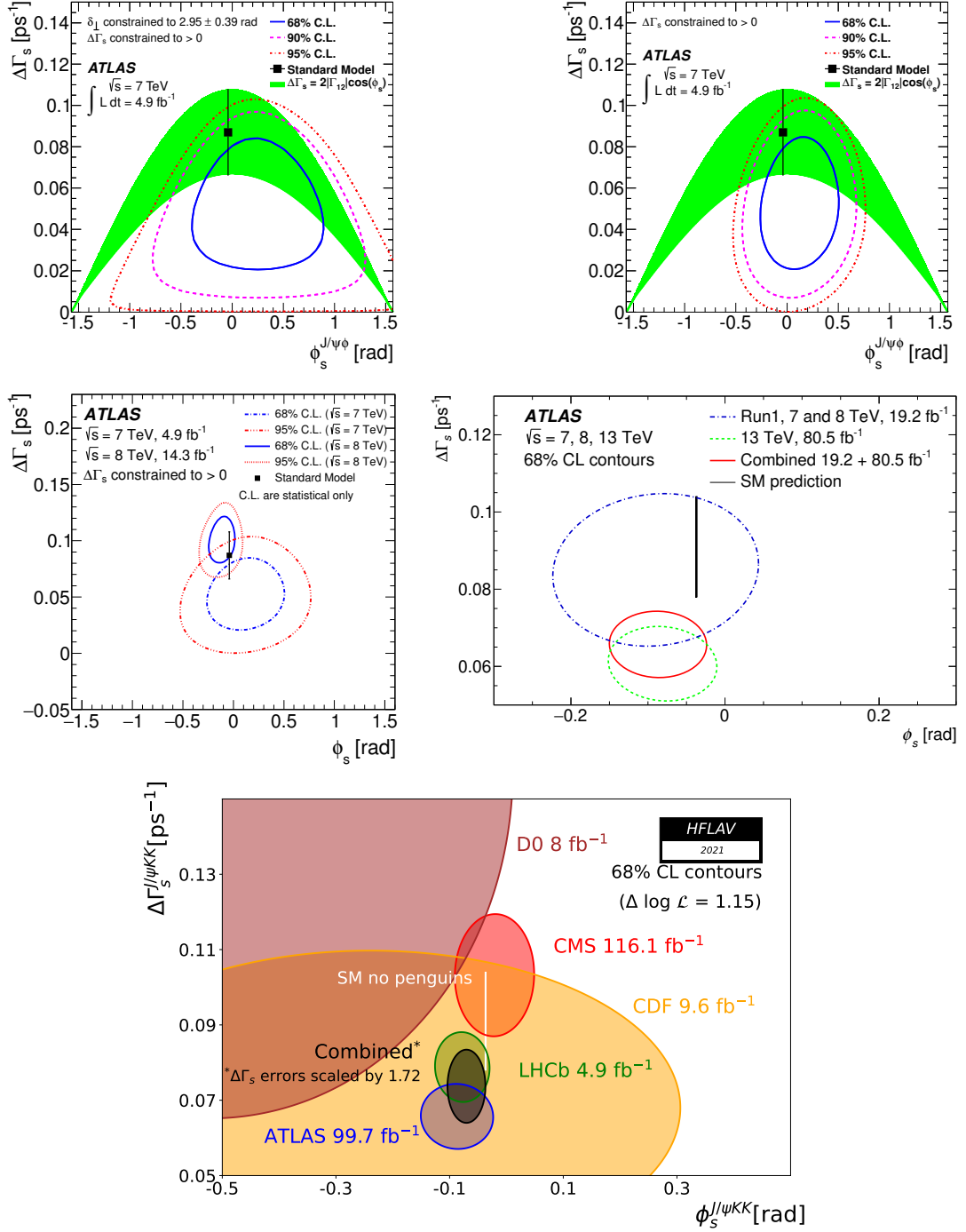
Figure 19: Evolution of the results of the CPV measurement in $B_s^0 \to J/\psi\phi$ channel at ATLAS. Contours of 68% confidence level in the $\phi_s$–$\Delta\Gamma_s$ plane, showing ATLAS results for $pp$ collision data with $\sqrt{s}$ of 7 TeV [11] (top: left not tagged, right with tagging, at the same data, demonstrating the sole effect of tagging on precision of the analysis), 8 TeV [10] (middle right) and 13 TeV [190] (middle left, partial Run 2 data only as the latest public ATLAS result). The plots include also combination of the various datasets. The combination of all tagged Run 1 and Run 2 ATLAS results overlaid with results from the same analysis of other experiments [191–196] is shown on the bottom figure, provided by The Heavy Flavour Averaging Group [71]. The SM prediction for $2\beta_s$ and $\Delta\Gamma_s$ are taken from References [189, 197] and neglects possible sub-leading Penguin contributions.

# 6 Rare *B*-meson decays

The rare *b*-hadron decays do not occur at the tree level of the Feynman diagrams and proceed via diagrams with loops or boxes. Possible new particles in the loops can thus significantly modify the properties of such decay, in particular, the branching fraction and/or angular distribution of the decay products. The rare decays are thus often used as probes for NP. The experimental challenge is in their rareness: Extracting them from the data requires strong suppression of various types of background, leaving a handful of signal events to observe or have available for potential angular analysis. Moreover, quite exotic backgrounds can emerge in the analysis, including other known and yet-unobserved rare decays.

One class of such rare decays are the FCNC transitions, which are especially sensitive to NP due to several suppression mechanisms in the SM:

- proceed via loops, no tree diagrams,
- presence of small CKM elements ($|V_{ts}| = 0.0415 \pm 0.0009$, $|V_{td}| = 0.0086 \pm 0.0002$) [160],
- Glashow–Iliopoulos–Maiani (GIM [198]) suppression mechanism in loops with charm or down-type quarks by a factor of $\sim (m_s^2 - m_d^2)/M_W^2$,
- and helicity suppression in radiative or leptonic decays by a factor of $\sim m_{b,s}/M_W$ due to a helicity flip,

while NP can proceed via tree diagrams or some of the suppressions might be missing. The analyses of rare *B*-meson decays at ATLAS include (among others) purely leptonic decays $B^0_{(s)} \to \mu^+\mu^-$ [67, 120] and semileptonic rare decay $B^0 \to K^{*0}\mu^+\mu^-$ [12]. In the former case, BR is measured, while in the latter case, an angular analysis is performed. Examples of Feynman diagrams representing these decays with NP contributions are depicted in Figures 20.
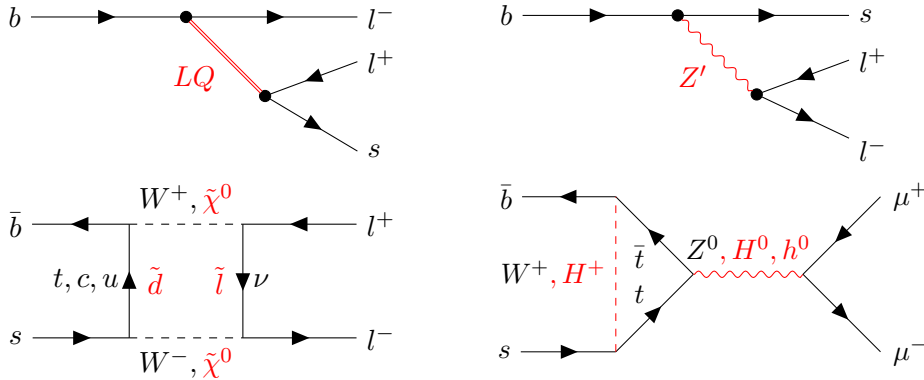


Figure 20: Examples of Feynman diagrams for $B^0 \to K^{*0}\mu^+\mu^-$ (top) and $B^0_s \to \mu^+\mu^-$ (bottom) decays with New Physics contributions (red color).

## 6.1 Semileptonic Rare $B^0 \to K^{*0}\mu^+\mu^-$ Decay Analysis at ATLAS

The semileptonic rare decay $B^0 \to K^{*0}(K^+\pi^-)\mu^+\mu^-$ proceeds in SM at the lowest order via penguin or box Feynman diagrams. The BR is of the order of $10^{-6}$ [160], allowing more detailed studies of the differential decay rate. An anomaly has been observed by LHCb in the distribution of decay angles as a function of the dimuon invariant mass, though there is also interest in measurements of the charge asymmetry, differential branching fraction, or isospin asymmetry. The ATLAS analysis [12] is focused on the

region of the observed anomaly, in the dimuon mass squared ($q^2$) range only up to $6\,\mathrm{GeV}^2$.

The angular differential decay rate as a function of $q^2$ and the helicity angles $\theta_L$, $\theta_K$, and $\phi$ (see Figure 21) is [199, 200]:

$$
\frac{1}{\mathrm{d}\Gamma/\mathrm{d}q^2}\frac{\mathrm{d}^4\Gamma}{\mathrm{d}\cos\theta_L \mathrm{d}\cos\theta_K \mathrm{d}\phi \mathrm{d}q^2} = \frac{9}{32\pi}\left[\frac{3(1-F_L)}{4}\sin^2\theta_K + F_L\cos^2\theta_K + \frac{1-F_L}{4}\sin^2\theta_K\cos 2\theta_L\right.
$$
$$
-F_L\cos^2\theta_K\cos 2\theta_L + S_3\sin^2\theta_K\sin^2\theta_L\cos 2\phi
$$
$$
+S_4\sin 2\theta_K\sin 2\theta_L\cos\phi + S_5\sin 2\theta_K\sin\theta_L\cos\phi
$$
$$
+S_6\sin^2\theta_K\cos\theta_L + S_7\sin 2\theta_K\sin\theta_L\sin\phi
$$
$$
\left.+S_8\sin 2\theta_K\sin 2\theta_L\sin\phi + S_9\sin^2\theta_K\sin^2\theta_L\sin 2\phi\right], \qquad (9)
$$

with $F_L$ being the fraction of longitudinally polarized $K^{*0}$ mesons and $S_i$ being the angular coefficients, all $q^2$ dependent. However, the predictions for $S_i$ depend on hadronic form factors with significant uncertainties at the leading order. Using the following transformations, these uncertainties at leading order cancel [200, 201]:

$$
P_1 = \frac{2S_3}{1-F_L} \qquad P_2 = \frac{1}{2}\frac{S_6}{1-F_L} \qquad P_3 = -\frac{S_9}{1-F_L} \qquad P'_{j=4,5,6,8} = \frac{S_{i=4,5,7,8}}{\sqrt{F_L(1-F_L)}}. \qquad (10)
$$
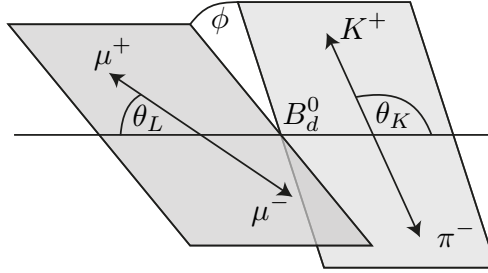


Figure 21: Illustration of the helicity decay angles between the final state particles, with $\theta_L$ defined in the dimuon rest frame, $\theta_K$ in the $K^{*0}$ rest frame, and $\phi$ in the $B^0$ rest frame.

The core of the analysis are extended UML fits in $q^2$ bins, including among the helicity angles also the invariant mass of $B^0$ candidates and its per-candidate uncertainty. Resonant decays $B^0 \to K^{*0}J/\psi$ (see Figure 22 left) and $B^0 \to K^{*0}\psi(2S)$ are used as control channels. Event selection is cut-based, optimized on MC simulations, with a hard minimum cut on the $B^0$ candidate proper decay time and a strong $B^0$ meson momentum pointing constraint towards the PV. As a consequence of missing hadron identification at ATLAS and the wide natural width of the $K^{*0}$ meson, in around 11% of cases the $B^0$ meson flavour is mistagged[17].

In the dataset of $pp$ collisions at $\sqrt{s} = 8\,\mathrm{TeV}$ only $342\pm39$ signal events are extracted, as depicted in Figure 22 (right). A fit of the full angular distribution of Equation 9 with so many free parameters would not converge. Therefore, foldings of the angular distribution were applied, reducing the angular fit parameters to $F_L$, $S_3$, and one of

---

[17]Both $K^{*0}$ or $\overline{K}^{*0}$ candidate hypotheses are tested with the two opposite-charge hadronic tracks, choosing the candidate with invariant mass closer to the $K^{*0}$ nominal mass. But in case of similar momentum of the two hadronic tracks, both hypotheses can provide candidate with invariant mass within the natural width of the $K^{*0}$ meson.
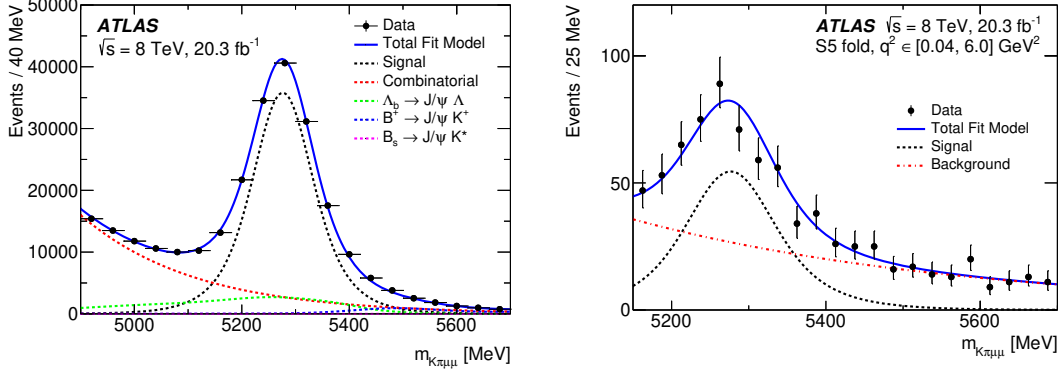
Figure 22: Fits to the $K\pi\mu\mu$ mass distribution for the samples of the control $J/\psi K^{*0}$ region (left) and the signal region of $q^2 \in [0.04, 6.0]\,\mathrm{GeV}^2$ (right). The data are shown as points and the total fit model as the solid lines. The black dashed line represents signal, the other lines combinatorial and dedicated background components.

$S_4$, $S_5$, $S_7$, or $S_8$. An example of the folding procedure to extract the $P_5'$ (resp. $S_5$) parameter uses absolute values of the helicity angles $\phi$ and $\cos\theta_L$ (i.e. transforms $\phi \to -\phi$ for $\phi < 0$ and $\theta_L \to \pi - \theta_L$ for $\theta_L > \pi/2$). The decay angular differential rate then simplifies to:

$$\frac{1}{\mathrm{d}\Gamma/\mathrm{d}q^2}\frac{\mathrm{d}^4\Gamma}{\mathrm{d}\cos\theta_L\,\mathrm{d}\cos\theta_K\,\mathrm{d}\phi\,\mathrm{d}q^2} = \frac{9}{8\pi}\left[\frac{3(1-F_L)}{4}\sin^2\theta_K + F_L\cos^2\theta_K + \frac{1-F_L}{4}\sin^2\theta_K\cos 2\theta_L\right.$$
$$-F_L\cos^2\theta_K\cos 2\theta_L + S_3\sin^2\theta_K\sin^2\theta_L\cos 2\phi$$
$$\left.+S_5\sin 2\theta_K\sin\theta_L\cos\phi\right].$$

However, the foldings lead to a loss of sensitivity to parameters $S_6$ and $S_9$, the former related to the forward-backward asymmetry of muons. Since $S_3$ and $F_L$ are present in each of the four folding schemes, the measurements with the lowest systematic uncertainties were taken. Several other measures have been taken to cope with the low number of signal events: wide $q^2$ bins of $2\,\mathrm{GeV}^2$ are used, sequential mass-angular extended UML fit is applied, fitting the mass distribution independently first, and fixing its related physics and nuisance parameters in the following mass-angular fit. Moreover, part of the parameters related to the mass fit is constrained using the fit results on the control channels.

A challenging aspect of the analysis was also understanding the background processes. Around 30 dedicated background $B$-decays were identified and studied as potential contributors to the collected events, including the $S$-wave $B^0 \to K^+\pi^-\mu^+\mu^-$. Still, two other groups of decays were also discovered, $B \to DX$ and $B^+ \to \mu^+\mu^- h^+$ ($h$ denotes charged pion or kaon), creating structures in the decay angles distribution [96] and resulting in additional systematic uncertainties.

The results of the analysis are summarized in Figures 23, showing the extracted angular parameters in three $q^2$ bins and comparing them with the results of other experiments and theoretical predictions. All measurements are found to be within three standard deviation of the different SM predictions. The results are also compatible with the other measurements. The systematic uncertainties mostly originate in the description of various backgrounds, both dedicated and combinatorial ones.
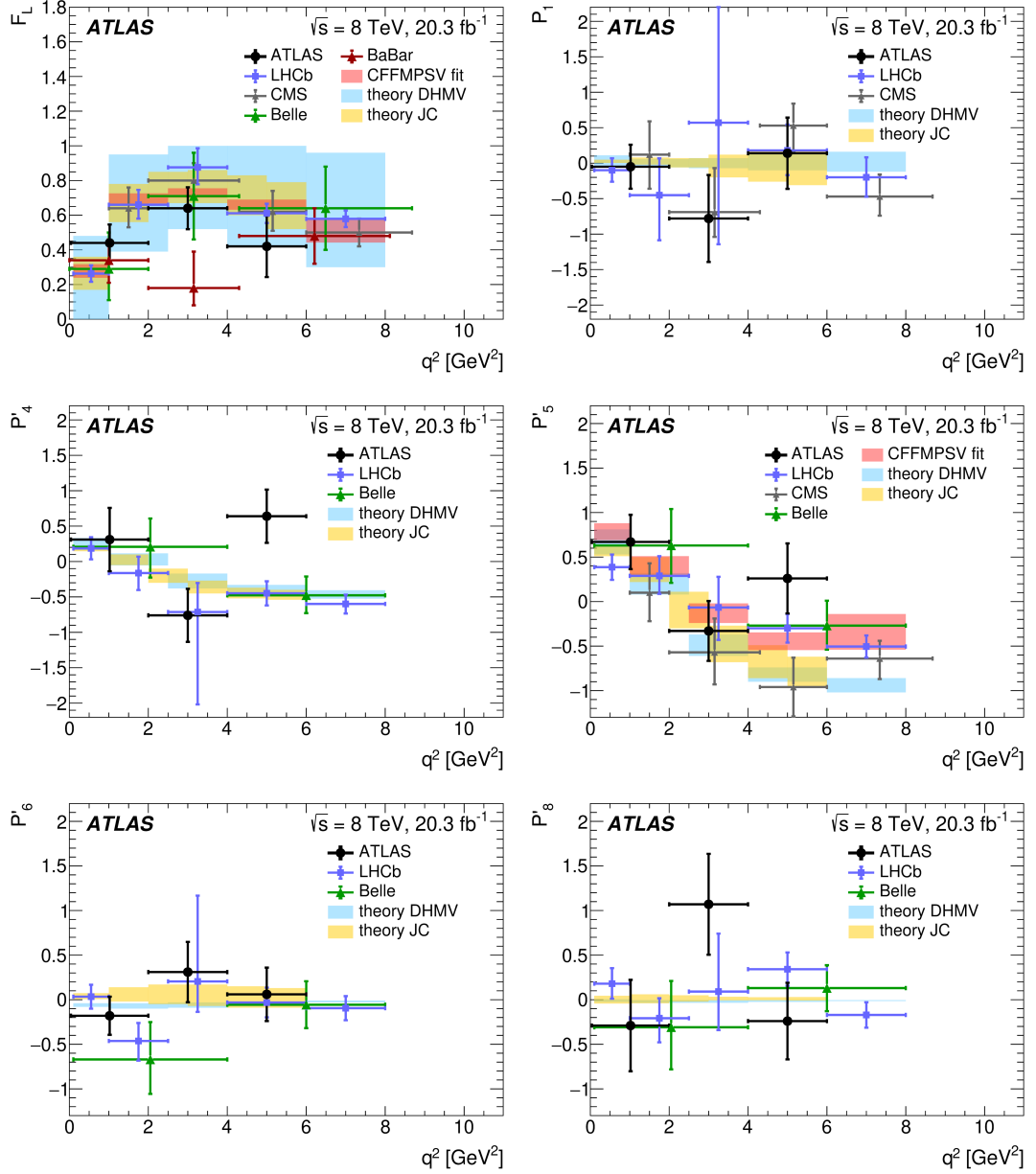
Figure 23: The measured values of angular parameters $F_L$, $P'_1$, $P'_4$, $P'_5$, $P'_6$, $P'_8$ compared with predictions from several theoretical groups (CFFMPSV [202], DHMV [102], JC [203, 204]) and with results from other experiments (at the time of publication): LHCb [205], CMS [206, 207], Belle [208, 209], BaBar [210].

# 7 Exotic Multiquark Structures

The constituent quark model describes mesons and baryons as bound $q\bar{q}$ and $qqq$ states. However, QCD suggests that more complicated states may exist, in particular, bound $q\bar{q}$-pairs with an excited gluon, multiquark singlet states such as $qq\bar{q}\bar{q}$ (tetraquarks either as compact systems or molecular-like bound states of two mesons) or $qqqq\bar{q}$ (pentaquarks again either as compact or bound hadron-meson states)[18]. Evidence for a number of such states has been collected [160], with $X(3872)$ ($u\bar{c}u\bar{c}$ tetraquark-like composition) as the first one observed [211] in 2003 at the Belle experiment. For pentaquarks, several reports appeared at about the same time, but have been shown to be spurious [212]. The first widely accepted evidence for pentaquarks has been reported by LHCb [213], where two $J/\psi p$ resonances have been observed in $\Lambda_b \to J/\psi K^- p$ decays. The ATLAS experiment contributed to these searches as well [13, 51, 214, 215].

## 7.1 Search For a Structure in the $B_s^0 \pi^\pm$ Mass Spectrum at ATLAS

Recently, the D0 collaboration [216] reported an observation of another tetraquark candidate [217]: a narrow structure $X(5568)$ in $B_s^0 \pi^\pm$ system (with $B_s^0 \to J/\psi \phi$). The resonance was supposed to be composed of $b$, $s$, $u$, and $d$ (anti-)quarks. ATLAS was among the experiments that tried to confirm this observation, using $pp$ collision data from Run 1. The analysis [**13**] was targeted to the properties of the final state seen at D0, searching for the signal in $B_s^0 \pi^\pm$ invariant mass in the range starting from the threshold up to $5.8\,\text{GeV}$.

The analysis uses the same selection of $B_s^0 \to J/\psi \phi$ candidates as the CPV analysis described in Section 5, except that additional cut on the proper decay time $t > 0.2\,\text{ps}$ is applied to reduce S/B and the $B_s^0$ invariant mass is limited to the signal region of $(5346.6 - 5386.6)\,\text{MeV}$. Kinematics of the $B_s^0$ meson is constrained to $p_\text{T}(B_s^0) > 10\,\text{GeV}$. Hadronic tracks (charged pion candidates) from the associated primary vertex are then combined with the $B_s^0$ candidates. The invariant mass of the $B_s^0 \pi^\pm$ system is calculated as $m(J/\psi K^+ K^- \pi^\pm) - m(J/\psi K^+ K^-) + m_\text{fit}(B_s^0)$, where $m_\text{fit}(B_s^0) = 5366.6\,\text{MeV}$. This definition significantly improves the resolution of $m(B_s^0 \pi^\pm)$. In average, 1.8 $B_s^0 \pi^\pm$ candidates are seen in an event and are all retained for further analysis. The distribution of $m(B_s^0 \pi^\pm)$ is fitted using an extended maximum likelihood method, as depicted in Figure 24. No signal is observed with properties corresponding to the D0 $X(5568)$ resonance. A series of fits is performed to scan the whole $m(B_s^0 \pi^\pm)$ range for possible excesses, but no signal is found either. Thus, upper limits are determined for the number of $B_s^0 \pi^\pm$ signal events and for the relative production rate of a hypothetical resonance $X$:

$$\rho_X \equiv \frac{\sigma(pp \to X + \text{anything}) \times \mathcal{B}(X \to B_s^0 \pi^\pm)}{\sigma(pp \to B_s^0 + \text{anything})} = \frac{N_X}{N_{B_s^0}} \times \frac{1}{\epsilon^\text{rel}(X)} \quad (11)$$

The limits, which account for the relative reconstruction and selection efficiency $\epsilon^\text{rel}(X)$ determined with MC simulations, are calculated using the asymptotic approximation from the profile likelihood formalism based on the $\text{CL}_s$ frequentist method. The upper limits on $\rho_X$ are shown in Figure 25 and do not support the D0 observation. Similar searches by LHCb [218], CMS [219], and CDF [220] also did not reveal any signal.

---

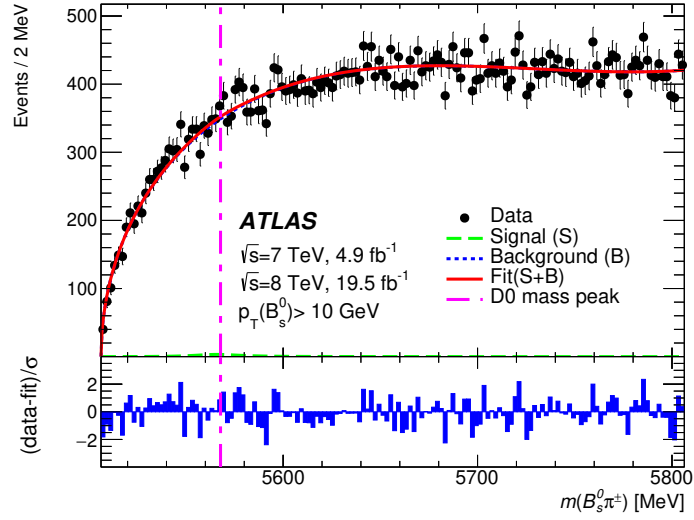[18]Even more complicated states of six quarks ($qqq\bar{q}\bar{q}\bar{q}$) are predicted.

Figure 24: Results of the fit to the $B_s^0 \pi^\pm$ mass distribution. The bottom panel shows the difference between each data point and the fit divided by the statistical uncertainty of that point. No significant signal (green) component is detected at the mass position of the $X(5568)$ structure.
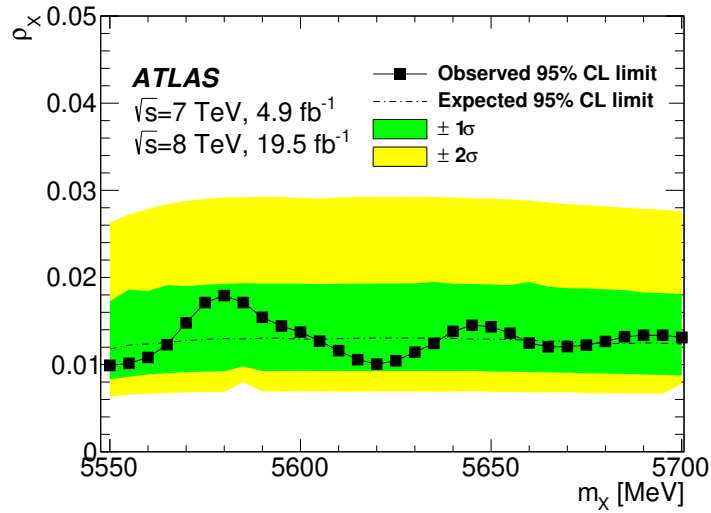


Figure 25: Upper limits for the relative production rate $\rho_X$ at 95% CL (black squares connected by line) at different masses of a hypothetical resonant state $X$ decaying to $B_s^0 \pi^\pm$. A Breit-Wigner width as reported by D0 is assumed. The expected 95% CL upper limits (central black dot-dashed line) with $\pm 1\sigma$ (green) and $\pm 2\sigma$ (yellow) uncertainty bands on $\rho_X$ are shown as a function of the assumed resonance mass. No signal is observed in the scanned mass range.

# 8    Future Prospects

Heavy flavour production and decays will be studied using the future facilities as well, all the more the observed flavour anomalies are currently one of the promising signals of physics beyond SM. Relatively recently (in 2018) Belle II experiment [221, 222], a new generation $e^+e^-$ B-factory at the SuperKEKB collider, has recorded the first data and will overcome its predecessor, Belle experiment [223] at KEKB, by providing $10\times$ larger integrated luminosity (by 2027). In the field of hadron colliders, it is the High-Luminosity LHC with the upgraded ATLAS, CMS, and LHCb detectors, and possibly also the Future Circular Collider (FCC) [224], where HF physics will also take place. The ATLAS B-physics program provided important results from Run 1 and Run 2, and data are currently being taken in Run 3, anticipating $2\times$ larger dataset than collected up to now. Similar HF analyses will run also at the High-Luminosity LHC with the Upgraded ATLAS detector. Within the ATLAS B-physics group, HL-LHC projections of the expected precision of a few fundamental B-physics analyses [14, 15, 225, 226] were performed. Two of them include the channels $B_s^0 \to J/\psi\phi$ [**14**] and $B^0 \to K^{*0}\mu^+\mu^-$ [**15**].

Although an obvious improvement at HL-LHC comes from the increased luminosity and $b$-hadron production cross section, thus larger number of $b$-hadrons produced in the $pp$ collisions, other improvements are related to the upgrade of the detector subsystems, as described in Section 3. On the other hand, an increased number of $pp$ collisions in single bunch crossing will put stress on the trigger system, resulting in a need to tighten the trigger selection criteria.

## 8.1    ATLAS Upgrade Performance

The replacement of the tracking system with the all-silicon ITk detector would significantly improve the precision of measurement of the momenta of the charged particles as well as the impact parameter. This will thus result in better resolution of the $b$-hadron invariant mass and the decay time. The improvements are illustrated in Figures 26 and 27. The invariant mass resolution shrinks by 30%, while the proper decay time resolution shrinks by 21%, compared to the Run 2 ATLAS detector with already installed IBL. Also, it is observed that the proper decay time resolution does not deteriorate with the increasing pileup. These studies, evaluating the improvements in the reconstruction of basic physics quantities, were one of many that contributed to the decision about the design of the ITk geometry (position and inclination of the detector layers, pixel size).

## 8.2    Projections of $B^0 \to K^{*0}\mu^+\mu^-$ and $B_s^0 \to J/\psi\phi$ Analyses

The projections of the B-physics analyses account for the effects of the improved detector, for the increased integrated luminosity, $b$-hadron production cross section, and pileup, and evaluate the expected precision of the measurements under three trigger scenarios (optimistic, middle, and conservative). The optimistic one, requiring muon $p_{\mathrm{T}}$ thresholds at $6\,\mathrm{GeV}$, is close to the conditions in Run 2 and Run 3. The choice of the scenarios is based on considerations discussed in the ATLAS Phase II TDAQ Technical Design Report [23]. As the trigger system for HL-LHC does not yet exist, the trigger algorithms are emulated by offline selections.

In both analyses, toy-MC is used to evaluate the expected precision of the physics parameters of interest. The starting point for the evaluation is the results from Run 1. Monte Carlo simulations and real data are used to estimate the number of signal and background events. On the basis of those numbers, toy-MC data are produced. The analysis procedures then exactly follow the real analyses from the existing ATLAS
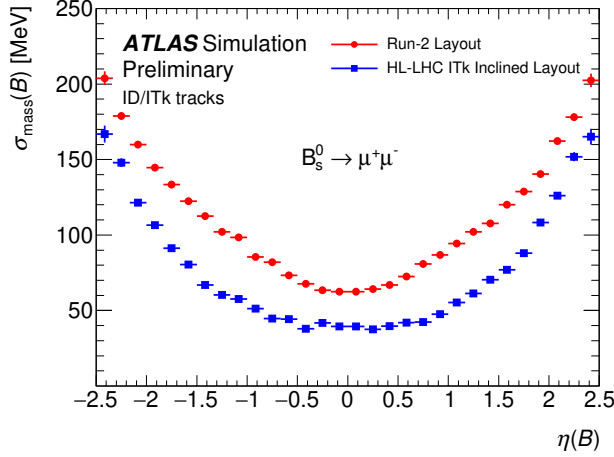
Figure 26: $B_s^0$ mass resolution $\sigma_{\mathrm{mass}}(B)$ as a function of the $B_s^0$ meson pseudo-rapidity in the decay channel $B_s^0 \to \mu^+\mu^-$, comparing the performance from MC simulations for Run 2 and HL-LHC. Taken from Reference [16].
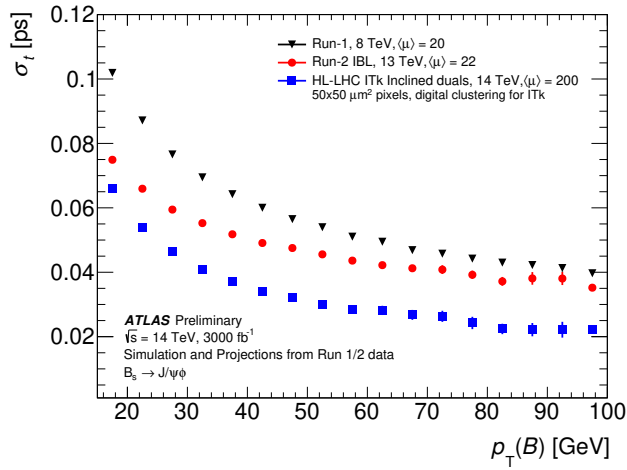


Figure 27: Dependence of the $B_s^0$ meson proper decay time resolution of the signal $B_s^0 \to J/\psi\phi$ decay on $B_s^0$ $p_T$. Per-candidate resolutions corrected for scale factors are shown, comparing the performance in Run 1 (ID), Run 2 (IBL) and upgrade HL-LHC MC simulations. Taken from Reference [14].

measurements. Systematic uncertainties are divided into several groups: those dependent on real data (e.g. fit-model systematics) are assumed to reduce as with the square root of the relative integrated luminosities, while the ones depending purely on the amount of MC simulations are neglected. Systematics depending on external measurements are treated case by case (either unchanged or, when backed up by new facts since the Run 1 analyses, reduced).

The results indicate that we can expect an improvement in the precision of the physics parameters of interest by $9\times$–$20\times$ ($B_s^0 \to J/\psi\phi$), respectively $5\times$–$9\times$ ($B^0 \to K^{*0}\mu^+\mu^-$), as illustrated in Figures 28 and 29. Hence ATLAS Upgrade is expected to observe nonzero $\phi_s$ and confirm (or reject) the $P_5'$ anomaly.
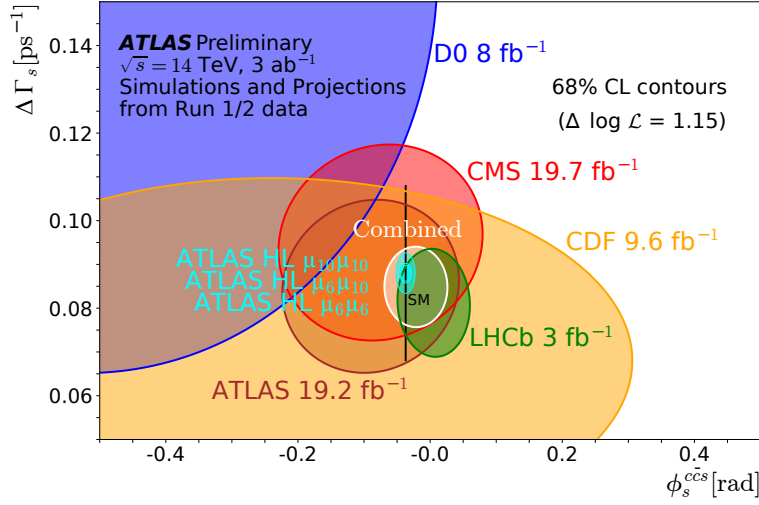
Figure 28: Experimental summary of the $\phi_s$ measurements with superimposed ATLAS HL-LHC extrapolations, including both the projected statistical and systematic uncertainties. Modified figure [14], original taken from [227, 228].
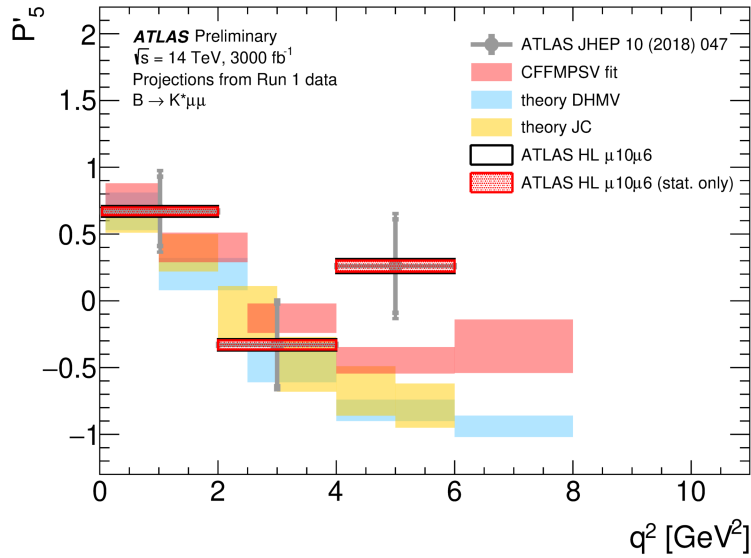


Figure 29: Projected ATLAS HL-LHC measurement precision [15] in the $P'_5$ parameter for the intermediate trigger scenario compared to the ATLAS Run 1 measurement. Alongside theory predictions (CFFMPSV [202], DHMV [102], JC [203]) are also shown. Both the projected statistical and the total (statistical and systematic) uncertainties are shown. While the HL-LHC toy-MC were generated with the DHMV central values of the $F_L$ and $P_i^{(\prime)}$ parameters, in these plots the central values are moved to the ATLAS Run 1 measurement for better visualization of the improvement in the precision.

# 9  Conclusions

Testing the heavy flavour sector of the Standard Model is a promising tool in the search for New Physics. The thesis summarizes the main analyses of the B-physics group at the ATLAS experiment, to which I have contributed significantly. This includes analyses of $CP$-violation in $B_s^0 \to J/\psi\phi$ decay, a search for exotic structures connected with heavy flavour, as well as a probe of the properties of semileptonic rare $B$-meson decays. The first topic attempts to find an answer to the question of the superiority of matter over antimatter in the Universe. The search for and studies of exotic structures allows for the tests of the Quantum Chromodynamics. The last topic of rare decays is connected with the so-called Flavour Anomalies, a set of signs of tension between Standard Model predictions and the experimental results. Although the most pronounced measurements of the anomalies come from specialized experiments on heavy flavour physics, the B-factories, experiments at general purpose detectors such as ATLAS or CMS also contribute to some of these observations of tensions. At the same time, especially accounting for that many of the anomalies are/were only seen on a single (LHCb) experiment, independent measurements from other experiments such as ATLAS provide a valuable cross-check. The importance of the cross-checks is enhanced by the recent disappearance of several of the flavour anomalies.

The ATLAS heavy flavour analyses are, so far, compatible with the SM predictions, with a few deviations slightly below the $3\sigma$ level. With the upcoming datasets from Run 3 or High-Luminosity LHC, the increased number of events would eventually allow determining whether those signs of deviations indicated real discrepancy from SM, or whether they were just statistical fluctuations. Accounting also for prospects of other future experiments at LHC and $e^+e^-$ B-factories, B-physics will remain an exciting field of research.

# References

[1]  ATLAS Collaboration, *Observation of a new particle in the search for the Standard Model Higgs boson with the ATLAS detector at the LHC*, Phys. Lett. B **716** (2012) pp. 1–29, arXiv: 1207.7214 [hep-ex] (cit. on p. 2).

[2]  CMS Collaboration, *Observation of a New Boson at a Mass of 125 GeV with the CMS Experiment at the LHC*, Phys. Lett. B **716** (2012) pp. 30–61, arXiv: 1207.7235 [hep-ex] (cit. on p. 2).

[3]  *LHC Machine*, JINST **3** (2008) S08001, ed. by L. Evans and P. Bryant (cit. on p. 2).

[4]  ATLAS Collaboration, *The ATLAS Experiment at the CERN Large Hadron Collider*, JINST **3** (2008) S08003 (cit. on pp. 2, 10–12).

[5]  ATLAS Collaboration, *ATLAS Experiment - Public Results*, https://twiki.cern.ch/twiki/bin/view/AtlasPublic, 2022-10-15 (cit. on p. 2).

[6]  LHCb Collaboration, *The LHCb Detector at the LHC*, JINST **3** (2008) S08005 (cit. on p. 2).

[7]  LHCb Collaboration, *LHCb Detector Performance*, Int. J. Mod. Phys. A **30** (2015) p. 1530022, arXiv: 1412.6352 [hep-ex] (cit. on p. 2).

[8]  G. Aad, ..., P. Řezníček, ... et al. (ATLAS Collaboration), *Measurement of the $CP$-violating phase $\phi_s$ in $B_s^0 \to J/\psi\phi$ decays in ATLAS at 13 TeV*, Eur. Phys. J. C **81** (2021) p. 342, arXiv: 2001.07115 [hep-ex] (cit. on pp. 3, 30, 56).

[9]  G. Aad, ..., P. Řezníček, ... et al. (ATLAS Collaboration), *Measurement of the CP-violating phase $\phi_s$ and the $B_s^0$ meson decay width difference with $B_s^0 \to J/\psi\phi$ decays in ATLAS*, JHEP **08** (2016) p. 147, arXiv: 1601.03297 [hep-ex] (cit. on pp. 3, 13, 22, 28, 30, 56).

[10]  G. Aad, ..., P. Řezníček, ... et al. (ATLAS Collaboration), *Flavor tagged time-dependent angular analysis of the $B_s^0 \to J/\psi\phi$ decay and extraction of $\Delta\Gamma_s$ and the weak phase $\phi_s$ in ATLAS*, Phys. Rev. D **90** (2014) p. 052007, arXiv: 1407.1796 [hep-ex] (cit. on pp. 3, 30, 33, 56).

[11]  G. Aad, ..., P. Řezníček, ... et al. (ATLAS Collaboration), *Time-dependent angular analysis of the decay $B_s^0 \to J/\psi\phi$ and extraction of $\Delta\Gamma_s$ and the CP-violating weak phase $\phi_s$ by ATLAS*, JHEP **12** (2012) p. 072, arXiv: 1208.0572 [hep-ex] (cit. on pp. 3, 30, 33, 56).

[12]  M. Aaboud, ..., P. Řezníček, ... et al. (ATLAS Collaboration), *Angular analysis of $B_d^0 \to K^*\mu^+\mu^-$ decays in pp collisions at $\sqrt{s}$ = 8 TeV with the ATLAS detector*, JHEP **10** (2018) p. 047, arXiv: 1805.04000 [hep-ex] (cit. on pp. 3, 23, 34, 56).

[13]  M. Aaboud, ..., P. Řezníček, ... et al. (ATLAS Collaboration), *Search for a Structure in the $B_s^0 \pi^{\pm}$ Invariant Mass Spectrum with the ATLAS Experiment*, Phys. Rev. Lett. **120** (2018) p. 202007, arXiv: 1802.01840 [hep-ex] (cit. on pp. 3, 38, 56).

[14]  G. Aad, ..., P. Řezníček, ... et al. (ATLAS Collaboration), *CP-violation measurement prospects in the $B_s^0 \to J/\psi\phi$ channel with the upgraded ATLAS detector at the HL-LHC*, ATL-PHYS-PUB-2018-041, 2018, URL: https://cds.cern.ch/record/2649881 (cit. on pp. 3, 13, 40–42, 56).

[15]  G. Aad, ..., P. Řezníček, ... et al. (ATLAS Collaboration), *$B_d^0 \to K^{*0}\mu\mu$ angular analysis prospects with the upgraded ATLAS detector at the HL-LHC*, ATL-PHYS-PUB-2019-003, 2019, URL: https://cds.cern.ch/record/2654519 (cit. on pp. 3, 40, 42, 56).

[16]  ATLAS Collaboration, *Expected performance for an upgraded ATLAS detector at High-Luminosity LHC*, ATLAS-PHYS-PUB-2016-026, additional plots at https://atlas.web.cern.ch/Atlas/GROUPS/PHYSICS/PLOTS/BPHYS-2016-001/, 2016, URL: http://cds.cern.ch/record/2223839 (cit. on pp. 3, 41).

[17]  ATLAS Collaboration, *ATLAS B-physics studies at increased LHC luminosity, potential for CP-violation measurement in the $B_s^0 \to J/\psi\phi$ decay*, ATLAS-PHYS-PUB-2013-010, 2013, URL: http://cds.cern.ch/record/1604429 (cit. on p. 3).

[18]  N. Kanaya, A. Krasznahorkay, H. Kurashige, C. Omachi, P. Řezníček, *Performance study of the level-1 di-muon trigger*, ATL-PHYS-PUB-2009-045, 2009, URL: http://cds.cern.ch/record/1167941 (cit. on pp. 3, 57).

[19]  N. C. Benekos et al., *B-physics performance with Initial and Complete Inner detector layouts in Data Challenge-1*, ATL-PHYS-2005-002, 2004, URL: http://cds.cern.ch/record/806544 (cit. on p. 3).

[20] ATLAS and CMS Collaborations,
*Snowmass White Paper Contribution: Physics with the Phase-2 ATLAS and CMS Detectors*,
ATL-PHYS-PUB-2022-018, 2022, URL: https://cds.cern.ch/record/2805993 (cit. on p. 3).

[21] A. Dainese et al., *Report on the Physics at the HL-LHC,and Perspectives for the HE-LHC*,
CERN Yellow Rep. Monogr. **7** (2019) pp. 1–1418 (cit. on pp. 3, 56).

[22] A. Cerri et al., *Opportunities in Flavour Physics at the HL-LHC and HE-LHC*,
(2018), CERN-LPCC-2018-06, arXiv: 1812.07638 [hep-ph] (cit. on p. 3).

[23] ATLAS Collaboration,
*Technical Design Report for the Phase-II Upgrade of the ATLAS TDAQ System*,
ATLAS-TDR-029, CERN-LHCC-2017-020, 2017, URL: http://cds.cern.ch/record/2285584
(cit. on pp. 3, 40, 56).

[24] ATLAS Collaboration, *Technical Design Report for the ATLAS Inner Tracker Pixel Detector*,
ATLAS-TDR-030, CERN-LHCC-2017-021, 2017, URL: http://cds.cern.ch/record/2285585
(cit. on pp. 3, 56).

[25] ATLAS Collaboration,
*Expected Performance of the ATLAS Experiment - Detector, Trigger and Physics*, (2009),
arXiv: 0901.0512 [hep-ex] (cit. on p. 3).

[26] G. Aad, ..., P. Řezníček, ... et al. (ATLAS Collaboration),
$B^{\pm}$ *mass reconstruction in* $B^{\pm} \to J/\psi K^{\pm}$ *decay at ATLAS at 13 TeV pp collisions at the LHC*,
ATLAS-CONF-2015-064, 2015, URL: http://cds.cern.ch/record/2114830 (cit. on pp. 3, 57).

[27] G. Aad, ..., P. Řezníček, ... et al. (ATLAS Collaboration), *Measurement of the* $B_d^0$ *and* $B_s^0$
*lifetimes in the decay modes* $B_d^0 \to J/\psi K^{0*}$ *and* $B_s^0 \to J/\psi\phi$ *in ATLAS*,
ATLAS-CONF-2011-092, 2011, URL: http://cds.cern.ch/record/1363779 (cit. on pp. 3, 57).

[28] G. Aad, ..., P. Řezníček, ... et al. (ATLAS Collaboration),
*Observation of the* $B_d^0$ *and* $B_s^0$ *mesons in the decays* $B_d^0 \to J/\psi K^{0*}$ *and* $B_s^0 \to J/\psi\phi$ *in ATLAS*,
ATLAS-CONF-2011-050, 2011, URL: http://cds.cern.ch/record/1341815 (cit. on pp. 3, 57).

[29] G. Aad, ..., P. Řezníček, ... et al. (ATLAS Collaboration),
*Study of alignment-related systematic effects on the ATLAS Inner Detector tracking*,
ATLAS-CONF-2012-141, 2012, URL: http://cds.cern.ch/record/1483518
(cit. on pp. 3, 29, 57).

[30] S. Gadomski and P. Reznicek,
*Measurement of amplifier pulse shapes in SCT modules using a laser setup*,
ATL-INDET-2001-010, 2001, URL: https://cds.cern.ch/record/684249 (cit. on p. 4).

[31] Z. Doležal, Z. Drásal, P. Kodyš, P. Kvasnička, P. Řezníček, D. Scheirich,
*Systematic effects in some semiconductor detector tests*, Nucl. Instrum. Meth. A **583** (2007)
pp. 37–41, Radiation effects on semiconductor materials, detectors and devices. Proceedings,
6th International Conference, RESMDD'06, Florence, Italy, October 10-13, 2006 (cit. on p. 4).

[32] Z. Doležal, C. Escobar, S. Gadomski, C. Garcia, S. Gonzales, P. Kodyš, P. Kubík, C. Lacasta,
S. Marti, V.A. Mitsou, G.F. Moorhead, P.W. Phillips, P. Řezníček, R. Slavík,
*Laser tests of silicon detectors*,
Nucl. Instrum. Meth. A **573** (2007) pp. 12–15, Position-sensitive detectors. Proceedings, 7th
International Conference, PSD-7, Liverpool, UK, September 9-13, 2005 (cit. on p. 4).

[33] ATLAS SCT Collaboration, *ATLAS SCT end-cap module production*,
ATL-INDET-PUB-2006-007, 2006, URL: http://cds.cern.ch/record/973395 (cit. on p. 4).

[34] A. J. Barr et al., *Beamtests of prototype ATLAS SCT modules at CERN H8 in 2000*, (2001)
pp. 104–108, ATL-INDET-2002-005, https://cds.cern.ch/record/684272, 7th Workshop on
electronics for LHC experiments, Stockholm, Sweden, 10-14 Sep 2001: Proceedings
(cit. on p. 4).

[35] N. Nikitin, P. Řezníček, S. Sivoklokov, M. Smižanská, K. Toms,
*Potential of rare B-decays in ATLAS*, Nucl. Phys. B Proc. Suppl. **163** (2007) pp. 147–152,
Proceedings, 1st Workshop on Theory, Phenomenology and Experiment in Heavy Flavour
Physics: Anacapri, Capri, Italy, May 29-31, 2006 (cit. on p. 4).

[36] N. Nikitin, S. Sivoklokov, L. Smirnova, K. Toms, F. Malek, S. Viret, P. Řezníček, M. Smižanská,
*Rare B-decays at ATLAS*,
Nucl. Phys. B Proc. Suppl. **156** (2006) pp. 119–123, Proceedings, 10th International Conference
on B-Physics at Hadron Machines (Beauty 2005): Assisi (Perugia), Italy, 20-24 June 2005
(cit. on p. 4).

[37] P. Řezníček, C. Anastopoulos, E. B-Thacker, J. Catmore, S. Dallison, F. Derue, B. Epp, P. Jussel, A. Kaczmarska, L. d. Mora, H. v. Radzievwski, T. Stahl for the ATLAS Collaboration, *Physics analysis tools for beauty physics in ATLAS*, J. Phys. Conf. Ser. **119** (2008) p. 032003, Proceedings, 16th International Conference on Computing in High Energy and Nuclear Physics (CHEP 2007): Victoria, Canada, September 2-7, 2007 (cit. on pp. 4, 57).

[38] P. Řezníček for the ATLAS Collaboration, *Recent ATLAS results in charmonium production*, PoS **BEAUTY2018** (2018) p. 015, Proceedings, 17th International Conference on B-Physics at Frontier Machines (Beauty 2018): La Biodola, Elba island, Italy, May 6-11, 2018 (cit. on p. 4).

[39] A. Crivellin et al., *PSI/UZH Workshop Proceedings: Impact of $B \to \mu^+\mu^-$ on New Physics Searches*, (2018), arXiv: 1803.10097 [hep-ph] (cit. on p. 4).

[40] P. Řezníček for the ATLAS Collaboration, *Latest ATLAS results on $\phi_s$*, PoS **CKM2016** (2017) p. 083, Proceedings, 9th International Workshop on the CKM Unitarity Triangle (CKM2016): Mumbai, India, November 28-December 3, 2016 (cit. on p. 4).

[41] P. Řezníček for the ATLAS and CMS Collaborations, *Lepton Flavour Violation and $B_{(s)}$ Leptonic Final States at the LHC*, (2009), Proceedings, Heavy Quarks and Leptons 2008 (HQ&L08) Melbourne, Australia, June 5-9, 2008, arXiv: 0905.1613 [hep-ex] (cit. on p. 4).

[42] M. Artuso et al., *B, D and K decays*, Eur. Phys. J. C **57** (2008) pp. 309–492, Flavor in the era of the LHC. Proceedings, CERN Workshop, Geneva, Switzerland, November 2005-March 2007, arXiv: 0801.1833 [hep-ph] (cit. on p. 4).

[43] P. Řezníček for the ATLAS, LHCb and CMS Collaborations, *LHC program for very rare B decays*, Nucl. Phys. B Proc. Suppl. **167** (2007) pp. 188–191, Proceedings, 7th International Conference on Hyperons, Charm and Beauty Hadrons (BEACH 2006): Lancaster, UK, 2-8 July 2006 (cit. on p. 4).

[44] ATLAS Collaboration, *Study of the $B_c^+ \to J/\psi D_s^+$ and $B_c^+ \to J/\psi D_s^{*+}$ decays with the ATLAS detector*, Eur. Phys. J. C **76** (2016) p. 4, arXiv: 1507.07099 [hep-ex] (cit. on p. 4).

[45] ATLAS Collaboration, *Measurement of the parity-violating asymmetry parameter $\alpha_b$ and the helicity amplitudes for the decay $\Lambda_b^0 \to J/\psi \Lambda^0$ with the ATLAS detector*, Phys. Rev. D **89** (2014) p. 092009, arXiv: 1404.1071 [hep-ex] (cit. on p. 4).

[46] ATLAS Collaboration, *Measurement of the production cross section of prompt $J/\psi$ mesons in association with a $W^\pm$ boson in pp collisions at $\sqrt{s} = 7$ TeV with the ATLAS detector*, JHEP **04** (2014) p. 172, arXiv: 1401.2831 [hep-ex] (cit. on p. 4).

[47] ATLAS Collaboration, *Flavor tagged time-dependent angular analysis of the $B_s^0 \to J/\psi\phi$ decay and extraction of $\Delta\Gamma_s$ and the weak phase $\phi_s$ in ATLAS*, Phys. Rev. D **90** (2014) p. 052007, arXiv: 1407.1796 [hep-ex] (cit. on p. 4).

[48] ATLAS Collaboration, *Determination of the ratio of b-quark fragmentation fractions $f_s/f_d$ in pp collisions at $\sqrt{s} = 7$ TeV with the ATLAS detector*, Phys. Rev. Lett. **115** (2015) p. 262001, arXiv: 1507.08925 [hep-ex] (cit. on p. 4).

[49] ATLAS Collaboration, *Measurement of the branching ratio $\Gamma(\Lambda_b^0 \to \psi(2S)\Lambda^0)/\Gamma(\Lambda_b^0 \to J/\psi\Lambda^0)$ with the ATLAS detector*, Phys. Lett. B **751** (2015) pp. 63–80, arXiv: 1507.08202 [hep-ex] (cit. on p. 4).

[50] ATLAS Collaboration, *Observation and measurements of the production of prompt and non-prompt $J/\psi$ mesons in association with a Z boson in pp collisions at $\sqrt{s} = 8$ TeV with the ATLAS detector*, Eur. Phys. J. C **75** (2015) p. 229, arXiv: 1412.6428 [hep-ex] (cit. on p. 4).

[51] ATLAS Collaboration, *Search for the $X_b$ and other hidden-beauty states in the $\pi^+\pi^-\Upsilon(1S)$ channel at ATLAS*, Phys. Lett. B **740** (2015) pp. 199–217, arXiv: 1410.4409 [hep-ex] (cit. on pp. 4, 38).

[52] ATLAS Collaboration, *Measurement of the differential non-prompt $J/\psi$ production fraction in $\sqrt{s} = 13$ TeV pp collisions at the ATLAS experiment*, ATLAS-CONF-2015-030, 2015, URL: https://cds.cern.ch/record/2037967 (cit. on p. 4).

[53] ATLAS Collaboration, *Measurement of the production cross-section of $\psi(2S) \to J/\psi(\to \mu^+\mu^-)\pi^+\pi^-$ in pp collisions at $\sqrt{s} = 7$ TeV at ATLAS*, JHEP **09** (2014) p. 079, arXiv: 1407.5532 [hep-ex] (cit. on p. 4).

[54] ATLAS Collaboration, *Observation of an Excited $B_c^{\pm}$ Meson State with the ATLAS Detector*, Phys. Rev. Lett. **113** (2014) p. 212004, arXiv: 1407.1032 [hep-ex] (cit. on p. 4).

[55] ATLAS Collaboration, *Measurement of $\chi_{c1}$ and $\chi_{c2}$ production with $\sqrt{s} = 7$ TeV pp collisions at ATLAS*, JHEP **07** (2014) p. 154, arXiv: 1404.7035 [hep-ex] (cit. on p. 4).

[56] SNO Collaboration, *Measurement of the rate of $\nu_e + d \to p + p + e^-$ interactions produced by $^8B$ solar neutrinos at the Sudbury Neutrino Observatory*, Phys. Rev. Lett. **87** (2001) p. 071301, arXiv: nucl-ex/0106015 (cit. on p. 5).

[57] Muon g-2 Collaboration, *Measurement of the negative muon anomalous magnetic moment to 0.7 ppm*, Phys. Rev. Lett. **92** (2004) p. 161802, arXiv: hep-ex/0401008 (cit. on p. 5).

[58] Muon g-2 Collaboration, *Measurement of the Positive Muon Anomalous Magnetic Moment to 0.46 ppm*, Phys. Rev. Lett. **126** (2021) p. 141801, arXiv: 2104.03281 [hep-ex] (cit. on p. 5).

[59] CDF Collaboration, *High-precision measurement of the W boson mass with the CDF II detector*, Science **376** (2022) pp. 170–176 (cit. on p. 5).

[60] J. Albrecht, D. van Dyk, and C. Langenbruch, *Flavour anomalies in heavy quark decays*, Prog. Part. Nucl. Phys. **120** (2021) p. 103885, arXiv: 2107.04822 [hep-ex] (cit. on pp. 5, 6, 8).

[61] LHCb Collaboration, *Measurement of CP-Averaged Observables in the $B^0 \to K^{*0}\mu^+\mu^-$ Decay*, Phys. Rev. Lett. **125** (2020) p. 011802, arXiv: 2003.04831 [hep-ex] (cit. on pp. 5, 7).

[62] LHCb Collaboration, *Angular analysis and differential branching fraction of the decay $B_s^0 \to \phi\mu^+\mu^-$*, JHEP **09** (2015) p. 179, arXiv: 1506.08777 [hep-ex] (cit. on pp. 5, 7).

[63] LHCb Collaboration, *Branching Fraction Measurements of the Rare $B_s^0 \to \phi\mu^+\mu^-$ and $B_s^0 \to f_2'(1525)\mu^+\mu^-$ - Decays*, Phys. Rev. Lett. **127** (2021) p. 151801, arXiv: 2105.14007 [hep-ex] (cit. on pp. 5, 7).

[64] LHCb Collaboration, *Differential branching fraction and angular analysis of the decay $B^0 \to K^{*0}\mu^+\mu^-$*, JHEP **08** (2013) p. 131, arXiv: 1304.6325 [hep-ex] (cit. on p. 5).

[65] LHCb Collaboration, *Differential branching fractions and isospin asymmetries of $B \to K^{(*)}\mu^+\mu^-$ decays*, JHEP **06** (2014) p. 133, arXiv: 1403.8044 [hep-ex] (cit. on p. 5).

[66] LHCb Collaboration, *First observations of the rare decays $B^+ \to K^+\pi^+\pi^-\mu^+\mu^-$ and $B^+ \to \phi K^+\mu^+\mu^-$*, JHEP **10** (2014) p. 064, arXiv: 1408.1137 [hep-ex] (cit. on p. 5).

[67] ATLAS Collaboration, *Study of the rare decays of $B_s^0$ and $B^0$ mesons into muon pairs using data collected during 2015 and 2016 with the ATLAS detector*, JHEP **04** (2019) p. 098, arXiv: 1812.03017 [hep-ex] (cit. on pp. 5, 34).

[68] CMS Collaboration, *Measurement of properties of $B_s^0 \to \mu^+\mu^-$ decays and search for $B^0 \to \mu^+\mu^-$ with the CMS experiment*, JHEP **04** (2020) p. 188, arXiv: 1910.12127 [hep-ex] (cit. on p. 5).

[69] LHCb Collaboration, *Measurement of the $B_s^0 \to \mu^+\mu^-$ branching fraction and effective lifetime and search for $B^0 \to \mu^+\mu^-$ decays*, Phys. Rev. Lett. **118** (2017) p. 191801, arXiv: 1703.05747 [hep-ex] (cit. on p. 5).

[70] CMS Collaboration, *Measurement of $B_s^0 \to \mu^+\mu^-$ decay properties and search for the $B^0 \to \mu\mu$ decay in proton-proton collisions at $\sqrt{s} = 13$ TeV*, CMS-PAS-BPH-21-006, 2022, arXiv: 2212.10311 [hep-ex], URL: https://cds.cern.ch/record/2815334 (cit. on pp. 5, 8).

[71] Heavy Flavor Averaging Group, *Averages of b-hadron, c-hadron, and $\tau$-lepton properties as of 2021*, (2022), and online updates till Oct 2022 at https://hflav.web.cern.ch/, arXiv: 2206.07501 [hep-ex] (cit. on pp. 5, 7, 33).

[72] M. Bordone, N. Gubernari, D. van Dyk, and M. Jung, *Heavy-Quark expansion for $\bar{B}_s \to D_s^{(*)}$ form factors and unitarity bounds beyond the $SU(3)_F$ limit*, Eur. Phys. J. C **80** (2020) p. 347, arXiv: 1912.09335 [hep-ph] (cit. on p. 5).

[73] F. U. Bernlochner, Z. Ligeti, D. J. Robinson, and W. L. Sutcliffe,
*New predictions for $\Lambda_b \to \Lambda_c$ semileptonic decays and tests of heavy quark symmetry*,
Phys. Rev. Lett. **121** (2018) p. 202001, arXiv: `1808.09464 [hep-ph]` (cit. on p. 5).

[74] F. U. Bernlochner, Z. Ligeti, D. J. Robinson, and W. L. Sutcliffe,
*Precise predictions for $\Lambda_b \to \Lambda_c$ semileptonic decays*, Phys. Rev. D **99** (2019) p. 055008,
arXiv: `1812.07593 [hep-ph]` (cit. on p. 5).

[75] J. Harrison, C. T. H. Davies, and A. Lytle, *$R(J/\psi)$ and $B_c^- \to J/\psi \ell^- \bar{\nu}_\ell$ Lepton Flavor
Universality Violating Observables from Lattice QCD*, Phys. Rev. Lett. **125** (2020) p. 222003,
arXiv: `2007.06956 [hep-lat]` (cit. on p. 5).

[76] Belle Collaboration, *Measurement of the branching ratio of $\bar{B} \to D^{(*)} \tau^- \bar{\nu}_\tau$ relative to
$\bar{B} \to D^{(*)} \ell^- \bar{\nu}_\ell$ decays with hadronic tagging at Belle*, Phys. Rev. D **92** (2015) p. 072014,
arXiv: `1507.03233 [hep-ex]` (cit. on pp. 5, 7).

[77] Belle Collaboration,
*Measurement of the $\tau$ lepton polarization and $R(D^*)$ in the decay $\bar{B} \to D^* \tau^- \bar{\nu}_\tau$*,
Phys. Rev. Lett. **118** (2017) p. 211801, arXiv: `1612.00529 [hep-ex]` (cit. on pp. 5, 7).

[78] Belle Collaboration, *Measurement of the $\tau$ lepton polarization and $R(D^*)$ in the decay
$\bar{B} \to D^* \tau^- \bar{\nu}_\tau$ with one-prong hadronic $\tau$ decays at Belle*, Phys. Rev. D **97** (2018) p. 012004,
arXiv: `1709.00129 [hep-ex]` (cit. on pp. 5, 7).

[79] Belle Collaboration, *Measurement of $\mathcal{R}(D)$ and $\mathcal{R}(D^*)$ with a semileptonic tagging method*,
Phys. Rev. Lett. **124** (2020) p. 161803, arXiv: `1910.05864 [hep-ex]` (cit. on pp. 5, 7).

[80] Belle Collaboration, *Measurement of the branching ratio of $\bar{B}^0 \to D^{*+} \tau^- \bar{\nu}_\tau$ relative to
$\bar{B}^0 \to D^{*+} \ell^- \bar{\nu}_\ell$ decays with a semileptonic tagging method*, Phys. Rev. D **94** (2016) p. 072007,
arXiv: `1607.07923 [hep-ex]` (cit. on pp. 5, 7).

[81] LHCb Collaboration,
*Measurement of the ratio of branching fractions $\mathcal{B}(\bar{B}^0 \to D^{*+} \tau^- \bar{\nu}_\tau)/\mathcal{B}(\bar{B}^0 \to D^{*+} \mu^- \bar{\nu}_\mu)$*,
Phys. Rev. Lett. **115** (2015) p. 111803, [Erratum: Phys.Rev.Lett. 115, 159901 (2015)],
arXiv: `1506.08614 [hep-ex]` (cit. on pp. 5, 7).

[82] LHCb Collaboration, *Measurement of the ratio of the $B^0 \to D^{*-} \tau^+ \nu_\tau$ and $B^0 \to D^{*-} \mu^+ \nu_\mu$
branching fractions using three-prong $\tau$-lepton decays*, Phys. Rev. Lett. **120** (2018) p. 171802,
arXiv: `1708.08856 [hep-ex]` (cit. on pp. 5, 7).

[83] LHCb Collaboration, *Test of Lepton Flavor Universality by the measurement of the
$B^0 \to D^{*-} \tau^+ \nu_\tau$ branching fraction using three-prong $\tau$ decays*,
Phys. Rev. D **97** (2018) p. 072013, arXiv: `1711.02505 [hep-ex]` (cit. on pp. 5, 7).

[84] LHCb Collaboration, *LHC Seminar - First joint measurement of $R(D)$ and $R(D^*)$ at LHCb*,
`https://indico.cern.ch/event/1187939/`, 2022-10-18 (cit. on pp. 5, 7).

[85] BaBar Collaboration, *Evidence for an excess of $\bar{B} \to D^{(*)} \tau^- \bar{\nu}_\tau$ decays*,
Phys. Rev. Lett. **109** (2012) p. 101802, arXiv: `1205.5442 [hep-ex]` (cit. on pp. 5, 7).

[86] BaBar Collaboration, *Measurement of an Excess of $\bar{B} \to D^{(*)} \tau^- \bar{\nu}_\tau$ Decays and Implications
for Charged Higgs Bosons*, Phys. Rev. D **88** (2013) p. 072012, arXiv: `1303.0571 [hep-ex]`
(cit. on pp. 5, 7).

[87] A. Bharucha, D. M. Straub, and R. Zwicky,
*$B \to V \ell^+ \ell^-$ in the Standard Model from light-cone sum rules*, JHEP **08** (2016) p. 098,
arXiv: `1503.05534 [hep-ph]` (cit. on pp. 6–8).

[88] R. R. Horgan, Z. Liu, S. Meinel, and M. Wingate, *Lattice QCD calculation of form factors
describing the rare decays $B \to K^* \ell^+ \ell^-$ and $B_s \to \phi \ell^+ \ell^-$*, Phys. Rev. D **89** (2014) p. 094501,
arXiv: `1310.3722 [hep-lat]` (cit. on pp. 6, 8).

[89] D. M. Straub, *flavio: a Python package for flavour and precision phenomenology in the
Standard Model and beyond*, (2018), arXiv: `1810.08132 [hep-ph]` (cit. on pp. 6–8).

[90] R. R. Horgan, Z. Liu, S. Meinel, and M. Wingate,
*Rare B decays using lattice QCD form factors*, PoS **LATTICE2014** (2015) p. 372,
arXiv: `1501.00367 [hep-lat]` (cit. on pp. 6–8).

[91] LHCb Collaboration, *Search for lepton-universality violation in $B^+ \to K^+ \ell^+ \ell^-$ decays*,
Phys. Rev. Lett. **122** (2019) p. 191801, arXiv: `1903.09252 [hep-ex]` (cit. on pp. 6, 8).

[92] LHCb Collaboration, *Test of lepton universality with $B^0 \to K^{*0} \ell^+ \ell^-$ decays*,
JHEP **08** (2017) p. 055, arXiv: `1705.05802 [hep-ex]` (cit. on pp. 6, 8).

[93]  LHCb Collaboration, *Test of lepton universality in $b \to s\ell^+\ell^-$ decays*, (2022),
      arXiv: 2212.09152 [hep-ex] (cit. on pp. 6, 8).

[94]  LHCb Collaboration,
      *Measurement of lepton universality parameters in $B^+ \to K^+\ell^+\ell^-$ and $B^0 \to K^{*0}\ell^+\ell^-$ decays*,
      (2022), arXiv: 2212.09153 [hep-ex] (cit. on pp. 6, 8).

[95]  K. G. Wilson and W. Zimmermann, *Operator product expansions and composite field operators
      in the general framework of quantum field theory*, Commun. Math. Phys. **24** (1972) pp. 87–106
      (cit. on p. 6).

[96]  I. Carli, *Angular analysis of the $B^0 \to K^*\mu^+\mu^-$ decay with the ATLAS detector*,
      PhD. thesis: Faculty of Mathematics and Physics, Charles University in Prague, 2018,
      URL: https://cds.cern.ch/record/2696422/ (cit. on pp. 6, 36).

[97]  J. Aebischer et al., *B-decay discrepancies after Moriond 2019*,
      Eur. Phys. J. C **80** (2020) p. 252, arXiv: 1903.10434 [hep-ph] (cit. on p. 6).

[98]  M. Algueró et al.,
      *Emerging patterns of New Physics with and without Lepton Flavour Universal contributions*,
      Eur. Phys. J. C **79** (2019) p. 714, [Addendum: Eur.Phys.J.C 80, 511 (2020)],
      arXiv: 1903.09578 [hep-ph] (cit. on p. 6).

[99]  M. Ciuchini et al., *New Physics in $b \to s\ell^+\ell^-$ confronts new data on Lepton Universality*,
      Eur. Phys. J. C **79** (2019) p. 719, arXiv: 1903.09632 [hep-ph] (cit. on p. 6).

[100] A. Arbey, T. Hurth, F. Mahmoudi, D. M. Santos, and S. Neshatpour,
      *Update on the $b \to s$ anomalies*, Phys. Rev. D **100** (2019) p. 015045,
      arXiv: 1904.08399 [hep-ph] (cit. on p. 6).

[101] A. D'Alise et al.,
      *Standard model anomalies: lepton flavour non-universality, $g - 2$ and W-mass*,
      JHEP **08** (2022) p. 125, arXiv: 2204.03686 [hep-ph] (cit. on p. 7).

[102] S. Descotes-Genon, L. Hofer, J. Matias, and J. Virto,
      *On the impact of power corrections in the prediction of $B \to K^*\mu^+\mu^-$ observables*,
      JHEP **12** (2014) p. 125, arXiv: 1407.8526 [hep-ph] (cit. on pp. 7, 37, 42).

[103] A. Khodjamirian, T. Mannel, A. A. Pivovarov, and Y. .-. Wang,
      *Charm-loop effect in $B \to K^{(*)}\ell^+\ell^-$ and $B \to K^*\gamma$*, JHEP **09** (2010) p. 089,
      arXiv: 1006.4945 [hep-ph] (cit. on p. 7).

[104] W. Altmannshofer and D. M. Straub, *New physics in $b \to s$ transitions after LHC run 1*,
      Eur. Phys. J. C **75** (2015) p. 382, arXiv: 1411.3161 [hep-ph] (cit. on p. 7).

[105] R. R. Horgan, Z. Liu, S. Meinel, and M. Wingate, *Calculation of $B^0 \to K^{*0}\mu^+\mu^-$ and
      $B_s^0 \to \phi\mu^+\mu^-$ observables using form factors from lattice QCD*,
      Phys. Rev. Lett. **112** (2014) p. 212003, arXiv: 1310.3887 [hep-ph] (cit. on p. 7).

[106] ATLAS, CMS and LHCb Collaborations,
      *Combination of the ATLAS, CMS and LHCb results on the $B_{(s)}^0 \to \mu^+\mu^-$ decays.*,
      CMS-PAS-BPH-20-003, LHCb-CONF-2020-002, ATLAS-CONF-2020-049, 2020,
      URL: https://cds.cern.ch/record/2727216 (cit. on p. 8).

[107] M. Beneke, C. Bobeth, and R. Szafron,
      *Power-enhanced leading-logarithmic QED corrections to $B_q \to \mu^+\mu^-$*, JHEP **10** (2019) p. 232,
      arXiv: 1908.07011 [hep-ph] (cit. on p. 8).

[108] Belle Collaboration,
      *Test of lepton flavor universality and search for lepton flavor violation in $B \to K\ell\ell$ decays*,
      JHEP **03** (2021) p. 105, arXiv: 1908.01848 [hep-ex] (cit. on p. 8).

[109] Belle Collaboration, *Test of Lepton-Flavor Universality in $B \to K^*\ell^+\ell^-$ Decays at Belle*,
      Phys. Rev. Lett. **126** (2021) p. 161801, arXiv: 1904.02440 [hep-ex] (cit. on p. 8).

[110] BaBar Collaboration,
      *Measurement of Branching Fractions and Rate Asymmetries in the Rare Decays $B \to K^{(*)}l^+l^-$*,
      Phys. Rev. D **86** (2012) p. 032012, arXiv: 1204.3933 [hep-ex] (cit. on p. 8).

[111] M. Algueró, B. Capdevila, S. Descotes-Genon, J. Matias, and M. Novoa-Brunet,
      *$b \to s\ell^+\ell^-$ global fits after $R_{K_S}$ and $R_{K^{*+}}$*, Eur. Phys. J. C **82** (2022) p. 326,
      arXiv: 2104.08921 [hep-ph] (cit. on p. 9).

[112] W. Altmannshofer and P. Stangl, *New physics in rare B decays after Moriond 2021*,
      Eur. Phys. J. C **81** (2021) p. 952, arXiv: 2103.13370 [hep-ph] (cit. on p. 9).

[113] M. Ciuchini et al., *Lessons from the $B^{0,+} \to K^{*0,+} \mu^+ \mu^-$ angular analyses*,
Phys. Rev. D **103** (2021) p. 015030, arXiv: 2011.01212 [hep-ph] (cit. on p. 9).

[114] T. Hurth, F. Mahmoudi, D. M. Santos, and S. Neshatpour,
*More Indications for Lepton Nonuniversality in $b \to s\ell^+\ell^-$*,
Phys. Lett. B **824** (2022) p. 136838, arXiv: 2104.10058 [hep-ph] (cit. on p. 9).

[115] *Status of global fits to the data*, talk at conference: Beyond the Flavour Anomalies III, 2022,
URL: https://conference.ippp.dur.ac.uk/event/1064/ (cit. on p. 9).

[116] ATLAS Collaboration, *ATLAS Experiment - Public Luminosity Plots*, https://twiki.cern.
ch/twiki/bin/view/AtlasPublic/WebHome#Detector_Systems_Trigger_Computi,
2022-11-28, further data-summary information available (for ATLAS collaborators only) at
https://atlas.web.cern.ch/Atlas/GROUPS/DATAPREPARATION/DataSummary/ (cit. on p. 10).

[117] HL-LHC Collaboration, *The HL-LHC project*,
https://hilumilhc.web.cern.ch/content/hl-lhc-project, 2022-11-28 (cit. on p. 10).

[118] ATLAS Collaboration, *ATLAS Inner Detector: Technical Design Report, Volume 1*,
ATLAS-TDR-4; CERN-LHCC-97-016, 1997, URL: https://cds.cern.ch/record/331063
(cit. on p. 12).

[119] ATLAS Collaboration, *ATLAS Inner Detector: Technical Design Report, Volume 2*,
ATLAS-TDR-5, CERN-LHCC-97-017, 1997, URL: https://cds.cern.ch/record/331064
(cit. on p. 12).

[120] ATLAS Collaboration, *Study of the rare decays of $B_s^0$ and $B^0$ into muon pairs from data
collected during the LHC Run 1 with the ATLAS detector*, Eur. Phys. J. C **76** (2016) p. 513,
arXiv: 1604.04263 [hep-ex] (cit. on pp. 13, 14, 34).

[121] B. Abbott et al., *Production and integration of the ATLAS Insertable B-Layer*,
JINST **13** (2018) T05008, arXiv: 1803.00844 [physics.ins-det] (cit. on p. 13).

[122] ATLAS Collaboration, *ATLAS Insertable B-Layer: Technical Design Report*,
ATLAS-TDR-19; CERN-LHCC-2010-013, 2010, URL: https://cds.cern.ch/record/1291633
(cit. on p. 13).

[123] ATLAS Collaboration, *Technical Design Report for the ATLAS Inner Tracker Pixel Detector*,
ATLAS-TDR-030, CERN-LHCC-2017-021, 2017, URL: http://cds.cern.ch/record/2285585
(cit. on p. 13).

[124] ATLAS Collaboration, *ATLAS Inner Tracker Strip Detector: Technical Design Report*,
ATLAS-TDR-025; CERN-LHCC-2017-005, 2017, URL: https://cds.cern.ch/record/2257755
(cit. on p. 13).

[125] ATLAS Collaboration, *A High-Granularity Timing Detector for the ATLAS Phase-II Upgrade:
Technical Design Report*, ATLAS-TDR-031; CERN-LHCC-2020-007, 2020,
URL: https://cds.cern.ch/record/2719855 (cit. on p. 13).

[126] ATLAS Collaboration, *ATLAS LAr Calorimeter Phase-II Upgrade: Technical Design Report*,
ATLAS-TDR-027; CERN-LHCC-2017-018, 2017, URL: https://cds.cern.ch/record/2285582
(cit. on p. 14).

[127] ATLAS Collaboration, *ATLAS Tile Calorimeter Phase-II Upgrade: Technical Design Report*,
ATLAS-TDR-028; CERN-LHCC-2017-019, 2017, URL: https://cds.cern.ch/record/2285583
(cit. on p. 14).

[128] ATLAS Collaboration, *Measurement of the muon reconstruction performance of the ATLAS
detector using 2011 and 2012 LHC proton–proton collision data*,
Eur. Phys. J. C **74** (2014) p. 3130, arXiv: 1407.3935 [hep-ex] (cit. on p. 14).

[129] ATLAS Collaboration, *ATLAS New Small Wheel: Technical Design Report*,
ATLAS-TDR-020; CERN-LHCC-2013-006, 2013, URL: https://cds.cern.ch/record/1552862
(cit. on p. 14).

[130] ATLAS Collaboration, *ATLAS Muon Spectrometer Phase-II Upgrade: Technical Design Report*,
ATLAS-TDR-026; CERN-LHCC-2017-017, 2017, URL: https://cds.cern.ch/record/2285580
(cit. on p. 14).

[131] ATLAS Collaboration, *Readiness of the ATLAS Tile Calorimeter for LHC collisions*,
Eur. Phys. J. C **70** (2010) p. 1193, arXiv: 1007.5423 [hep-ex] (cit. on p. 15).

[132] ATLAS Collaboration,
*$dE/dx$ measurement in the ATLAS Pixel Detector and its use for particle identification*,
ATLAS-CONF-2011-016, 2011, URL: https://cds.cern.ch/record/1336519 (cit. on p. 15).

[133] ATLAS Collaboration, *Performance of the ATLAS Trigger System in 2010*, Eur. Phys. J. C **72** (2012) p. 1849, arXiv: 1110.1530 [hep-ex] (cit. on p. 15).

[134] ATLAS Collaboration, *Performance of the ATLAS trigger system in 2015*, Eur. Phys. J. C **77** (2017) p. 317, arXiv: 1611.09661 [hep-ex] (cit. on p. 15).

[135] ATLAS Collaboration, *Performance of the ATLAS Level-1 topological trigger in Run 2*, Eur. Phys. J. C **82** (2021) p. 7, arXiv: 2105.01416 [hep-ex] (cit. on p. 15).

[136] ATLAS Collaboration, *Trigger-object Level Analysis with the ATLAS detector at the Large Hadron Collider: summary and perspectives*, ATL-DAQ-PUB-2017-003, 2017, URL: https://cds.cern.ch/record/2295739 (cit. on p. 16).

[137] ATLAS Collaboration, *ATLAS data quality operations and performance for 2015–2018 data-taking*, JINST **15** (2020) P04003, arXiv: 1911.04632 [physics.ins-det] (cit. on p. 16).

[138] ATLAS Collaboration, *Operation of the ATLAS trigger system in Run 2*, JINST **15** (2020) P10004, arXiv: 2007.12539 [hep-ex] (cit. on pp. 16, 23).

[139] *The Worldwide LHC Computing Grid*, https://wlcg-public.web.cern.ch/, 2022-10-15 (cit. on p. 16).

[140] ATLAS Collaboration, *The ATLAS Collaboration Software and Firmware*, ATL-SOFT-PUB-2021-001, 2021, URL: https://cds.cern.ch/record/2767187 (cit. on p. 16).

[141] ATLAS Collaboration, *The ATLAS Experiment's main offline software repository*, https://gitlab.cern.ch/atlas/athena/, 2022-12-01 (cit. on p. 16).

[142] R. Brun and F. Rademakers, *ROOT – An object oriented data analysis framework*, Nucl. Instrum. Meth. A **389** (1997) pp. 81–86, ISSN: 0168-9002 (cit. on p. 16).

[143] ATLAS Collaboration, *The ATLAS Simulation Infrastructure*, Eur. Phys. J. C **70** (2010) p. 823, arXiv: 1005.4568 [physics.ins-det] (cit. on p. 16).

[144] T. Sjöstrand et al., *An introduction to PYTHIA 8.2*, Comput. Phys. Commun. **191** (2015) p. 159, arXiv: 1410.3012 [hep-ph] (cit. on p. 16).

[145] M. Bähr et al., *Herwig++ physics and manual*, Eur. Phys. J. C **58** (2008) p. 639, arXiv: 0803.0883 [hep-ph] (cit. on p. 16).

[146] T. Gleisberg et al., *Event generation with SHERPA 1.1*, JHEP **02** (2009) p. 007, arXiv: 0811.4622 [hep-ph] (cit. on p. 16).

[147] J. Alwall et al., *The automated computation of tree-level and next-to-leading order differential cross sections, and their matching to parton shower simulations*, JHEP **07** (2014) p. 079, arXiv: 1405.0301 [hep-ph] (cit. on p. 17).

[148] D. J. Lange, *The EvtGen particle decay simulation package*, Nucl. Instrum. Meth. A **462** (2001) p. 152, Proceedings, 7th International Conference on B physics at hadron machines (BEAUTY 2000) (cit. on p. 17).

[149] GEANT4 Collaboration, S. Agostinelli, et al., *GEANT4 – a simulation toolkit*, Nucl. Instrum. Meth. A **506** (2003) p. 250 (cit. on p. 17).

[150] ATLAS Collaboration, *AtlFast3: The Next Generation Of Fast Simulation in ATLAS*, Comput. Softw. Big Sci. **6** (2021) p. 7, arXiv: 2109.02551 [hep-ex] (cit. on p. 17).

[151] J. de Favereau et al., *DELPHES 3, A modular framework for fast simulation of a generic collider experiment*, JHEP **02** (2014) p. 057, arXiv: 1307.6346 [hep-ex] (cit. on p. 17).

[152] ATLAS Collaboration, *ATLAS Experiment - Public B-physics and Light States Results*, https://twiki.cern.ch/twiki/bin/view/AtlasPublic/BPhysPublicResults, 2022-12-11 (cit. on p. 19).

[153] ATLAS Collaboration, *Measurement of the total cross section from elastic scattering in pp collisions at $\sqrt{s} = 7$ TeV with the ATLAS detector*, Nucl. Phys. B **889** (2014) p. 486, arXiv: 1408.5778 [hep-ex] (cit. on p. 19).

[154] ATLAS Collaboration, *Measurement of the total cross section from elastic scattering in pp collisions at $\sqrt{s} = 8$ TeV with the ATLAS detector*, Phys. Lett. B **761** (2016) p. 158, arXiv: 1607.06605 [hep-ex] (cit. on p. 19).

[155] ATLAS Collaboration, *Measurement of the total cross section and ρ-parameter from elastic scattering in pp collisions at $\sqrt{s} = 13$ TeV with the ATLAS detector*, (2022), arXiv: 2207.12246 [hep-ex] (cit. on p. 19).

[156] J. Stirling, *Parton Luminosity and Cross Section Plots*,
https://twiki.cern.ch/twiki/bin/view/AtlasPublic, 2022-12-12 (cit. on p. 19).

[157] ATLAS Collaboration, *Measurement of the b-hadron production cross section using decays to $D^{*+}\mu^- X$ final states in pp collisions at $\sqrt{s} = 7$ TeV with the ATLAS detector*,
Nucl. Phys. B **864** (2012) p. 341, arXiv: 1206.3122 [hep-ex] (cit. on pp. 19, 26).

[158] ATLAS Collaboration, *Measurement of the differential cross-section of $B^+$ meson production in pp collisions at $\sqrt{s} = 7$ TeV at ATLAS*, JHEP **10** (2013) p. 042,
arXiv: 1307.0126 [hep-ex] (cit. on p. 19).

[159] M. Marčišovský, *A study of the $b\bar{b}$ production mechanisms with the ATLAS experiment*,
Ph.D. thesis: Czech Technical University in Prague, Faculty of Nuclear Sciences and Physical Engineering, 2016,
URL: https://physics.fjfi.cvut.cz/publications/ejcf/DIS_Marcisovsky_Michal.pdf
(cit. on pp. 19, 20).

[160] Particle Data Group, *Review of Particle Physics*, PTEP **2022** (2022) p. 083C01
(cit. on pp. 19, 22, 30, 34, 38).

[161] ATLAS Collaboration, *ATLAS Experiment - B-physics Trigger Public Results*,
https://twiki.cern.ch/twiki/bin/view/AtlasPublic/BPhysicsTriggerPublicResults,
2022-12-11 (cit. on pp. 20, 22).

[162] ATLAS Collaboration, *Measurement of the average B lifetime in inclusive $B \to J/\psi X \to \mu^+\mu^- X$ decays with the ATLAS detector*, ATLAS-CONF-2011-145, 2011,
URL: https://cds.cern.ch/record/1389455 (cit. on p. 21).

[163] V. Kostyukhin, *VKalVrt - package for vertex reconstruction in ATLAS*, ATL-PHYS-2003-031,
2003, URL: https://cds.cern.ch/record/685551 (cit. on p. 21).

[164] ATLAS Collaboration, *Reconstruction of primary vertices at the ATLAS experiment in Run 1 proton–proton collisions at the LHC*, Eur. Phys. J. C **77** (2017) p. 332,
arXiv: 1611.10235 [hep-ex] (cit. on p. 22).

[165] ATLAS Collaboration, $K_S^0$ *and $\Lambda$ production in pp interactions at $\sqrt{s} = 0.9$ and 7 TeV measured with the ATLAS detector at the LHC*, Phys. Rev. D **85** (2012) p. 012001,
arXiv: 1111.1297 [hep-ex] (cit. on p. 23).

[166] ATLAS Collaboration, *ATLAS Experiment - Tracking Performance Results*, https://twiki.cern.ch/twiki/bin/view/AtlasPublic/InDetTrackingPerformanceApprovedPlots,
2022-12-11 (cit. on p. 24).

[167] W. Verkerke and D. P. Kirkby, *The RooFit toolkit for data modeling*,
eConf **C0303241** (2003) MOLT007, ed. by L. Lyons and M. Karagoz,
arXiv: physics/0306116 (cit. on p. 25).

[168] ATLAS Collaboration,
*Measurement of the differential cross-sections of prompt and non-prompt production of $J/\psi$ and $\psi(2S)$ in pp collisions at $\sqrt{s} = 7$ and 8 TeV with the ATLAS detector*,
Eur. Phys. J. C **76** (2016) p. 283, arXiv: 1512.03657 [hep-ex] (cit. on p. 26).

[169] S. S. Wilks,
*The Large-Sample Distribution of the Likelihood Ratio for Testing Composite Hypotheses*,
Annals Math. Statist. **9** (1938) pp. 60–62 (cit. on p. 25).

[170] G. Cowan, K. Cranmer, E. Gross, and O. Vitells,
*Asymptotic formulae for likelihood-based tests of new physics*,
Eur. Phys. J. C **71** (2011) p. 1554, [Erratum: Eur.Phys.J.C 73, 2501 (2013)],
arXiv: 1007.1727 [physics.data-an] (cit. on p. 25).

[171] A. L. Read, *Presentation of search results: The CL(s) technique*,
J. Phys. G **28** (2002) pp. 2693–2704, ed. by M. R. Whalley and L. Lyons (cit. on p. 25).

[172] ZEUS Collaboration,
*Measurement of inelastic $J/\psi$ production in deep inelastic scattering at HERA*,
Eur. Phys. J. C **44** (2005) pp. 13–25, arXiv: hep-ex/0505008 (cit. on p. 26).

[173] N. L. Johnson, *Bivariate Distributions Based On Simple Translation Systems*,
Biometrika **36** (1949) pp. 297–304, ISSN: 0006-3444, eprint:
https://academic.oup.com/biomet/article-pdf/36/3-4/297/530659/36-3-4-297.pdf
(cit. on p. 26).

[174] N. L. Johnson, *Systems of Frequency Curves Generated by Methods of Translation*,
Biometrika **36** (1949) pp. 149–176, ISSN: 00063444,
URL: http://www.jstor.org/stable/2332539 (visited on 12/15/2022) (cit. on p. 26).

[175] M. Pivk and F. R. Le Diberder, *SPlot: A Statistical tool to unfold data distributions*,
Nucl. Instrum. Meth. A **555** (2005) pp. 356–369, arXiv: physics/0402083 (cit. on p. 26).

[176] G. Punzi, *Comments on likelihood fits with variable resolution*,
eConf **C030908** (2003) WELT002, ed. by L. Lyons, R. P. Mount, and R. Reitmeyer,
arXiv: physics/0401045 (cit. on p. 26).

[177] M. Smižanská, *PythiaB an interface to Pythia6 dedicated to simulation of beauty events*,
ATL-COM-PHYS-2003-038, 2003, URL: https://cds.cern.ch/record/681440,
Document available for ATLAS members only, code public at
https://gitlab.cern.ch/atlas/athena/-/tree/master/Generators/Pythia8B_i
(cit. on p. 27).

[178] J. Pumplin et al.,
*New generation of parton distributions with uncertainties from global QCD analysis*,
JHEP **07** (2002) p. 012, arXiv: hep-ph/0201195 (cit. on p. 27).

[179] ATLAS Collaboration, *ATLAS Pythia 8 tunes to 7 TeV data*, ATL-PHYS-PUB-2014-021, 2014,
URL: https://cds.cern.ch/record/1966419 (cit. on p. 27).

[180] ATLAS Collaboration,
*Luminosity determination in pp collisions at $\sqrt{s} = 7$ TeV using the ATLAS detector at the LHC*,
Eur. Phys. J. C **71** (2011) p. 1630, arXiv: 1101.2185 [hep-ex] (cit. on p. 27).

[181] ATLAS Collaboration, *Improved luminosity determination in pp collisions at $\sqrt{s} = 7$ TeV using
the ATLAS detector at the LHC*, Eur. Phys. J. C **73** (2013) p. 2518,
arXiv: 1302.4393 [hep-ex] (cit. on p. 27).

[182] ATLAS Collaboration,
*Luminosity determination in pp collisions at $\sqrt{s} = 8$ TeV using the ATLAS detector at the LHC*,
Eur. Phys. J. C **76** (2016) p. 653, arXiv: 1608.03953 [hep-ex] (cit. on p. 27).

[183] ATLAS Collaboration, *Luminosity determination in pp collisions at $\sqrt{s} = 13$ TeV using the
ATLAS detector at the LHC*, ATLAS-CONF-2019-021, 2019,
URL: https://cds.cern.ch/record/2677054 (cit. on p. 27).

[184] ATLAS Collaboration, *Alignment of the ATLAS Inner Detector and its Performance in 2012*,
ATLAS-CONF-2014-047, 2014, URL: https://cds.cern.ch/record/1741021 (cit. on p. 29).

[185] A. D. Sakharov,
*Violation of CP Invariance, C asymmetry, and baryon asymmetry of the universe*,
Pisma Zh. Eksp. Teor. Fiz. **5** (1967) pp. 32–35 (cit. on p. 30).

[186] N. Cabibbo, *Unitary Symmetry and Leptonic Decays*, Phys. Rev. Lett. **10** (1963) pp. 531–533
(cit. on p. 30).

[187] M. Kobayashi and T. Maskawa,
*CP Violation in the Renormalizable Theory of Weak Interaction*,
Prog. Theor. Phys. **49** (1973) pp. 652–657 (cit. on p. 30).

[188] A. Riotto, *Theories of baryogenesis*,
ICTP Summer School in High-Energy Physics and Cosmology, 1998 pp. 326–436,
arXiv: hep-ph/9807454 (cit. on p. 30).

[189] J. Charles et al., *Predictions of selected flavour observables within the Standard Model*,
Phys. Rev. D **84** (2011) p. 033005, arXiv: 1106.4041 [hep-ph],
CKMFitter, updated with spring 2011 results (cit. on pp. 30, 33).

[190] ATLAS Collaboration,
*Measurement of the CP-violating phase $\phi_s$ in $B_s^0 \to J/\psi\phi$ decays in ATLAS at 13 TeV*,
Eur. Phys. J. C **81** (2021) p. 342, arXiv: 2001.07115 [hep-ex] (cit. on p. 33).

[191] D0 Collaboration, *Measurement of the CP-violating phase $\phi_s^{J/\psi\phi}$ using the flavor-tagged decay
$B_s^0 \to J/\psi\phi$ in 8 fb$^{-1}$ of $p\bar{p}$ collisions*, Phys. Rev. D **85** (2012) p. 032006,
arXiv: 1109.3166 [hep-ex] (cit. on p. 33).

[192] CDF Collaboration,
*Measurement of the Bottom-Strange Meson Mixing Phase in the Full CDF Data Set*,
Phys. Rev. Lett. **109** (2012) p. 171802, arXiv: 1208.2967 [hep-ex] (cit. on p. 33).

[193]  CMS Collaboration, *Measurement of the CP-violating weak phase $\phi_s$ and the decay width difference $\Delta\Gamma_s$ using the $B_s^0 \to J/\psi\phi(1020)$ decay channel in pp collisions at $\sqrt{s} = 8$ TeV,*
Phys. Lett. B **757** (2016) pp. 97–120, arXiv: 1507.07527 [hep-ex] (cit. on p. 33).

[194]  CMS Collaboration, *Measurement of the CP-violating phase $\phi_s$ in the $B_s^0 \to J/\psi\,\phi(1020) \to \mu^+\mu^- K^+K^-$ channel in proton-proton collisions at $\sqrt{s} = 13$ TeV,*
Phys. Lett. B **816** (2021) p. 136188, arXiv: 2007.02434 [hep-ex] (cit. on p. 33).

[195]  LHCb Collaboration, *Precision measurement of CP violation in $B_s^0 \to J/\psi K^+K^-$ decays,*
Phys. Rev. Lett. **114** (2015) p. 041801, arXiv: 1411.3104 [hep-ex] (cit. on p. 33).

[196]  LHCb Collaboration,
*Updated measurement of time-dependent CP-violating observables in $B_s^0 \to J/\psi K^+K^-$ decays,*
Eur. Phys. J. C **79** (2019) p. 706, [Erratum: Eur.Phys.J.C 80, 601 (2020)],
arXiv: 1906.08356 [hep-ex] (cit. on p. 33).

[197]  A. Lenz and G. Tetlalmatzi-Xolocotzi,
*Model-independent bounds on new physics effects in non-leptonic tree-level decays of B-mesons,*
JHEP **07** (2020) p. 177, arXiv: 1912.07621 [hep-ph] (cit. on p. 33).

[198]  S. L. Glashow, J. Iliopoulos, and L. Maiani, *Weak Interactions with Lepton-Hadron Symmetry,*
Phys. Rev. D **2** (1970) pp. 1285–1292 (cit. on p. 34).

[199]  I. Dunietz, H. R. Quinn, A. Snyder, W. Toki, and H. J. Lipkin,
*How to extract CP violating asymmetries from angular correlations,*
Phys. Rev. D **43** (1991) pp. 2193–2208 (cit. on p. 35).

[200]  S. Descotes-Genon, T. Hurth, J. Matias, and J. Virto,
*Optimizing the basis of $B \to K^* ll$ observables in the full kinematic range,*
JHEP **05** (2013) p. 137, arXiv: 1303.5794 [hep-ph] (cit. on p. 35).

[201]  S. Descotes-Genon, J. Matias, M. Ramon, and J. Virto,
*Implications from clean observables for the binned analysis of $B \to K^*\mu^+\mu^-$ at large recoil,*
JHEP **01** (2013) p. 048, arXiv: 1207.2753 [hep-ph] (cit. on p. 35).

[202]  M. Ciuchini et al.,
*$B \to K^*\ell^+\ell^-$ decays at large recoil in the Standard Model: a theoretical reappraisal,*
JHEP **06** (2016) p. 116, arXiv: 1512.07157 [hep-ph] (cit. on pp. 37, 42).

[203]  S. Jäger and J. Martin Camalich,
*On $B \to V\ell\ell$ at small dilepton invariant mass, power corrections, and new physics,*
JHEP **05** (2013) p. 043, arXiv: 1212.2263 [hep-ph] (cit. on pp. 37, 42).

[204]  S. Jäger and J. Martin Camalich, *Reassessing the discovery potential of the $B \to K^*\ell^+\ell^-$ decays in the large-recoil region: SM challenges and BSM opportunities,*
Phys. Rev. D **93** (2016) p. 014028, arXiv: 1412.3183 [hep-ph] (cit. on p. 37).

[205]  LHCb Collaboration,
*Angular analysis of the $B^0 \to K^{*0}\mu^+\mu^-$ decay using 3 fb$^{-1}$ of integrated luminosity,*
JHEP **02** (2016) p. 104, arXiv: 1512.04442 [hep-ex] (cit. on p. 37).

[206]  CMS Collaboration,
*Angular analysis of the decay $B^0 \to K^{*0}\mu^+\mu^-$ from pp collisions at $\sqrt{s} = 8$ TeV,*
Phys. Lett. B **753** (2016) pp. 424–448, arXiv: 1507.08126 [hep-ex] (cit. on p. 37).

[207]  CMS Collaboration, *Measurement of angular parameters from the decay $B^0 \to K^{*0}\mu^+\mu^-$ in proton-proton collisions at $\sqrt{s} = 8$ TeV,* Phys. Lett. B **781** (2018) pp. 517–541,
arXiv: 1710.02846 [hep-ex] (cit. on p. 37).

[208]  Belle Collaboration, *Measurement of the Differential Branching Fraction and Forward-Backward Asymmetry for $B \to K^{(*)}\ell^+\ell^-$,* Phys. Rev. Lett. **103** (2009) p. 171801,
arXiv: 0904.0770 [hep-ex] (cit. on p. 37).

[209]  Belle Collaboration, *Angular analysis of $B^0 \to K^*(892)^0\ell^+\ell^-$,*
LHC Ski 2016: A First Discussion of 13 TeV Results, 2016, arXiv: 1604.04042 [hep-ex]
(cit. on p. 37).

[210]  BaBar Collaboration, *Measurement of angular asymmetries in the decays $B \to K^*\ell^+\ell^-$,*
Phys. Rev. D **93** (2016) p. 052015, arXiv: 1508.07960 [hep-ex] (cit. on p. 37).

[211]  Belle Collaboration,
*Observation of a narrow charmonium-like state in exclusive $B^\pm \to K^\pm\pi^+\pi^- J/\psi$ decays,*
Phys. Rev. Lett. **91** (2003) p. 262001, arXiv: hep-ex/0309032 (cit. on p. 38).

54

[212] K. H. Hicks, *On the conundrum of the pentaquark*, Eur. Phys. J. H **37** (2012) pp. 1–31 (cit. on p. 38).

[213] LHCb Collaboration,
*Observation of $J/\psi p$ Resonances Consistent with Pentaquark States in $\Lambda_b^0 \to J/\psi K^- p$ Decays*,
Phys. Rev. Lett. **115** (2015) p. 072001, arXiv: 1507.03414 [hep-ex] (cit. on p. 38).

[214] ATLAS Collaboration, *Measurements of $\psi(2S)$ and $X(3872) \to J/\psi\pi^+\pi^-$ production in pp collisions at $\sqrt{s} = 8$ TeV with the ATLAS detector*, JHEP **01** (2017) p. 117,
arXiv: 1610.09303 [hep-ex] (cit. on p. 38).

[215] ATLAS Collaboration, *Study of $J/\psi p$ resonances in the $\Lambda_b^0 \to J/\psi p K^-$ decays in pp collisions at $\sqrt{s} = 7$ and 8 TeV with the ATLAS detector*, ATLAS-CONF-2019-048, 2019,
URL: https://cds.cern.ch/record/2693957 (cit. on p. 38).

[216] D0 Collaboration, *The Upgraded D0 detector*, Nucl. Instrum. Meth. A **565** (2006) pp. 463–537,
arXiv: physics/0507191 (cit. on p. 38).

[217] D0 Collaboration, *Evidence for a $B_s^0\pi^\pm$ state*, Phys. Rev. Lett. **117** (2016) p. 022003,
arXiv: 1602.07588 [hep-ex] (cit. on p. 38).

[218] LHCb Collaboration, *Search for Structure in the $B_s^0\pi^\pm$ Invariant Mass Spectrum*,
Phys. Rev. Lett. **117** (2016) p. 152003, [Addendum: Phys.Rev.Lett. 118, 109904 (2017)],
arXiv: 1608.00435 [hep-ex] (cit. on p. 38).

[219] CMS Collaboration,
*Search for the X(5568) state decaying into $B_s^0\pi^\pm$ in proton-proton collisions at $\sqrt{s} = 8$ TeV*,
Phys. Rev. Lett. **120** (2018) p. 202005, arXiv: 1712.06144 [hep-ex] (cit. on p. 38).

[220] CDF Collaboration,
*A search for the exotic meson $X(5568)$ with the Collider Detector at Fermilab*,
Phys. Rev. Lett. **120** (2018) p. 202006, arXiv: 1712.09620 [hep-ex] (cit. on p. 38).

[221] Belle-II Collaboration, *The Belle II Physics Book*, PTEP **2019** (2019) p. 123C01, ed. by
E. Kou and P. Urquijo, [Erratum: PTEP 2020, 029201 (2020)], arXiv: 1808.10567 [hep-ex]
(cit. on p. 40).

[222] Belle-II Collaboration, *Belle II Technical Design Report*, (2010),
arXiv: 1011.0352 [physics.ins-det] (cit. on p. 40).

[223] Belle Collaboration, *Physics Achievements from the Belle Experiment*,
PTEP **2012** (2012) p. 04D001, arXiv: 1212.5342 [hep-ex] (cit. on p. 40).

[224] FCC Collaboration,
*FCC Physics Opportunities: Future Circular Collider Conceptual Design Report Volume 1*,
Eur. Phys. J. C **79** (2019) p. 474 (cit. on p. 40).

[225] ATLAS Collaboration, *Prospects for lepton flavour violation measurements in $\tau \to 3\mu$ decays with the ATLAS detector at the HL-LHC*, ATL-PHYS-PUB-2018-032, 2018,
URL: https://cds.cern.ch/record/2647956 (cit. on p. 40).

[226] ATLAS Collaboration, *Prospects for the $\mathcal{B}(B_{(s)}^0 \to \mu^+\mu^-)$ measurements with the ATLAS detector in the Run 2 and HL-LHC data campaigns*, ATL-PHYS-PUB-2018-005, 2018,
URL: https://cds.cern.ch/record/2317211 (cit. on p. 40).

[227] Particle Data Group, *Review of Particle Physics*, Phys. Rev. D **98** (2018) p. 030001
(cit. on p. 42).

[228] Heavy Flavor Averaging Group,
*Averages of b-hadron, c-hadron, and $\tau$-lepton properties as of summer 2016*, Eur. Phys. J. **C77**
(2017) p. 895, updated results and plots available at https://hflav.web.cern.ch,
arXiv: 1612.07233 [hep-ex] (cit. on p. 42).

# A Publications Forming the Habilitation Thesis

## A.1 Search for New Physics Effects in Rare and *CP*-Violating *B*-Meson Decays, Search for New States

The list below contains papers in reviewed journals where I am one of the main authors within the ATLAS Collaboration:

- G. Aad, ..., P. Řezníček, ... et al. (ATLAS Collaboration), *Measurement of the CP-violating phase $\phi_s$ in $B_s^0 \to J/\psi\phi$ decays in ATLAS at 13 TeV*, Eur. Phys. J. C **81**.4 (2021) p. 342, arXiv: 2001.07115 [hep-ex]

- G. Aad, ..., P. Řezníček, ... et al. (ATLAS Collaboration), *Measurement of the CP-violating phase $\phi_s$ and the $B_s^0$ meson decay width difference with $B_s^0 \to J/\psi\phi$ decays in ATLAS*, JHEP **08** (2016) p. 147, arXiv: 1601.03297 [hep-ex]

- G. Aad, ..., P. Řezníček, ... et al. (ATLAS Collaboration), *Flavor tagged time-dependent angular analysis of the $B_s^0 \to J/\psi\phi$ decay and extraction of $\Delta\Gamma_s$ and the weak phase $\phi_s$ in ATLAS*, Phys. Rev. D **90**.5 (2014) p. 052007, arXiv: 1407.1796 [hep-ex]

- G. Aad, ..., P. Řezníček, ... et al. (ATLAS Collaboration), *Time-dependent angular analysis of the decay $B_s^0 \to J/\psi\phi$ and extraction of $\Delta\Gamma_s$ and the CP-violating weak phase $\phi_s$ by ATLAS*, JHEP **12** (2012) p. 072, arXiv: 1208.0572 [hep-ex]

- M. Aaboud, ..., P. Řezníček, ... et al. (ATLAS Collaboration), *Angular analysis of $B_d^0 \to K^*\mu^+\mu^-$ decays in pp collisions at $\sqrt{s} = 8$ TeV with the ATLAS detector*, JHEP **10** (2018) p. 047, arXiv: 1805.04000 [hep-ex]

- M. Aaboud, ..., P. Řezníček, ... et al. (ATLAS Collaboration), *Search for a Structure in the $B_s^0\pi^\pm$ Invariant Mass Spectrum with the ATLAS Experiment*, Phys. Rev. Lett. **120**.20 (2018) p. 202007, arXiv: 1802.01840 [hep-ex]

## A.2 Projections of the B-Physics Analyses for the Future Stages of the LHC and the ATLAS Experiment

An important part of the B-physics analyses were also studies of the expected performance and projected results for the future stages of the LHC: the Upgraded ATLAS experiment at the High-Luminosity LHC. I am one of the main authors of these analyses within the ATLAS Collaboration. The latest ones

- G. Aad, ..., P. Řezníček, ... et al. (ATLAS Collaboration), $B_d^0 \to K^{*0}\mu\mu$ *angular analysis prospects with the upgraded ATLAS detector at the HL-LHC*, ATL-PHYS-PUB-2019-003, 2019, URL: https://cds.cern.ch/record/2654519

- G. Aad, ..., P. Řezníček, ... et al. (ATLAS Collaboration), *CP-violation measurement prospects in the $B_s^0 \to J/\psi\phi$ channel with the upgraded ATLAS detector at the HL-LHC*, ATL-PHYS-PUB-2018-041, 2018, URL: https://cds.cern.ch/record/2649881

became part of the collection of all such studies from LHC experiments published as the CERN Yellow Report Monograph CERN-2019-007 [21]. Results of the preceding studies of mine, including in addition expected trigger efficiencies, can be found in the Technical Design Reports for the Phase II Upgrade of the ATLAS TDAQ system (ATLAS-TDR-029 [23]) and for the ATLAS Inner Tracker Pixel Detector (ATLAS-TDR-030 [24]). All the papers are thoroughly reviewed within the ATLAS collaboration.

### A.3  Performance of the *B*-Meson Decays Reconstruction

Studying the performance and features of reconstruction of *b*-hadron decays is the usual first step of all the B-physics analyses. Results of such analyses, in which I am one of the main authors, can be found in the following public materials reviewed within the ATLAS collaboration.

- G. Aad, ..., P. Řezníček, ... et al. (ATLAS Collaboration), $B^\pm$ *mass reconstruction in* $B^\pm \to J/\psi K^\pm$ *decay at ATLAS at 13 TeV pp collisions at the LHC*, ATLAS-CONF-2015-064, 2015, URL: http://cds.cern.ch/record/2114830

- G. Aad, ..., P. Řezníček, ... et al. (ATLAS Collaboration), *Study of alignment-related systematic effects on the ATLAS Inner Detector tracking*, ATLAS-CONF-2012-141, 2012, URL: http://cds.cern.ch/record/1483518

- G. Aad, ..., P. Řezníček, ... et al. (ATLAS Collaboration), *Measurement of the* $B_d^0$ *and* $B_s^0$ *lifetimes in the decay modes* $B_d^0 \to J/\psi K^{0*}$ *and* $B_s^0 \to J/\psi \phi$ *in ATLAS*, ATLAS-CONF-2011-092, 2011, URL: http://cds.cern.ch/record/1363779

- G. Aad, ..., P. Řezníček, ... et al. (ATLAS Collaboration), *Observation of the* $B_d^0$ *and* $B_s^0$ *mesons in the decays* $B_d^0 \to J/\psi K^{0*}$ *and* $B_s^0 \to J/\psi \phi$ *in ATLAS*, ATLAS-CONF-2011-050, 2011, URL: http://cds.cern.ch/record/1341815

- N. Kanaya, A. Krasznahorkay, H. Kurashige, C. Omachi, P. Řezníček, *Performance study of the level-1 di-muon trigger*, ATL-PHYS-PUB-2009-045, 2009, URL: http://cds.cern.ch/record/1167941

### A.4  Analysis Tools for ATLAS B-physics Group

The reconstruction software of the ATLAS experiment provides data which encapsulates basic physics-like objects. In order to perform the analysis of the data, complex analysis software is needed. I was one of the developers of these analysis tools for the whole ATLAS B-physics group. Their description can be found in the following conference proceedings:

- P. Řezníček, C. Anastopoulos, E. B-Thacker, J. Catmore, S. Dallison, F. Derue, B. Epp, P. Jussel, A. Kaczmarska, L. d. Mora, H. v. Radzievwski, T. Stahl for the ATLAS Collaboration, *Physics analysis tools for beauty physics in ATLAS*, J. Phys. Conf. Ser. **119** (2008) p. 032003, Proceedings, 16th International Conference on Computing in High Energy and Nuclear Physics (CHEP 2007): Victoria, Canada, September 2-7, 2007